ULTRASOUND - AIDED LASER JOINING OF METALS TO PLASTICS

CHEN YUJIAO

Ph.D

The Hong Kong Polytechnic University

2018

THE HONG KONG POLYTECHNIC UNIVERSITY

DEPARTMENT OF INDUSTRIAL AND SYSTEMS ENGINEERING

ULTRASOUND - AIDED LASER JOINING OF METALS TO PLASTICS

CHEN YUJIAO

A thesis submitted in partial fulfilment of the requirements

for the degree of Doctor of Philosophy

June 2017

CERTIFICATE OF ORIGINALITY

I hereby declare that this thesis is my own work and that, to the best of my knowledge and belief, it reproduces no material previously published or written, nor material that has been accepted for the award of any other degree or diploma, except where due acknowledgement has been made in the text.

_____ (Signed)

CHEN Yujiao (Name of student)

Abstract

In recent years, much interest has been shown in joining dissimilar materials such as light metals and plastics using laser technology, especially in the automobile and biomedical industries. To this end, a direct laser bonding technique for joining metals to plastics, namely laser-assisted metal and plastic (LAMP) joining, has been developed over the last ten years. It uses laser light to heat up the metal-plastic interface, and the plastic at the interface is melted and partly decomposed. This results in the formation of gas bubbles in the molten plastic. It is generally accepted that the high pressure developed inside the laser-induced bubbles causes the molten plastic to have intimate contact with the metal surface, and as a result, a strong bonding between the metal and plastic parts is attained. Despite a number of successes that have been obtained in the LAMP process, the inherent features of laser-induced bubbles in the joint are still a main concern because the bubbles themselves are defects by nature, and therefore have a counter effect on the joint strength.

In this research, a new ultrasound-aided laser joining process – using the conjoint action of a laser and ultrasonics – for joining metals to plastics (U-LAMP) has been successfully developed, and has been shown to be able to eliminate the laser-induced bubbles with increased joint strength. For the first phase of the research, an ultrasonic generation system with an appropriate specimen clamping tool was designed and fabricated for studying the U-LAMP process. The system allows the specimens to be joined to be ultrasonically vibrated while under laser irradiation. For the second phase of the research, the

new U-LAMP process was employed to join polyethylene terephthalate (PET) to pure titanium (Ti) to show the superiority of U-LAMP over the conventional LAMP. The effects of ultrasonic vibration on the chemical bond formation at the joint interface, removal of bubbles in the joint, and the shear and fatigue properties of the joints were studied.

Under a low laser power condition, where decomposition of the plastic was avoided and therefore the laser-induced bubble problem was not encountered, the benefit of ultrasonic action was found to be in the promotion of the formation of chemical bonds (TiO_2, Ti_2O_3, Ti-O, and Ti-C) at the joint interface. This was supported by the results of XPS analyses conducted across the joint interface. As a result, the joint strength can be increased by as much as seven times that produced by the conventional LAMP process. While joining at high laser power, where laser-induced bubbles are present, the primary function of ultrasonic vibration is to eliminate bubbles in the joint. With a proper ultrasonic tool design to create a differential pressure field in the joint specimen, bubbles in the molten plastic pool can be made to escape from the joint zone. The effects of ultrasonic vibration on the bubble dynamics, bubble translation path and bubble removal mechanism were analysed based on the ultrasonic vibration induced pressure field. The bubble translation path in the molten pool was also studied using a high speed camera, and the captured bubble movement path agrees well with the predicted path of the pressure field analysis. In regard to the mechanical properties, the joint strength of the U-LAMP specimens, measured in terms of the fracture load, was significantly higher than that of the LAMP specimens. Moreover, for the former, fracture occurred in the parent plastic material, whereas for the latter, almost all fractures occurred at the

metal-plastic interface. This shows that the metal-plastic interfacial bond strength of U-LAMP specimens is higher than that of LAMP specimens. The superiority of U-LAMP over the conventional LAMP is also evident by the extended fatigue life of the U-LAMP specimens over that of the LAMP specimens, at least one order of magnitude higher. The improvement in fatigue life is due to the absence of porosity in the U-LAMP specimens which also exhibit strong interfacial bonding. The different fatigue crack propagation paths in both LAMP and U-LAMP joints were established.

ACKNOWLEDGEMENTS

I would like to take this opportunity to express my deep and sincere appreciation towards my Chief Supervisor, Professor T.M. Yue whose tireless inspiration and help guided me to overcome the difficulties in my Ph.D study and in my life. I also express my sincere gratitude to Professor Z.N. Guo, my Co-supervisor, for his encouragement and the valuable suggestions he gave to me throughout my research study.

My sincere thanks also go to Mr. T.W. Chan of the Advanced Manufacturing Technology Research Centre and Mr. S.Y. Lau of the Materials Engineering Laboratory for their technical support.

The financial support from the Hong Kong Polytechnic University for the provision of the research studentship is also greatly acknowledged.

Finally, special thanks go to my parents for their life-long love and extensive mental and financial support and to my important friends Miss J.Q. Dong, Mr. Q.J. Liu and Mr. L. Wei for their continuous support and encouragement during my Ph.D study. I would also like to thank all my friends who gave me support during my research study.

Table of Contents

List of Figures

List of Tables

Chapter 1

Introduction

1.1 Background of research

In engineering and product design, especially in the automotive and biomedical industries, there has always been great interest in joining dissimilar materials using a variety of means, such as laser, ultrasound and friction technologies [1-6]. The scope and demand of integrated material structures and products are increasing sharply chiefly due to many breakthroughs in fabrication technology. Indeed, many automobile and biomedical products are made of multi-components where various types of materials are used and the advantages of each material can be realised [7]. Frequently, the realisation of high functionality by compounding two different kinds of materials requires a reliable joining technique to produce reproducible high quality joints. Joining of plastics to metals is not new; conventionally, joining methods consist of adhesive bonding and mechanical fastening by screws or rivets [7, 8]. Nevertheless, these traditional techniques have their own drawbacks, mainly due to the incompatible structural, physical and chemical properties between these two types of materials. In the case of adhesive bonding, there are always concerns on environmental issues about the restriction of volatile organic compounds emissions. Other drawbacks include long processing times, high production costs and the limitations of shape and size, with the process requiring very stringent quality control. With regard to mechanical fastening,

inflexible design and low productivity are the two major shortcomings. To circumvent some of these problems, Katayama [9] developed a direct laser bonding technique for joining metals to plastics, namely laser-assisted metals and plastics (LAMP) joining. Indeed, LAMP has been employed to create strong joints between engineering metals (for example aluminium alloys, steel, stainless steel) and engineering plastics (for example polyethylene telephthalate PET and polyamide PA) using a near Gaussian Nd:YAG laser beam or a line shaped diode laser beam [9-12].

Notwithstanding the successes that have been achieved by a number of research studies on laser joining of metals to plastics [13-15], the exact joining mechanisms are still not fully understood. More importantly, the laser-induced bubbles, although assisting in creating an intimate contact surface between the metal and plastic parts by inducing high pressure in the molten plastic, they themselves are defects by nature, and therefore have a counter effect on the joint strength [16]. What is clear is that the presence of bubbles at the metal-plastic interface can seriously undermine the joint performance, but unfortunately, thus far, no in-depth study on methods of eliminating the bubbles, modelling and predicting the bubble distribution at the interfacial region can be found in the literature. With such a background in mind, this research is aiming at developing a new ultrasound-aided LAMP (U-LAMP) joining method that can address the bubble problem.

Ultrasound has been widely employed in cleaning [17-19], mixing [20-21], drilling [22-24] and welding [25-27] to increase the efficiency of the various processing technologies. In the present research on the U-LAMP joining method, ultrasound serves the purposes of (i) reducing the size of the

laser-generated bubbles and dispersing them in a discrete manner, or even eliminating the bubbles entirely, and (ii) generating a high positive pressure on the molten plastic and increasing its fluidity so as to cause it to have an intimate contact with the joining surface of the metal part, resulting in an enhancement of joint strength. Indeed, ultrasound has been found to be able to generate high positive and negative pressures on molten plastic materials, resulting in increased fluidity [28-31]. Moreover, an acoustic field can have a significant effect on the bubbles' trajectories as well as on the configuration and structure of the bubbles [32-36]. It is therefore envisaged that ultrasound is a promising aid that can be employed to address the bubble issue of LAMP.

1.2 Research objectives

The primary objective of this research is to develop a new ultrasound-aided laser method for joining metals to plastics with the ultimate aim of eliminating the laser-induced bubbles and achieving a significant improvement in joint strength. For the new joining process, an integrated system composed of an ultrasonic generator and a specimen clamping device have been designed and fabricated. The system allows the specimen to be vibrated under a longitudinal mode. The clamping system is so designed that a uniform force is applied to the specimen, with the force being adjustable. Moreover, different surface profiles of the ultrasonic transducer were used to study their effects on the acoustic pressure field of the molten plastic and the movement of bubbles in the joint.

With the new U-LAMP process, due to the acoustic energy, it is envisaged that the bubbles would be broken up and become smaller and

distributed more evenly in the joint, or even be eliminated with a well-designed ultrasonic transducer tool. As a result, the shear strength as well as the fatigue strength of the joint should be improved. However, before the full benefit of this new U-LAMP process can be realised, the theoretical aspects of the effects of the acoustic field on controlling the trajectories of the bubbles as well as an in-depth understanding of the joining mechanism must be gained. With this in mind, the following project objectives were defined:

(i) to design an ultrasonic system for the U-LAMP process that can resolve the bubble problem which is inherent with the conventional LAMP process;

(ii) to analyse and model the acoustic field in relation to the dynamic movement of bubbles in the joint;

(iii) to understand the joining mechanisms of metals to plastics under the combined actions of a laser and ultrasound;

(iv) to improve the mechanical properties of laser fabricated metal-plastic joints with the aid of ultrasound.

Chapter 2

Literature Review

U-LAMP joining is a new process developed in this project, which combines two seemingly unrelated techniques: laser welding and ultrasonic vibration. In this chapter, a literature review on some of the related aspects of laser welding, joining of metals to plastics and the application of ultrasonic vibration for material processing is presented.

2.1 Laser welding

Laser welding is an attractive method for joining plastics, metals, and plastics-to-metal because a laser beam is capable of focusing onto a relatively small area and reach a high power density, thus enabling materials to be easily melted even under a high processing speed. In order to achieve a satisfactory joint, the proper selection of beam power density, focal spot size, welding velocity and pulse duration is required. In this section, some background on laser joining is presented, including aspects such as laser output parameters, laser-material interaction, and in particularly the subject of laser-assisted joining of metals to plastics.

In pulse laser joining, the critical parameters for controlling the process and the quality of the joint are considered to be [37-38]:

(i) laser beam characteristics: wavelength, mode and polarisation, spot size, power intensity, pulse duration;

(ii) material properties: surface condition, composition, physical and thermal properties, etc.

(iii) welding setting: focal position, speed, dwell time and gap tolerance;

(iv) shielding gas protection: shroud design, composition, gas pressure/velocity.

In this study, the main variables in the joining experiment were the laser output parameters and the welding speed since they directly affect the melting and vaporisation of the plastic material.

2.1.1 Laser materials interaction

All the phenomena and events of heating, absorption, melting, evaporation, plasma formation, recoil pressure, Marangoni convection, and Kelvin-Helmholtz instabilities play a significant interrelated role in the complex laser-material interaction process [39]. In many cases, the complex interaction can be simplified and represented by a block diagram, as shown in Fig. 2.1 [40]. For the LAMP joining process, laser absorption at the metal surface and the melting and vaporisation of the plastic material are critical factors affecting the quality of the joint.

With regard to the application of the various lasers, sometimes it is convenient to present the information in the form of a relationship between laser intensity and interaction time, as shown in Fig. 2.2 [39]. For laser welding, the laser-material interaction falls into the categories of thermal effect or keyhole and plasma effects [41, 42]. In the case of the LAMP joining process, due to its nature, the keyhole and plasma effects can be ignored.

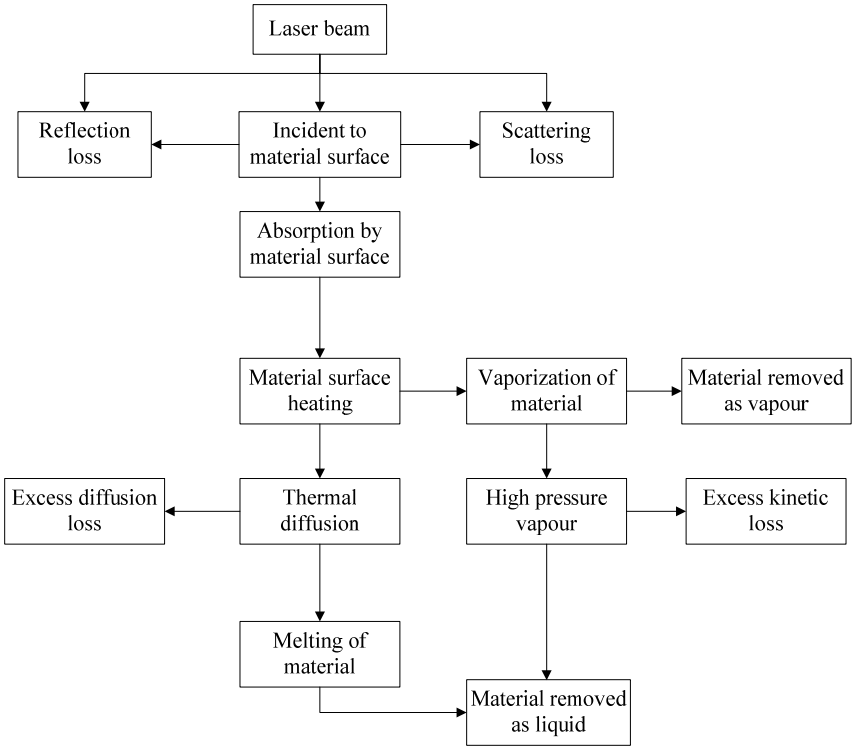

Fig. 2.1 Laser-material interaction events [40].

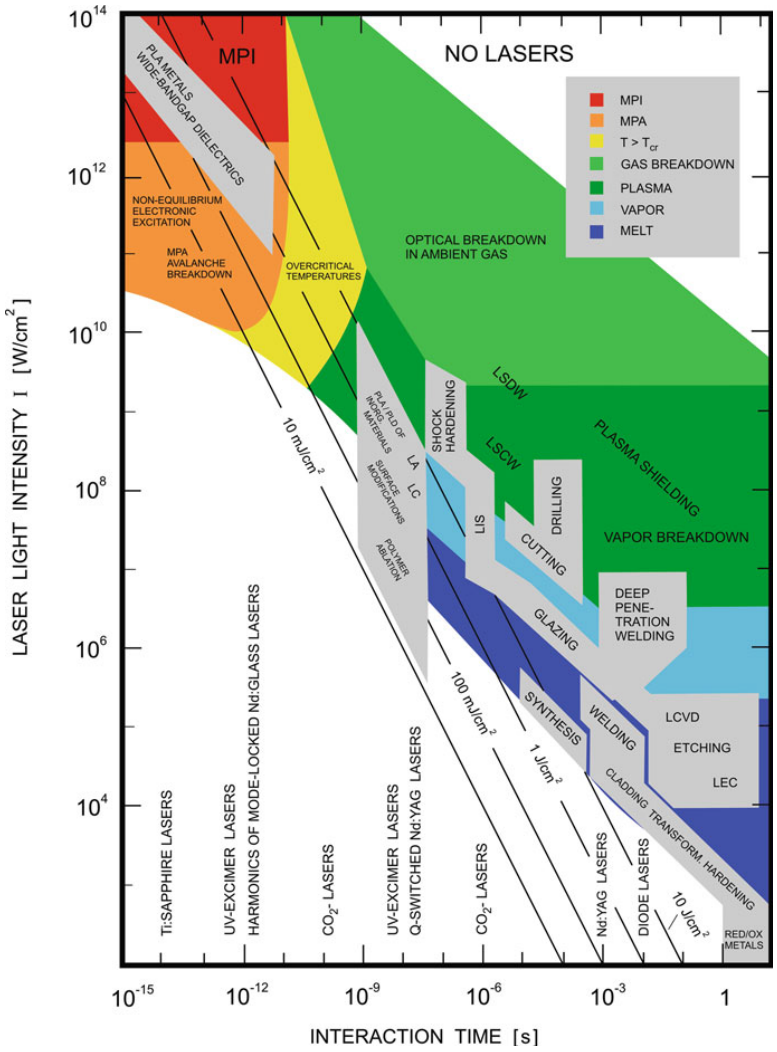

Fig. 2.2 The relationship between intensity and interaction time for different types of lasers and their intents [39].

2.1.2 Laser-assisted joining of metals to plastics

Since Gower et al. [1] successfully achieved the joining of a metal to polymer sandwich materials using laser technology, many researchers have paid serious attention to this emerging technology. In this section, the effects of bubbles formation, material properties, chemical bonds, joining parameters and surface preparation on joint properties and characteristics are summarised.

The laser joining mechanism between metals and plastics was first

studied by Katayama et al. [9] and Kawahito et al. [10] and they named this technique as the laser-assisted metal and plastic joining (LAMP). The principle of LAMP is simple; it uses laser light to heat up the metal-plastic interface, either by transmitting the laser through the plastic to generate heat at the interface or having the laser to heat up the metal part, and through thermal conduction causes the plastic at the interface to be heated up (Fig. 2.3 [43]). In both cases, the plastic at the interface is melted and partly decomposed; this results in the formation of bubbles in the molten plastic, which will stay in the solidified plastic zone. It has been proposed that the high pressure developed within laser-induced bubbles caused by rapid expansion would induce the molten plastic to have intimate contact with the metal surface and as a result, a strong mechanical anchor effect is attained. In addition, the interactive force of the chemical bond and Van der Waals forces are also thought to play an important role in securing a strong joint [44].

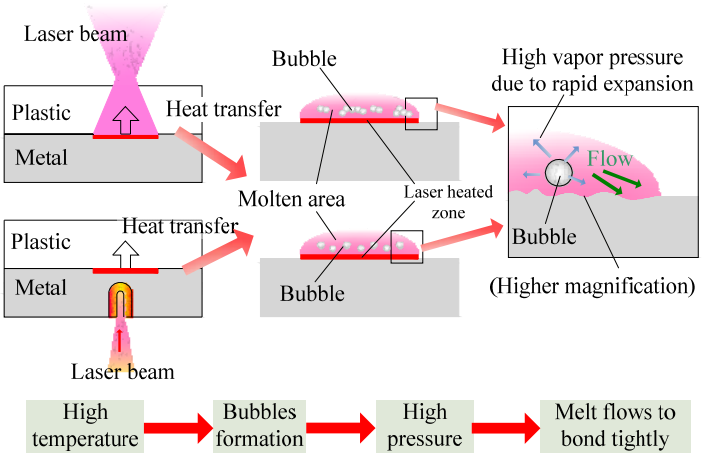

Fig. 2.3 A schematic diagram showing the LAMP joining process [43]

2.1.2.1 Laser induced bubbles

Kawahito et al. [11], Wahba et al. [16] and Katayama et al. [43] attributed the strong bond formed between the metal and the plastic materials partly to the formation of bubbles in the molten plastic during laser irradiation. They considered that the laser induced bubbles could induce high pressure in the molten plastic and force it into intimate contact with the metal surface, thus enabling the molten plastic to enter the concavities to accomplish anchoring effects, as illustrated in Fig. 2.3 [43]. Nevertheless, the bubbles are defects by nature. In order to further understand the laser joining mechanism, Wahba et al. [16] compared two lap joint configurations identified as an AZ91D thixo-moulded Mg specimen residing on top of a PET specimen and vice versa. Interestingly, the joint strength produced utilizing the second setup was two-third lower than that of the first one. The result was considered to be due to the difference in the bubble distribution. In the case where discrete bubbles are generated near the metal-plastic interface (Fig. 2.4a), a greater joint strength can be achieved because, unlike the networked bubble structure (Fig. 2.4b), the bubbles do not form a continuous line of weakness and also a relatively larger joint area is present between the bubbles. On the other hand, the lower bond strength of the second configuration is due to the formation of a networked bubble structure, so interfacial fracture can readily occur across the bubble network.

In addition, Tan et al. [45] studied the characteristics and formation mechanism of porosity during laser joining of steel and a carbon fibre reinforced polymer (CFRP). Two types of porosity morphologies were identified. Type I porosity had a smooth inner wall and a more cylindrical shape.

This kind of porosity appeared when the heat input was relatively high; it was located close to the bonding interface where the plastic part was in contact with the heated metal part. Its formation was due to decomposition of the CFRP and the generation of gaseous products of H_2O, NH_3, CO_2 and hydrocarbons. This kind of porosity can be completely suppressed by preventing decomposition of the plastic via controlling the processing parameters. On the other hand, type II porosity has a rough inner wall and can be found for all joining conditions. The porosity was normally located further away from the bonding interface, and was mainly confined to the regions where the polymer was solidified. This kind of porosity was a result of shrinkage of the molten polymer during solidification. It is possible to eliminate the porosity by exerting external pressure during solidification. Obviously, a low laser energy input can avoid the decomposition of plastic, but at the same time, the amount of molten plastic is reduced which can weaken the joint strength.

Turning to the effects of other laser processing parameters on bubble formation, a low welding speed with a high power input would result in large bubble sizes, with the joint strength decreaseing. Such a welding condition also leads to the formation of a connected bubble structure near the metal-plastic interface [46]. Tillmann et al. [46] also showed that the amount of bubbles formed in the joint has a significant impact on joint strength, which is in agreement with the findings of Cheon et al. [47]. The research results thus far have shown that the size, amount and distribution morphology of the bubbles are the key factors that affect the joint performance directly.

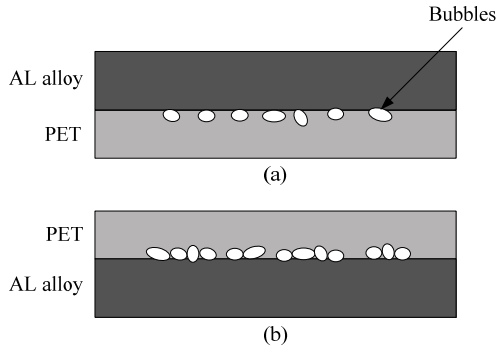

Fig 2.4 Illustrations of (a) individual bubbles morphology and (b) networked bubbles morphology [16].

2.1.2.2 Material properties

The joint strength of Cu/PET, A5052/PET and SUS304/PET, and the temperature field of the laser joint have been investigated by Farazila et al. [48]. The results showed that using the same laser output parameters, melting had obviously occurred to the aluminium alloy A5052 and stainless steel SUS304, while for the PET/Cu joint, no melting of the Cu metal was detected. This is due to the high melting point and high thermal conductivity of Cu, such that the temperature of the metal surface did not reach its melting point. While for the case of Al and stainless steel, due to the relatively low melting point of the aluminium alloy and the relatively low thermal conductivity of the steel, melting of the metals occurred with the latter metal to a much less extent. The study also showed that more scattered results in the joint strength were obtained if the metal did not melt. Obviously, any metal melting is undesirable in LAMP joining because this can cause severe decomposition and distortion of the plastic material, with a large amount of bubbles produced.

On the effect of polymer properties on joint strength when joining plastics to stainless steel. Miyashita et al. [49] reported that there was a large

difference in joint strength between PC/SUS304 and PET/SUS304, with values 2.1MPa and 6.5MPa, respectively. This can be contributed by the large difference in glass transition temperature of the two polymers [49], where PC can be melted more readily than PET when using the same laser energy. As a result, the PET/SUS304 joint has a greater bonding area, thus improving the failure load [49]. Surface tension is also an important property; polymers with high surface tension have large intermolecular forces exerted on the metal surface [50].

2.1.2.3 Chemical bonds

The chemical bonding created between the metal-plastic pair at the joint interface is also recognised as contributing to the overall joint strength. The research groups at Wayne State University and Fraunhofer [51-53] studied the interfacial bonding of Ti-coated glass/polyimide (TiG/PI) and Ti/PI) pairs quite extensively. Newaz et al. [52] showed that the tensile shear load of TiG/PI is approximately 1.5 times greater than that of Ti/PI. It was found that the failure of the Ti/PI joint occurred within the polyimide, while for TiG/PI, fracture occurred in the glass substrate [52]. This result implied that polyimide was firmly bonded to the Ti surface, resulting from the generation of strong Ti-C and Ti-O chemical bonds for both cases [52]. The induced bond strength appears to be comparable to that of a Ti-glass joint which is produced by the metal-coating process. On the contrary, while these joints have been immersed in an artificial cerebrospinal fluid (CSF) for 28 days, the Ti/Pi joint seems to be 1.2 times stronger than the TiG /PI joint, and both show strength reductions of 25% and 57%, respectively (Fig. 2.5). It has been reported that polyimide has a high water uptake (about 1% on average) and relatively high water transmission

rate (about 1.350 g·mm/m^2·day) [54]. This implies that water absorption via polyimide could promote oxidation at the interface [52, 55]. Since Ti-O bonds are generally unstable, they can be oxidized to generate a stable TiO_2, which contributes to a slight stronger bond in Ti/PI joints.

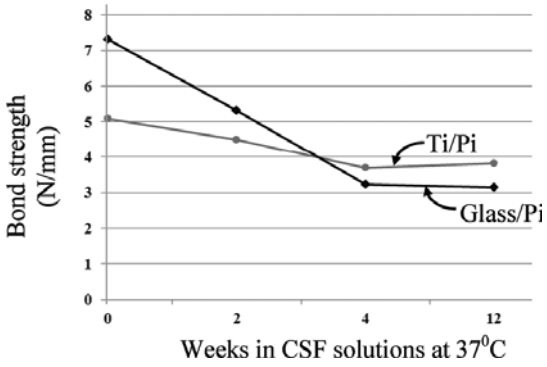

Fig. 2.5 The relationship between bond strength of titanium/polyimide and glass/polyimide micro-joints as a function of exposure time in CSF [52].

The evidence of the formation of new chemical bonds in the LAMP joining of metals to plastics was also studied by Katayama et al. [9], kawahito et al. [10] and Georgiev et al. [56, 57], who discovered the Ti-F and Ti-O bonds in the joining of Teflon FEP to Ti. Fig. 2.6 shows the Ti side of a Ti-Teflon FEP joined sample upon removing the polymer side. It illustrates that the Ti-F bond only exists within the interfacial region and the residual Teflon FEP indicates that a strong bond is established between these two materials [56]. As a consequence, the cohesive failure of the joint occurred in the plastic base material. However, if the joints are to be employed in a fluid, further studies on bond strength under a wet environment are required. Moreover, Kawahito et al. [10] also acquired a strong joint strength between a glassy metal

($Zr_{55}Al_{10}Ni_5Cu_{30}$) and PET. They reported two essential features which could promote a strong joint. Firstly, the formation of chemical bonds on the pre-existing zirconium oxide film is accompanied by the growth of an oxide film [10]. Secondly, the microstructure of the metal base near and in the joint area was in the state of amorphousness (disordered lattice structure); this was confirmed by X-ray diffraction (XRD) results [10]. In other words, the joint retains its amorphous characteristics even after being heated.

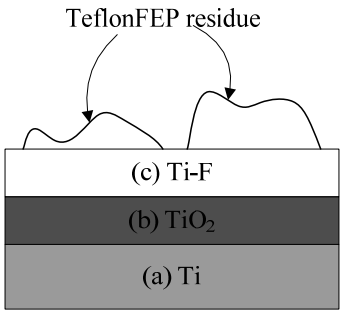

Fig. 2.6 A cross-section view of the titanium side of a bulk Ti/Teflon FEP sample after removing the polymer side [56].

2.1.2.4 Joining parameters

Formation of a sufficiently strong bond requires optimum laser energy with an appropriate scanning speed. Sufficient melting and wetting of the polymer to the metal part is crucial for achieving a high joint strength [46]. However, excessive heat input initiates overheating and pyrolysis of the polymer [2, 46], which leads to excessive bubble formation [46]. On the contrary, using a high scanning speed would result in insufficient laser-material interaction and would lead to weak joint strength [2, 46]. Normally, strong joint strength can be obtained when a moderate laser power and scanning speed are used [2, 46]. Figure 2.7 shows the effect of laser power on joint strength at

various scanning speeds [2].

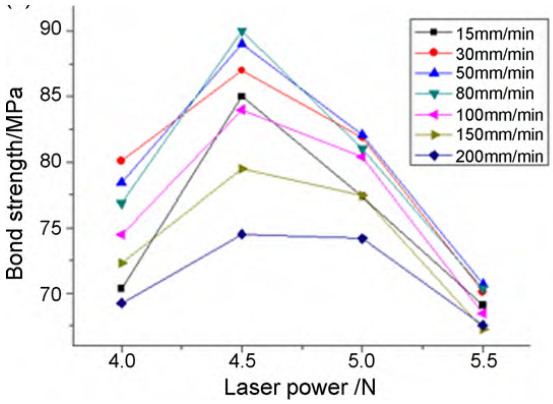

Fig. 2.7 Effect of laser power on joint strength at various scanning speeds [2].

2.1.2.5 Sample preparation

Metal Surface Patterning

It is predicted that surface patterning of the metal surface can increase the overall contact area of the join as well as to enhance the mechanical keying effect. To this end, Roesner et al. [50] pre-treated the metal surface using laser structuring. A groove pattern was created on the surface of a stainless steel specimen using a pulsed Nd:YAG laser. The results showed that the strength of the joint was dependent on the number of undercut structures as well as the width and distance between them. Taking a different approach, Wahba et al. [16] produced many pores on the surface of a Mg specimen prior to laser joining. As a result, an increase in tensile shear strength was obtained which was attributed to the mechanical anchor interlocking of the solidified plastic inside the pores. Recently, the effects of micro-patterning of the metal surface on failure behaviour have been studied in-depth. The pattern parameters studied include

the groove width and depth, and the space between the grooves, the focus angle of the laser beam and the direction with respect to the joint (Fig. 2.8) [58]. It was found that the space between the grooves was the key factor governing joint performance. On the other hand, the groove orientation did not show any noticeable effect on joint strength, but the alignment angle of grooves caused different failure modes.

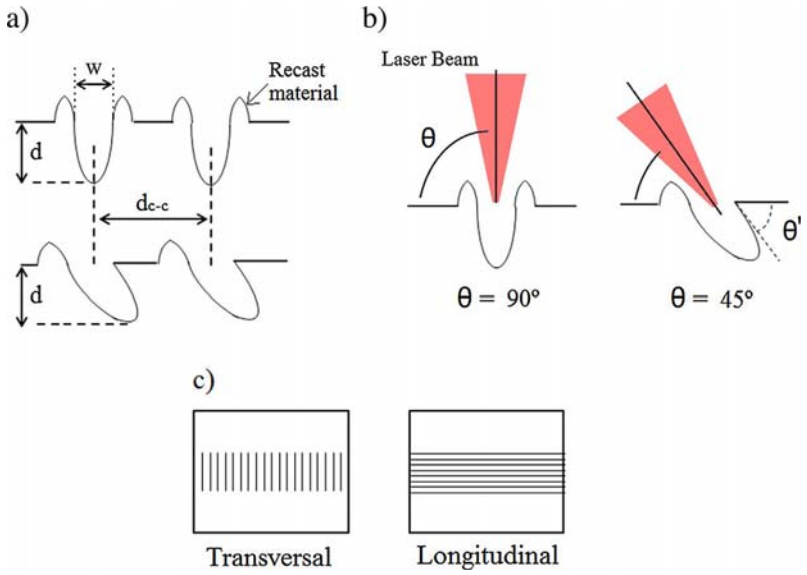

Fig. 2.8 Various metal microstructure patterns [58].

Surface treatment

The effects of sample surface pre-modification, including anodizing [44], and pre-oxidation [59], on joint mechanical performance have been studied. Yusof et al. [44] has investigated the effect of anodizing on the joint shear strength between an aluminium alloy (A5052) and PET film. The joint strength of the anodized A5052/PET was about 36% greater than that of the joint without any pre-treatment. The A5052 specimen was first cleaned in an

ultrasonic bath of acetone solution and then dipped into an electrolytic bath of sulphuric acid [44]. After cleaning with distilled water, the anodized sheet was immersed in a chemical solution for sealing the pores and, after the treatment, the reflectivity of the metal was reduced. This means that more laser energy is absorbed by the metal surface and results in a larger joint area, and this increases the shear failure resistance [44].

The positive effect of surface oxidation on the tensile shear strength of zinc-coated steel/ABS joints has been verified by Jung et al. [59]. The zinc oxide layer thickness produced was proportional to the joint strength as long as the strength of the oxide layer was greater than that of the jointed layer. The zinc oxide layer promoted reaction with the carbon of the ABS material (Zn-O-C), which was verified by means of SEM and XPS.

2.1.3 Summary

The literature review shows that laser-assisted joining is a potential method to join metals to plastic and can produce a strong bond. Different aspects of the joining process have been studied with an aim of improving joint strength, including process parameters, material properties and surface treatment. The joint's bubble and bonding characteristics for some widely studied metal-plastic pairs are summarised in Table 2.1, and it was found that the main concern of how to get rid of laser-induced bubbles has not been addressed.

It was suggested that the laser-induced bubbles serve as a means to create an intimate contact surface between the metal and plastic parts. However, it is apparent that the bubbles themselves are defects by nature. Until now, there

is still no effective method that can be used to eliminate the bubbles, or to model and predict the bubble distribution in the joint. What is also known is that the chemical bonds formed at the interface can enhance the joint strength, but few studies can be found as how to promote the generation of beneficial chemical bonds. Thus, in the light of these challenges, this research study seeks to address two critical issues, i.e. the elimination of bubbles and enhancing the chemical bonds in LAMP joining.

Table 2.1 Joint characteristics of some commonly studied metal-plastic pairs

Materials	Joint characteristics
Titanium and plastics	The chemical bonds of Ti-C and Ti-O were found in all types of polymers [60], except the cases of joining of Ti to TeflonFEP [56, 57] and KaptonFN [57] that resulted in the generation of Ti-O and Ti-F bonds.
Stainless steel (SUS304) and plastics	Formation of bubbles with optimum size and quantity were responsible for strong bonds in all joints [48].
Copper and plastics	Strong bond strength was attributed to the increment in surface roughness and heat absorptive by oxidation of cooper surface [48, 61].
Mg alloy and plastics	Formation of individual bubbles at the interfacial region produced higher bond strength than that of chains of interconnected bubbles morphology [16].

2.2 Other joining methods

2.2.1 Metal-plastic adhesion

Adhesive bonding is often employed in industrial applications. Generally, this process involves the following actions: (1) surface preparation by means of degreasing, chemical/plasma etching, sand blasting and sometimes the application of a primer under layer to increase adhesion; (2) an adhesive is spread over the joint and the bonding pairs are tightly gripped; (3) the bonding interfaces are kept under a sufficiently high clamping force; (4) the adhesive is cured and forms a bond; this process can be completed at elevated or room temperatures. The main benefits of this method are low stress concentrations, often resulting in an increase in fatigue resistance; however, the disadvantages are obvious: temperature sensitivity, high disposal costs and environmental concerns [62]. Therefore, bonding of metals to plastics by adhesion is rarely undertaken.

2.2.2 Friction joining of metals to plastics

Friction welding is a solid state joining technique, which can be considered to be an eco-joining method and has the advantages of reducing material waste as well as the elimination of harmful gas emissions that are normally associated with the fusion welding methods [63]. However, due the vast differences in the physical and thermal properties of metals and plastics, these two groups of dissimilar materials are not easy to be joined by the conventional friction joining process. In recent years, a specific friction stir welding (FSW) method, namely friction lap welding (FLW), has been developed for joining metal parts to plastic parts. This process differs from FSW

in that the non-consumable rotation probe of the former does not penetrate into the plastic part. Instead, the hard rotation probe only penetrates the top metal part and the heat generated by the friction action causes melting and decomposition of the underlying plastic part (Fig. 2.9) [63]. Upon the solidification of the molten plastic on the metal part, a joint is produced. This process has been successfully applied to join a number of metal-plastic pairs (AA6061/MC Nylon-6 [63], A5052/PET [64], AZ31/PPS-GF and AZ31/PPS-CF [65], Mg/PE [66], AA2024/carbon-fibre-reinforced polyphenylene sulfide [67]. These studies found that the key factors affecting joint properties were rotation rate [63-64], joining time [65, 67], joining pressure [63，67], joining speed [66] and surface treatments [66].

For the FLW, which is similar to the LAMP joining process, due to the decomposition of the plastic material; some bubbles are produced, as shown in Fig. 2.10 and Fig. 2.11. Although, these studies considered that the generation of bubbles caused the molten plastic to have an intimate contact with the metal surface due to the high pressure of the bubble [9-11, 16, 64], it was also found that the bubble itself is a defect by nature and it can reduce the shear strength of the joint depending on the size of the bubbles and their orientation [64]. Unfortunately, it is not easy to control the size and the orientation of the bubbles formed in the joining area.

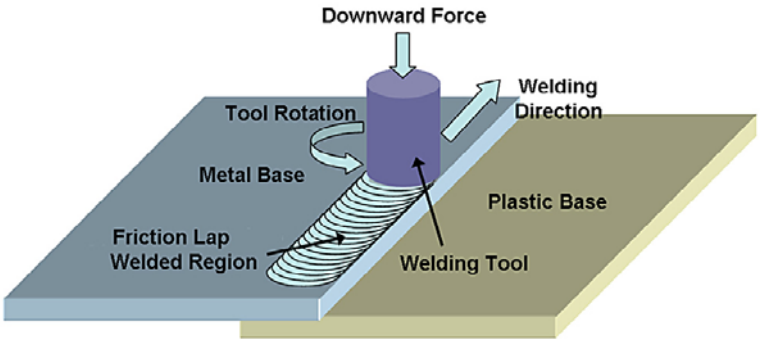

Fig. 2.9 A schematic scheme showing the principles of FLW [63].

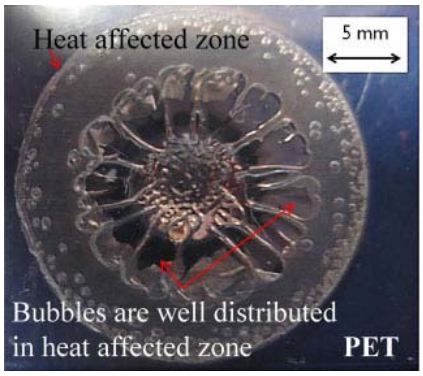

Fig. 2.10 Fracture surface of an A5052/PET specimen, showing the bubbles formed in the plastic material [64].

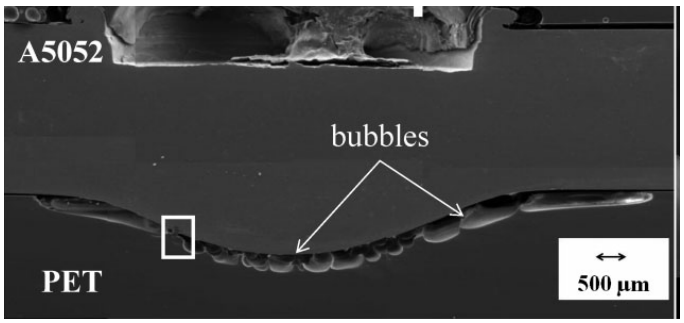

Fig. 2.11 A cross-sectional view of an A5052/PET specimen, showing the bubbles formed in the plastic material [64].

2.2.3 Ultrasonic joining of metals to plastics

Balle et al. [68, 69] used the ultrasonic lap joining technique to form strong joints between aluminium alloys and carbon fibre reinforced plastics/carbon fabrics without a plastic matrix (Fig. 2.12 (a), (b)), with the tensile shear strength of the joint reaching a level of over 30 MPa. A cross section of a joint formed between Al and the carbon fabric shows that ultrasonic energy can actually deform the Al and to have the carbon fibre engulfed without melting the Al (Fig. 2.12(c), (d)); moreover, no obvious damage of the carbon fibre reinforcement was observed. It is believed that the bonding between the two materials is mainly of a mechanical interlocking nature since no evidence of chemical bonds was presented. In order to improve the interlocking effect, Yeh et al. [70] employed the process of ultrasonic direct joining of laser surface-structured metal to thermoplastic. AA5052 sheets were structured by laser irradiation before joining. The results showed that the creation of micro-structure geometries on metal surfaces can enhance the long-term durability of metal/plastic hybrid joints. Although ultrasonic lap joining is a potential technique that can be used to join metal and plastic parts with a good joint strength, it should be noted that the shape of the joint often needs to be specifically designed in order to ensure that the ultrasonic energy is effectively directed to the jointing area.

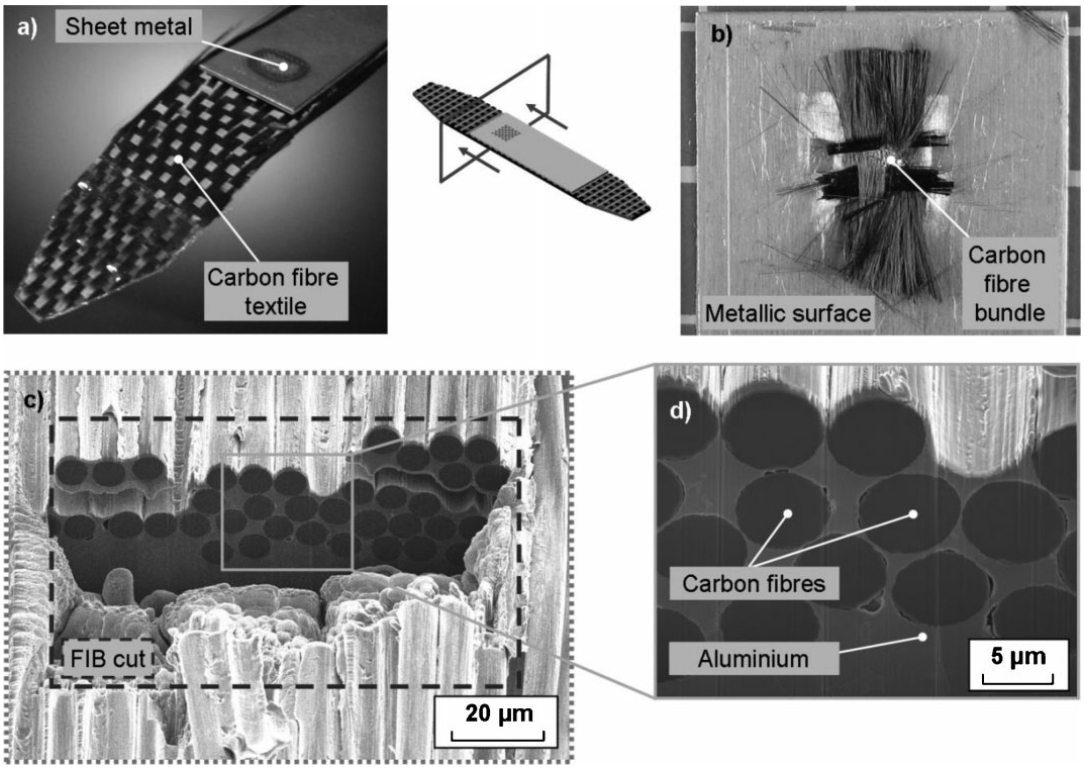

Fig. 2.12 Metal/carbon fibre textile-joint: (a) specimen, (b) back view of a prepared joint, (c) focused ion beam cut through the welding zone, and (d) SEM micrograph of the welding zone [68].

2.3 Effects of ultrasound on processing of molten polymers

As early as the 1950s, it was found that ultrasound can change the rheological properties of polymer melts [71], and since then the subject of ultrasound-assisted polymer processing has become an important field of research. The main applications of applying ultrasound in polymer processing are (i) improving the processing ability of polymers, (ii) assisting rubber devulcanization, and (iii) for developing new polymer materials. The main development stages of using ultrasound in polymer processing are summarised in Fig. 2.13.

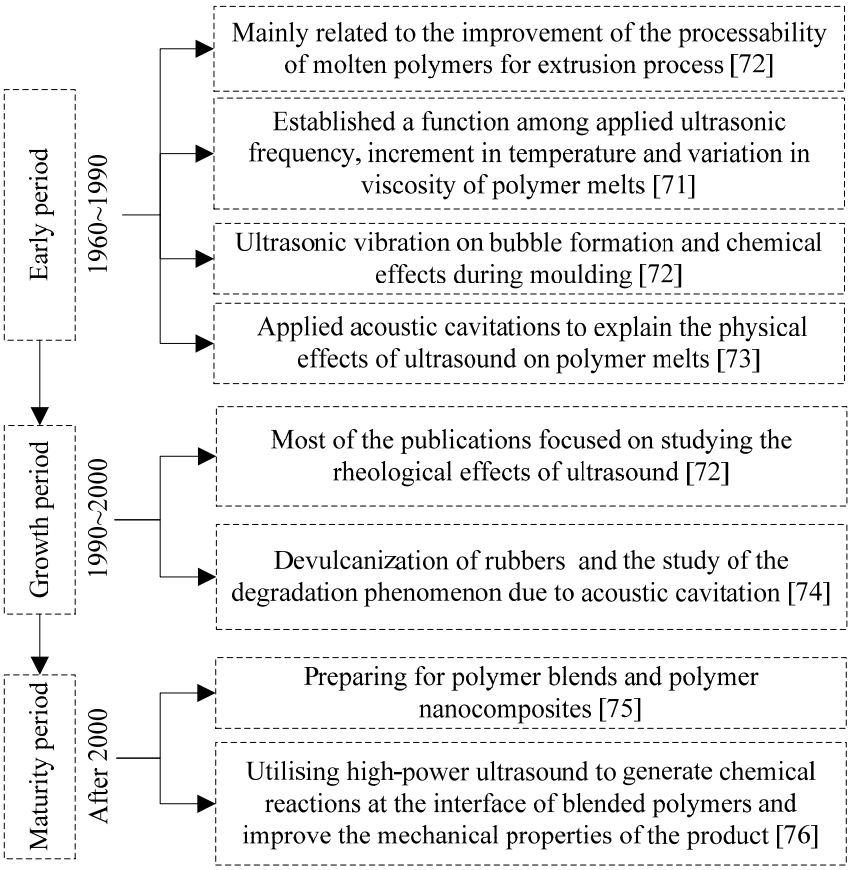

Fig. 2.13 The various development stages of using ultrasound in polymer processing.

The main physical effects of ultrasound on polymer melts are the creation of acoustic pressure and cavitation in the melt as well as the induction of molecular chain vibration. One of the major consequences of these effects is the degradation and fragmentation of the polymer molecular structure.

2.3.1 Acoustic cavitation

Ultrasound propagating in a liquid can cause pressure fluctuations, which leads to the generation of acoustic fields. Under the rarefaction phase of the acoustic field, cavities or voids, i.e. cavitation bubbles, are formed and each of them may grow until a maximum size is reached. The bubbles finally collapse violently in the form of certain stable and transient cavitational events

[72] during the compression phase, and is known as acoustic cavitation. If this happens in a Newtonian fluid, huge heat (~5000 K) and pressure (~500 atm) are created as well as micro-jets of fluid being generated during the collapse of the transient cavities, which leads to acoustic streaming flow and the introduction of shear forces to the melt [77].

Since the 1960s, Hughes and others [78] have made use of the acoustic cavitation phenomenon for medical applications (where the biological fluids or tissues are non-Newtonian fluids), and motivated many researchers to study the physics of the acoustic cavitation phenomenon. However, most of the analyses were still based on the properties of Newtonian fluids because of the difficulties encountered with non-Newtonian fluids. Similarly, in the study of ultrasonic treatment effects on polymer melts, the Newtonian fluid assumption has been widely employed despite the fact that the melts are actually non-Newtonian fluids [72]. Many researchers suggested that the acoustic streaming flow and shear forces created would impose a huge heat and pressure load on the polymer melt and could lead to the breaking up of the polymer chains/reduction of the polymer aggregates [79]. In addition, the ultrasonic input energy can even promote chemical reactions in some cases (mechanochemistry effect) [78]. Nonetheless, doubts were expressed on having acoustic cavitation occurring in all non-Newtonian fluids. Studies have found that by adding a water-soluble polymer in water can cause a reduction of the growth rate and a decrease in the size of the cavitation bubbles. This has a strong effect on the dynamic behaviour of the bubbles. In other words, a change in the elastic properties of a Newtonian fluid can delay bubble collapse occurring and can even suppress the formation of cavitation [80-83]. Indeed, Brujan et al. [84, 85] found that the dynamic

behaviour of cavitation bubbles was considerably different in polymer solutions and in water. This can be illustrated by the schematic diagram shown in Fig.2.14. In the case of a non-Newtonian polymer fluid, most of the potential energy is used up to provide an additional resistance to the extensional-lateral flow, which is conferred by the surrounding polymer molecules solution. As a result, the bubble collapse will therefore be suppressed in polymer solutions. Moreover, if a transient bubble contains a high level of gas content it may collapse and then rebound, and this action confers a significant change in pressure on the surrounding liquid. Such a phenomenon, if occurring in the LAMP joining process, can assist the molten plastic to have a more intimate contact with the metal part.

Having reviewed the phenomenon of acoustic cavitation, it is considered that cavitation is unlikely to occur in the U-LAMP joining process because the ultrasonic device would not create a strong acoustic field in the molten plastic. However, it will cause the melt as a whole to experience a change in pressure with time. This effect is elaborated in Section 7.4.2. Nonetheless, vapour bubbles will still be formed during U-LAMP joining due to the boiling of the molten plastic by the laser light.

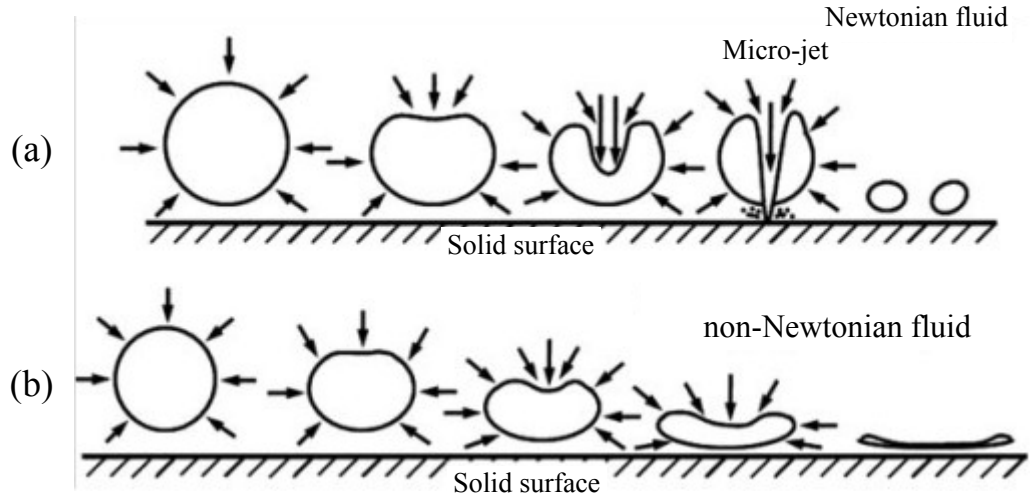

Fig. 2.14 A schematic diagram showing the dynamics behaviour of ultrasound-induced cavitation in (a) a Newtonian fluid, and (b) in a non-Newtonian fluid near a solid boundary [85].

2.3.2 Vibration of molecular chains

A few studies [86-89] claimed that the effects of ultrasound on the physical and chemical properties of polymers are through molecular chain/segment vibration rather than the result of acoustic cavitation. When ultrasonic fields propagate in a polymer melt, the relaxation time of the molten polymer is much longer than an oscillation cycle of the field. In other words, when polymer molecules are subjected to high frequency acoustic waves or loading, they are unable to relax in time. Therefore, random scission of the polymer chain can occur. The higher the molecular weight of the polymer, the easier will the chain scission occur. Normally, this degradation process is more pronounced at the beginning of the application of the ultrasound since there are more long chains present initially.

2.3.3 Acoustic pressure

In U-LAMP joining, one of the consequences of the ultrasonic vibration effect is the exertion of extra pressure on the molten plastic [90]. The induced pressure change in the molten plastic has an effect on the movement of the laser-induced vapour bubbles and this is an important subject matter covered in this research study. To study this, the ultrasonic transducer tools with different surface profiles were used.

2.4 Bubbles behaviour under ultrasonic standing wave

The acoustic radiation force together with hydrodynamic forces is known to be capable of causing gas bubbles in a fluid to expand and contract in a nonlinear manner, eventually resulting in a net displacement of the bubble in the wave propagation direction. Indeed, bubble movement/translation under the influence of an acoustic radiation force has been widely used for many medical applications, in particular drug delivery with the bubble being a substance carrier, where drugs can be transported to the target site via the radiation force [91, 92].

The acoustic radiation force known as the Bjerknes force acting on bubbles was first reported by Bjerknes [93], which is caused by a spatial acoustic pressure gradient and is classified into primary and secondary Bjerknes forces. The primary Bjerknes force results from the “primary” external wave that covers the acoustic pressure gradient as well as the average oscillation of one bubble within one cycle. The secondary Bjerknes force is the result of the “secondary” wave emited by the vibration of the bubbles. Some years later,

Eller [94] derived a mathematical expression for evaluating the average force acting on a sphere-shaped bubble under the action of a standing wave, and the theory was supported by experimental results. Based on the analysis, it was found that if the radius of a bubble is larger than the resonant radius, then the primary Bjerknes force can cause the bubble to travel towards a pressure node. On the contrary, if the radius is smaller than the resonant value, the bubbles will travel towards a pressure anti-node. The pressure amplitude of the sound emitted by a bubble decreases inversely proportional to the distance from another bubble since a bubble acts as a point-sound-source. This acoustic pressure gradient leads to the secondary Bjerknes force and many early studies have examined this force. Other studies showed that the secondary Bjerknes force can cause the phenomenon associated with acoustic cavitation, specifically the mutual attraction and coalescence of bubbles [95, 96].

In classical theory concerning bubble dynamics, the direction of the Bjerknes force for two interacting bubbles is determined based on the relationship between the resonance frequency of the bubbles and the driving frequency. If the driving frequency does fall between the resonance frequencies of the two interacting bubbles, the force will be repulsive; otherwise, it will be attractive. It was noted that the interacting bubbles under the influence of acoustic waves exhibit rather complicated dynamics that cannot simply be explained by classical theories. Indeed, it was found that many factors, such as viscous effects [97], nonlinear vibration of the bubbles [98, 99], and variations of resonance frequencies [100, 101] also affect the bubble dynamics.

In order to understand the translational movement of bubbles in an acoustic field, various models have been developed. Crum [102] presented a

simple model to determine the secondary Bjerknes force between two vibrating bubbles with the aid of photography, assuming that the bubble's radius only changed linearly with small amplitudes of pulsation. The study also found that the relative velocity of two approaching bubbles underwent a secondary Bjerknes force and demonstrated that the experimental results were in good agreement with the theoretical analysis. A few years after Kornfeld's publication [95], Doinikov [103] derived a refined mathematical expression to express the secondary Bjerknes force between two vibrating bubbles in a viscous incompressible fluid. This was an advancement over previous theories, since Doinikov studied the phenomenon in a more realistic manner and took acoustic streaming into account as well as treating the Bjerknes secondary forces to be unequal and unopposed. Further improvement has been made by permitting bubble translational oscillations and vertical motion of the liquid. With these considerations, it was found that small bubbles are capable of repelling each other even when driven below the resonance frequency due to viscous effects; this is not in agreement with the classical Bjerknes theory [97]. On the other hand, Parlitz et al. [104] employed a particle model to study the structures of the bubbles, in that an individual bubble could be treated as a moving particle and all the forces acting on bubbles, namely, acoustic radiation forces, drag forces and mass, could be maintained in balance. This particle model can be used to simulate the structure of bubbles and the trajectory of a pair of interacting bubbles in both travelling and standing wave fields. However, the changes in volume of the bubbles during oscillations have not been taken into account in this model, which leads to errors in the translational motion of the bubbles.

Moreover, other studies have been conducted to examine the resonance

response in multi-bubble systems [105] and in compressible liquids [106]. Doinikov [107] applied Lagrangian mechanics to derive a mathematical formula that coupled the radial and translational motions to express the secondary Bjerknes force for a vibrating spherical bubble in a viscous compressible fluid under strong acoustic fields. In addition, the effect of viscosity on the mutual force was also studied. Recently, based on Doinikov's model, Xi et al. [108] analysed the movements of bubbles close to a solid boundary in a weak standing wave field, which could be used to explain the translations of multi-bubble through considering a balance of all the forces acting on the bubbles in a liquid. More recently, Jiao et al. [109] applied the coupled model established by Doinikov [107] to simulate the trajectory of bubbles in water, which was in good agreement with the experiment.

With regard to the study of bubble dynamics in viscous fluids, thus far, there is a need to find an established model for describing bubble behaviour in a viscous compressible polymer melt. Nonetheless, Doinikov's coupled model [107] for determining the secondary Bjerknes force between two vibrating bubbles in a viscous compressible fluid, which has been verified by experimental studies, is considered to be acceptable for the study of the translation path of bubbles in the U-LAMP joining process.

Chapter 3

Experimental Details

3.1 Ultrasound-aided laser joining system

The ultrasound-aided laser joining system (Fig. 3.1) consists of a 300 W Nd:YAG pulsed laser which has a multi-mode beam distribution, an ultrasonic vibration system with longitudinal mode of vibration which is capable of vibrating at a frequency of 28 kHz and an apparatus clamping system. Some of the major specifications for this equipment are listed in Tables 3.1 and 3.2.

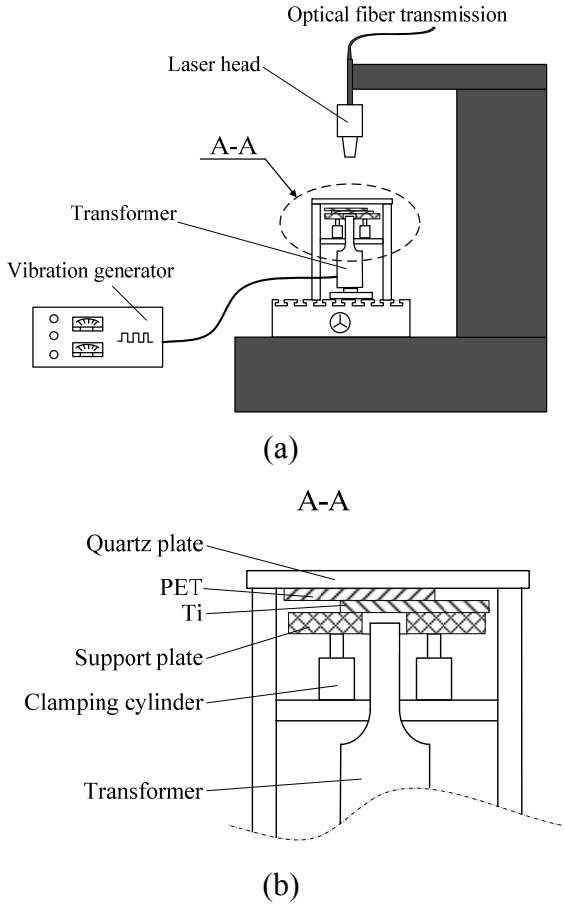

Fig. 3.1 (a) The ultrasound-aided laser joining system; (b) more details of A-A.

Table 3.1 The specifications of the laser welding machine

Parameter	Value
Beam wavelength	1064 nm
Output Average Power	300 W
Pulse energy	< 90 J
Pulse duration	0.01 ~ 50 ms
Pulse frequency	1~200 Hz
Minimum beam diameter	0.6 mm
Working stroke of workbench	300×300×300 mm

Table 3.2 The specifications of the ultrasonic system

Parameter	Value
Vibration frequency	28 kHz
Output Power	500 W
Transducer	Piezoelectric
Vibration Amplitude of transducer	＜30 μm

3.2 The ultrasonic device

Ultrasonic devices range from small table-top-sized applications to machines with large capacity. In addition to the physical size, the level of power for a particular machine tool is also an important consideration. All ultrasonic devices have similar major elements regardless of the geometry and power rating. The most important elements are the power supply, the transducer, the transformer (horn) and the tool [110].

3.2.1 The ultrasonic generator and transducer

An ultrasonic generator is used to convert low frequency (about 50 Hz) electrical signals to high frequency electrical signal (approx. 28 kHz). The transducer then converts the electrical energy into mechanical vibration. The power supplied depends on the size of the transducer [111]. Generally, based on different principles of operation, the transducers can be divided into two types: magnetostrictive and piezoelectric [112]. The magnetostrictive transducer allows oscillations to be transmitted through a wide frequency band due to its lower mechanical quality factor Q (m) value that is a measurement of the sharpness of the energy peak value [113]. In addition, it allows tool wear and improves the design flexibility of the transformer. However, its energy convection efficiency is low with high electrical losses (about 55–60%). The piezoelectric transducer has higher energy efficiency (90–96%), and also can generate higher vibration intensities than the magnetostrictive transducer [114]. Therefore, a piezoelectric transducer is used for the construction of the U-LAMP joining system in this project. In order to transfer the vibration energy from the transducer to the workpiece, an appropriate coupler, a transformer, is mounted between the transducer and the workpiece.

3.2.2 The transformer (transducer tool)

The velocity transformer (or the transducer tool) is used to transmit the ultrasonic waves to the workpiece with a reasonable high ultrasonic intensity and suitable displacement amplitude. One of the most popular velocity transformers, the double quarter-wave cylindrical step transformer, was used in this research. Its configuration is simple and can be conveniently produced.

Basically, it consists of two cylinders; each of which is a quarter of a wave length of the sound wave travelling in the transformer material. The two cylinders are joined together to form a transformer, as shown in Fig. 3.2. One end of the transformer, i.e. the input end, is rigidly attached to the transducer, whereas the other end, i.e. the output end, has the tool firmly attached on it, as shown in Fig. 3.3. During laser joining, the ultrasonic system excites the metal sheet at a frequency of 28 kHz, and the vibration amplitude of the workpiece is of the order of 2~10 μm. Since the workpiece is vibrating at exactly the frequency of the system, the workpiece can be regarded as a waveguide [115].

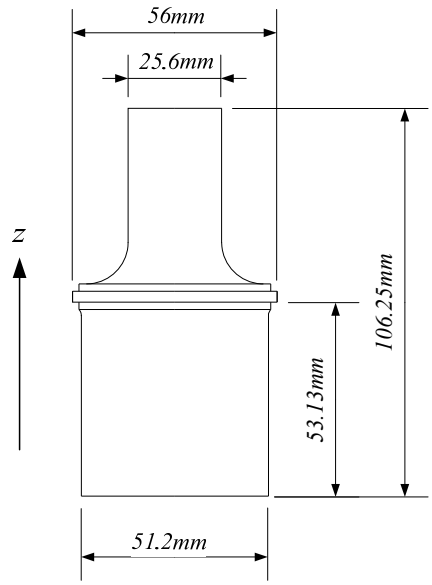

Fig. 3.2 Sketch of a double quarter wave cylinder transformer.

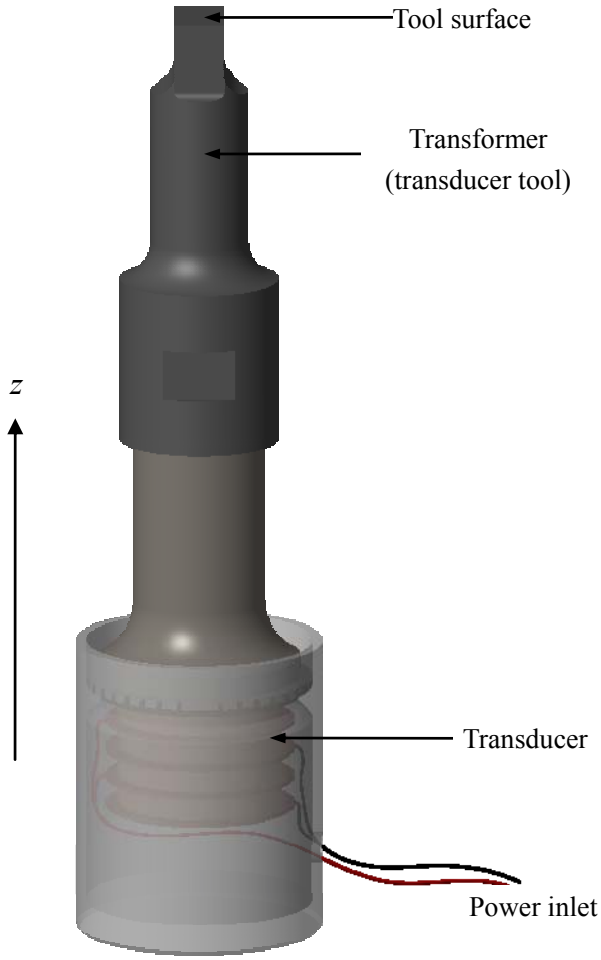

Fig. 3.3 The ultrasonic transformer is attached to the transducer.

If the input end diameter of the transformer is D_i and its output end diameter is D_o, then the diameter D of the transformer along the z-axis is given by [115, 116]:

$$\begin{cases} D = D_i & \left(0 < z \le \lambda/4\right) \\ D = D_o & \left(\lambda/4 < z < \lambda/2\right) \end{cases} \tag{3.1}$$

Also, the velocity u of the transformer can be expressed by the following equations (Fig.3.4):

$$\begin{cases} u = u_i \cos\dfrac{\pi z}{\lambda} & \left(0 < z \le \lambda/4\right) \\ u = \left(\dfrac{D_i}{D_o}\right)^2 u_i \cos\dfrac{\pi z}{\lambda} & \left(\lambda/4 < z < \lambda/2\right) \end{cases} \tag{3.2}$$

$$u_o = \left(\frac{D_i}{D_o}\right)^2 u_i \tag{3.3}$$

where u_i and u_o are the velocities at the input and output end surfaces of the transformer, respectively; and λ is equal to the wavelength of the sound propagating in the material. Hence, for a half-wave transformer the velocity transformation ratio R_u is equal to:

$$R_u = \frac{u_o}{u_i} = \left(\frac{D_i}{D_o}\right)^2 \tag{3.4}$$

Similarly, the displacement amplitude transformation ratio R_ξ is equal to:

$$R_\xi = \frac{\xi_o}{\xi_i} = \frac{u_o}{u_i} = \left(\frac{D_i}{D_o}\right)^2 \tag{3.5}$$

where ξ_i and ξ_o are the displacement amplitudes at the input and output end surfaces of the transformer, respectively.

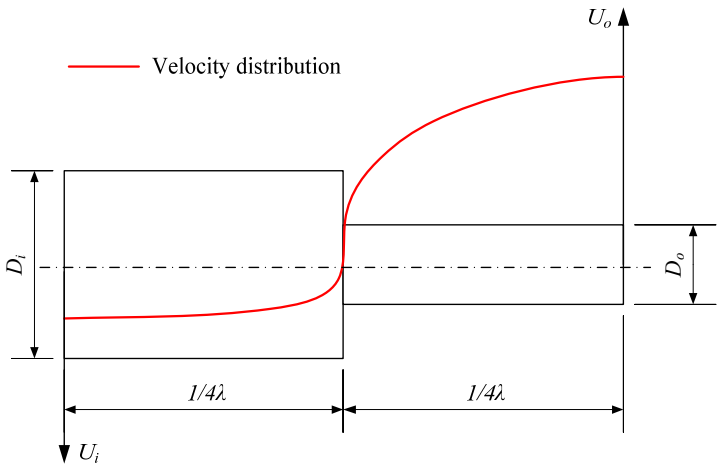

Fig. 3.4 The double quarter wave cylinder transformer and its velocity.

3.2.3 Longitudinal mode of vibration

As the output surface of the transformer is larger than that of the joining area, in this case, the velocity equation for the workpiece described previously can also be used, i.e. Eq. (3.2) [115].

$$\begin{cases} u = u_i \cos\dfrac{\pi z}{\lambda} & \left(0 < z \le \lambda/4\right) \\ u = \left(\dfrac{D_i}{D_o}\right)^2 u_i \cos\dfrac{\pi z}{\lambda} & \left(\lambda/4 < z < \lambda/2\right) \end{cases} \tag{3.6}$$

In this study, the thickness of the workpiece is 1 mm, which is much less than the wavelength, therefore the velocity of the workpiece u_w can be considered as uniform and can be determined by applying the following equation:

$$u_w = \left(\frac{D_i}{D_o} \right)^2 u_i \tag{3.7}$$

3.3 The coupling between ultrasonic device and specimen

A sufficient clamping force between the metal and plastic parts is necessary in order to achieve a good contact surface. To perform U-LAMP joining, a plastic sheet is placed on top of the metal sheet, and ultrasonic vibration is required to transmit to this metal-plastic coupled specimen through the output end of the transformer. Two coupling approaches for transmitting the vibration to the specimen have been considered; they are the fixed structure design and the detached structure design.

3.3.1 Ultrasonic-specimen fixed design

The ultrasonic-specimen fixed design is a clamping system which behaves as a forced vibration system (Fig. 3.5). The design consists of a loading plate, an upper fixture plate and four fixing screws. The loading plate is firmly inserted into the top surface of the transformer by a screw. The loading plate would normally be larger than the workpiece. In this study, the diameter is ϕ100 mm with a thickness of 10 mm. The workpiece is placed between the loading and the fixture plates which are fixed by four screws. Although this coupling design is simple, its disadvantage is that it is a forced vibration system, which means that the vibration amplitude is very small, generally less than 3 μm. This can lead to an uneven clamping force acting on the specimen. Moreover, the geometry of the loading plate affects the vibration amplitude. If the size of the loading plate increases, the vibration amplitude of the workpiece decreases.

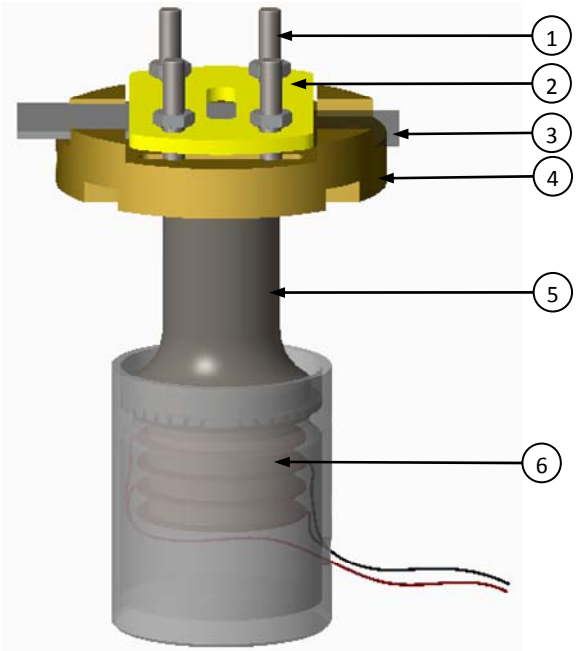

Fig. 3.5 The ultrasonic-specimen fixed design.

(1. fixture screws 2. fixture plate 3. workpiece 4. loading plate 5. transformer 6. transducer)

3.3.2 Ultrasonic-specimen detached design

The ultrasonic-specimen detached design works as a resonance system, and is shown in Fig. 3.1(b). In this design, the transformer is used to intensify the vibration with its tool surface covering the entire joining area. The clamping apparatus consist of a covering plate which is made of quartz glass, a clamping plate which is moveable, two cylinders, two supporting plates and a PLC controller (Fig. 3.6). Such a clamping system provides an effective means to control the clamping force acting on the workpiece to be joined. The workpiece is placed between the covering and clamping plates. There is enough space between the two supporting plates for the transformer to travel upwards and apply vibration onto the workpiece. Since the top end of the transformer is not

rigidly fixed onto the workpiece, this ultrasonic-specimen coupling design is regarded as a detached structure design. During the U-LAMP joining process, the two cylinders drive the clamping plate upwards till it is locked in with the workpiece. Then, the central cylinder drives the transducer upwards and brings the transformer in touch with the workpiece (i.e. the upper face of the metal sheet that is to be laser joined). Compared to the ultrasonic-specimen fixed clamping system, this detached structure design has the following advantages.

(i) A larger vibration amplitude can be achieved.

(ii) An even clamping force between the metal and plastic sheets (i.e. the workpiece) can be obtained and is easily controlled.

(iii) There is no specific geometry limitation on the workpiece.

A weakness of this design is that it works well for plastics that have high transmittances to the laser. However, the advantages outweigh the disadvantage. Based on above analysis, the ultrasonic-specimen detached clamping design was adopted in this study. The ultrasonic duration with sine wave and the clamping force of 0.6 MPa were employed.

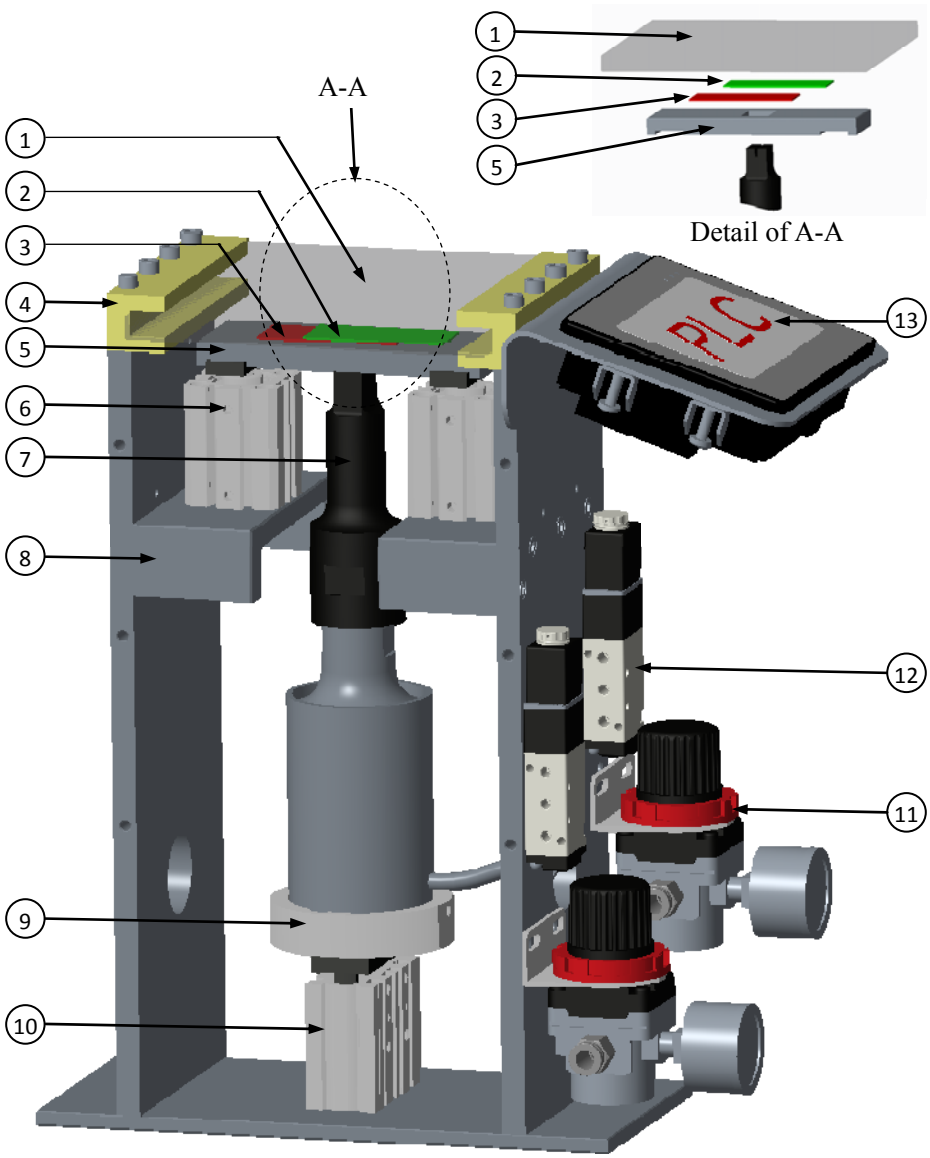

1. quartz plate; 2. plastic sheet; 3. metal sheet; 4. chute; 5. clamping plate; 6. clamping cylinders; 7. transformer; 8. support plate; 9. cylinder bracket; 10. cylinder; 11. pressure regulating valves; 12. solenoid valves; 13. PLC controller

(a)

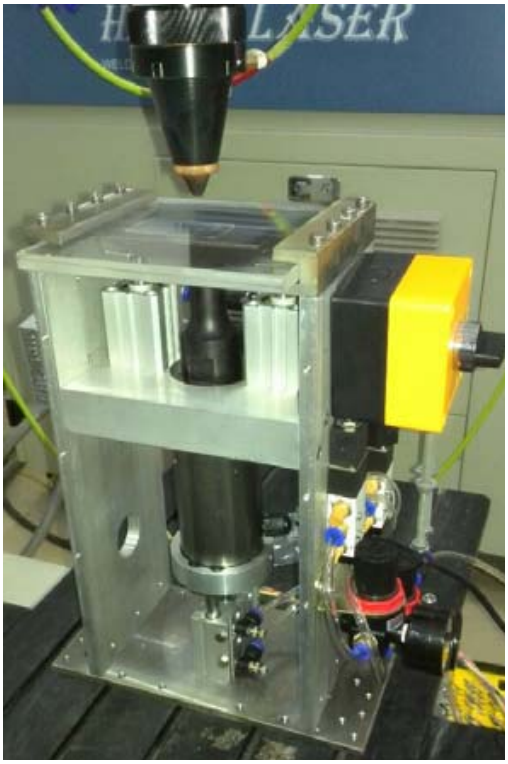

(b)

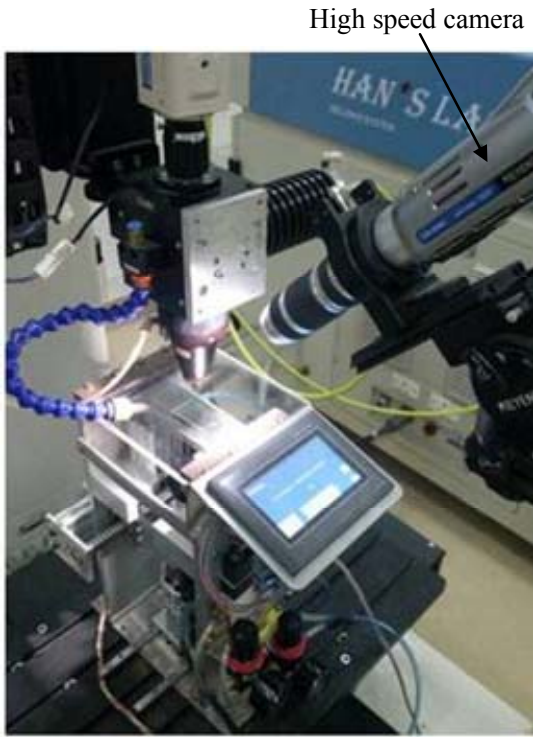

(c)

Fig. 3.6 (a) A schematic diagram showing the ultrasonic detached structure design, (b) front view of the design set-up, (c) the set up with a high speed camera.

3.4 Materials

In the present study, both LAMP and U-LAMP joining are conducted for a Titanium (Ti)/Polyethylene Terephthalate (PET) pair. Since there have been some detailed studies on the chemical bond nature of laser joined Ti/plastics pairs, it is convenient to compare the results of this study to those found in the open literature. Both Ti and PET materials used in this study were purchased from Goodfellow Ltd..

Titanium and its alloys are widely applied in aerospace equipment and medical applications (e.g. replacement hip joints) due to their excellent properties, such as lightness, high strength and excellent corrosion resistance. In this study, Ti sheet (ASTM B265 Grade 1) was selected as one of the metallic materials to be joined to plastic. The nominal composition and some of its physical, thermal and mechanical properties are given in Table 3.3 and Table 3.4, respectively.

Table 3.3 Nominal composition of the Ti sheet

Element	wt %
Aluminium	0.5
Cobalt	0.002
Copper	0.2
Chromium	0.5
Nickel	0.5
Iron	0.3
Magnesium	0.02
Manganese	0.5
Silicon	0.2
Tin	0.2
Vanadium	0.5
Tantalum	0.01
Titanium	Balance

Table 3.4 Titanium properties

Properties	Notation	Value
Melting point	T_m	1933 K
Boiling point	T_b	3560 K
Latent heat of fusion	L_m	3.65×10^5 J/kg
Latent heat of evapouration	L_v	8.893×10^6 J/kg
Density	ρ_m	4.5×10^3 kg/m^3
Thermal conductivity	K_{sm}	21.9 W/m K
Specific heat	C_{psm}	523 J/kg K
Coefficient of thermal expansion	K_{em}	$8.9\times10^{-}6$ K^{-1}
Tensile strength	σ_{lm}	230-460 MPa

PET is the plastic material to be joined to Ti. It is a stiff, hard and strong dimensionally stable material with low water absorption rate. It also has good gas permeable resistance properties and good chemical resistance, and is an important material for medical devices. The material can be tailored made to exhibit different percentages of crystallinity, i.e., the material can be produced with an amorphous structure or with a fairly high crystalline structure. It can therefore be highly transparent or opaque. Its chemical formula is -OCH_2-CH2OCOC6H4CO-, which contains the ester carbonyl group. Since the carbon atoms in ester carbonyl are active, chemical reactions should readily occur between PET and the metal part to be joined. Some of its physical, thermal, optical, chemical, mechanical properties are listed in Table 3.5.

The joining face of the titanium specimens was ground finished with emery paper (#320 and #1200) to remove oxide films from the surface, and all the Ti and PET specimens were cleaned in an ultrasonic bath in ethanol for 10 minutes prior to joining.

Table 3.5 PET properties

Properties	Notation	Value
Density	ρ_P	1.3-1.4×10^3 kg/m^3
Thermal conductivity	K_{sP}	0.15-0.4 W/m K
Specific heat	C_{psP}	1200-1350 J/kg K
Coefficient of thermal expansion	K_{eP}	20-60×10^{-6} K^{-1}
Tensile strength	σ_{lP}	80 MPa
Transmission index	κ_t	92-95%
Water absorption equilibrium	κ_a	＜0.7%
Lower working temperature	T_l	213-233 K
Upper working temperature	T_u	388-443 K
Heat-deflection temperature (at 0.45 MPa)	$T_{d0.45}$	388 K
Heat-deflection temperature (at 1.8 MPa)	$T_{d1.8}$	353 K

3.5 Design of experiments

The main objective of the experiment design is to demonstrate the advantages of U-LAMP over LAMP. Firstly, some experiments were conducted for LAMP to establish a baseline to use as a starting point for comparison. Previous studies showed that the most influential parameter affecting the amount of laser-induced bubbles produced was the laser power [45, 46]. With this in mind, the first set of experiments was employed to determine the level of laser power that initiates extensive decomposition of PET with widespread formation of bubbles. Having determined these laser power levels, two more sets of experiments, one at a lower and one at a higher

power level than this, were conducted. The former aims to study the effect of ultrasonic vibration on joint performance without the influence of laser-induced bubble. The main attention was focused on the chemical bonding of the joint interface. The latter was intended to study the possibilities of using ultrasonic vibration to eliminate bubbles in the joint with an aim to further improve joint performance. To this end, transducer tools with different surface profiles were used.

3.5.1 The LAMP process

A transmission joining configuration of the LAMP process together with the dimensions of the specimen is shown in Fig. 3.7. The joining parameters and the designation of specimens are listed in Table 3.6 and Table 3.7, respectively. During the joining process, the laser beam passed through the covering plate (quartz glass) and the PET sheet, which has a high transmittance of about 92% at λ_{laser} = 1064 nm, before reaching the surface of the Ti sheet.

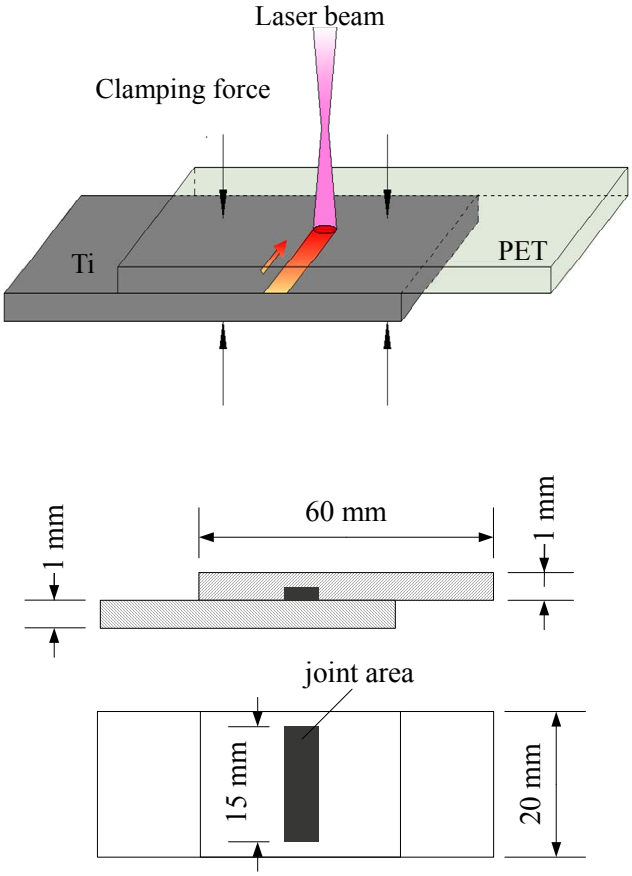

Fig. 3.7 A schematic diagram showing the transmission joining configuration of the Ti-PET pair.

Table 3.6 LAMP Joining Parameters

Parameters	Value
Laser beam focal length	25 mm
Laser power	35/45/60/80 W
Pulse duration	8 ms
Welding speed	4 mm/s

Table 3.7 Designation of Specimens

LAMP (Without ultrasonic vibration)	Sample 1	LP_35W
	Sample 2	LP_45W
	Sample 3	LP_60W
	Sample 4	LP_80W

LP = laser power (W)

3.5.2 Ultrasound-aided laser joining

To perform U-LAMP joining, the plastic sheet is placed on top of the metal sheet. During the joining process, the two cylinders drive the clamping plate to firmly hold the metal and plastic parts together. Then the cylinder drives the transformer to pass through the hole of the clamping plate, which is in contact with the bottom surface of the titanium sheet. The laser beam passes through the quartz plate and the plastic sheet, and when it reaches the metal surface, heat is absorbed by the metal, and as a result, the contact surface of the plastic sheet is melted. When ultrasonic vibration is applied, an extra pressure with an oscillation effect acts on the molten plastic and forcing it to have an intimate contact with the Ti sheet. A schematic diagram of the U-LAMP process is presented in Fig. 3.8.

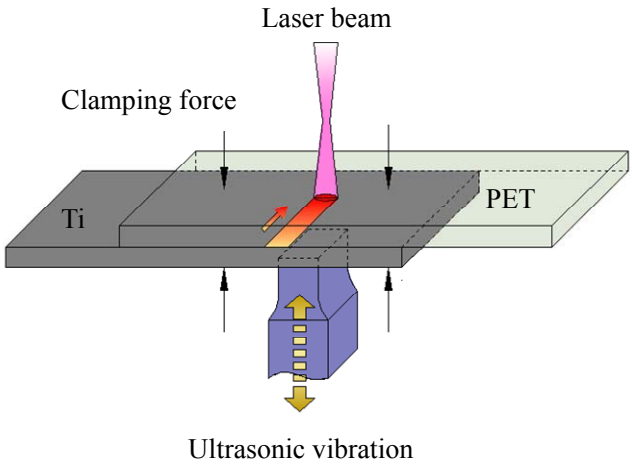

Fig. 3.8 A schematic diagram showing the ultrasound-aided laser joining process.

3.5.2.1 U-LAMP joining with low laser power

Previous studies showed that for the LAMP joining process, if the laser energy input was too low, the joint strength would also be low. On the other hand, if the laser energy input was increased, the joint strength would be increased [2, 46], but this could cause the formation of numerous bubbles to be formed in the joint.

It is envisaged that by the conjoint action of the laser and ultrasound, a better contact between the metal surface and molten plastic can be achieved. This means that a low laser power can be used to avoid decomposition of the polymer and the formation of bubbles, and due to better surface contact, the mechanical locking effect is enhanced. As a result, high joint strength can be obtained. Moreover, the vibration energy input to the joint enhances the chemical reactions between the molten plastic and the metal surface due to the more vigorous molecular chain vibration. This also leads to a stronger joint

interface with a higher failure load. It is therefore believed that with the aid of ultrasonic vibration, a strong interface can be formed between the metal and plastic parts, even without the assistance from laser induced bubbles to create intimate contact.

In this phase of the study, an ultrasonic tool with a smooth surface was used (Fig. 3.9); the ultrasonic device was operated at a duty cycle of 30% (Fig. 3.10). The tool was made of Cr12 steel. The joining parameters used in the experiment are given in Table 3.8. Based on some preliminary results of the LAMP joining experiment, the laser power was kept to below 30 W to avoid decomposition of the polymer and the formation of excessive laser-induced bubbles, which are detrimental to joint strength [46, 48-49]. The joint was created by using one pass of the laser beam only. This produced a lap-joint length of about 15 mm. The designations of the specimens are listed in Table 3.9.

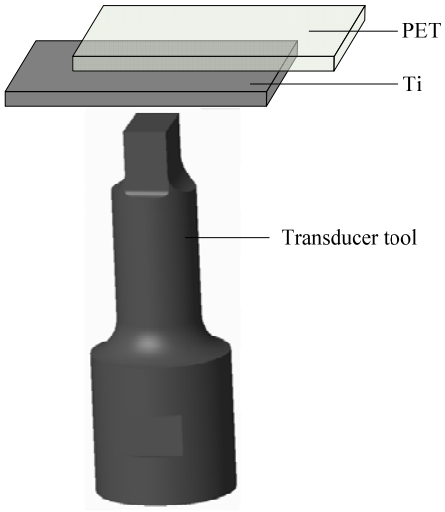

Fig. 3.9 The ultrasonic transducer with a smooth flat tool surface.

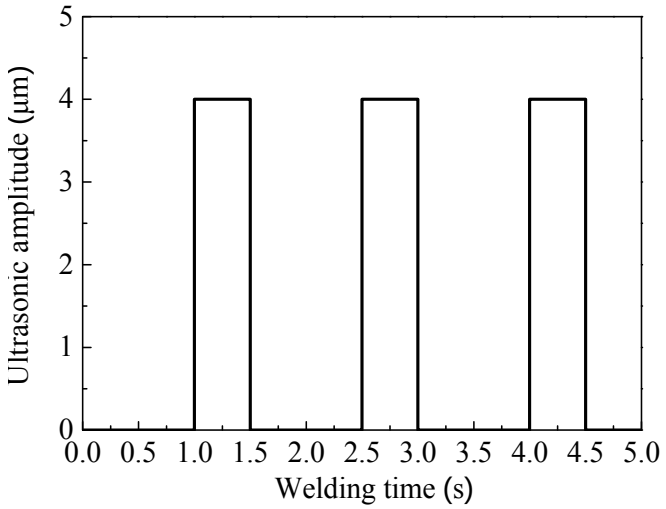

Fig. 3.10 The ultrasonic pulse operation mode (duty cycle of 30%).

Table 3.8 U-LAMP joining parameters

Parameters	Value
Laser beam focal length	25 mm
Laser power	30 W
Pulse duration	8 ms
Welding speed	4 mm/s
Ultrasonic vibration amplitude	0/2/4/6 μm

Table 3.9 Designation of specimens

LAMP (Without ultrasonic vibration)	Specimen A1	LP_30W_UA_0
	Specimen A2	LP_45W_UA_0
U-LAMP (With ultrasonic vibration)	Specimen B	LP_30W_UA_2
	Specimen C	LP_30W_UA_4
	Specimen D	LP_30W_UA_6

LP = laser power (W)

UA = Ultrasonic vibration amplitude (μm)

3.5.2.2 Using a three holes transducer tool

A three-blind-holes transducer tool (Fig. 3.11) was used to study the effect of the pressure field on the movement of bubbles in the molten pool during U-LAMP joining. The purpose of having cavities in the transducer tool is to create a relatively low pressure region in the molten plastic zone above the location of the cavities when ultrasonic vibration is applied. It is considered that the differential pressure effect would cause bubbles to move to the low pressure regions in the molten plastic pool. During laser joining, the ultrasonic device operates at a duty cycle of 20% (Fig. 3.12). Other joining parameters used are listed in Table 3.10.

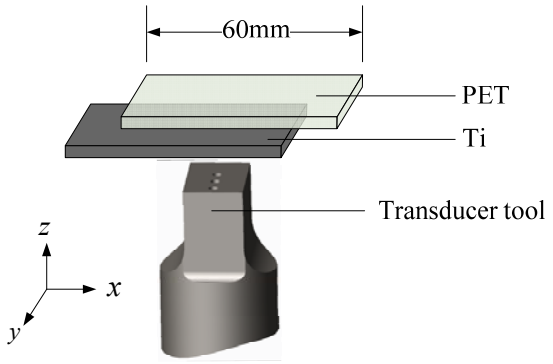

(a)

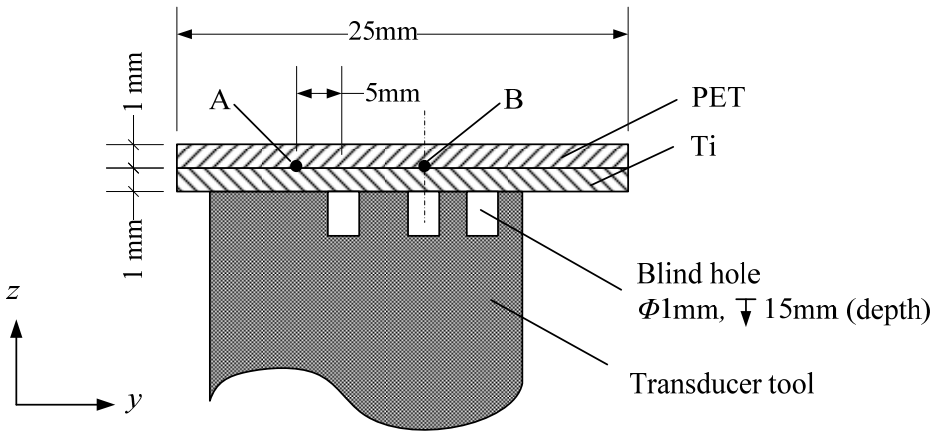

(b)

Fig. 3.11 Ultrasonic transducer tool with circular blind holes.

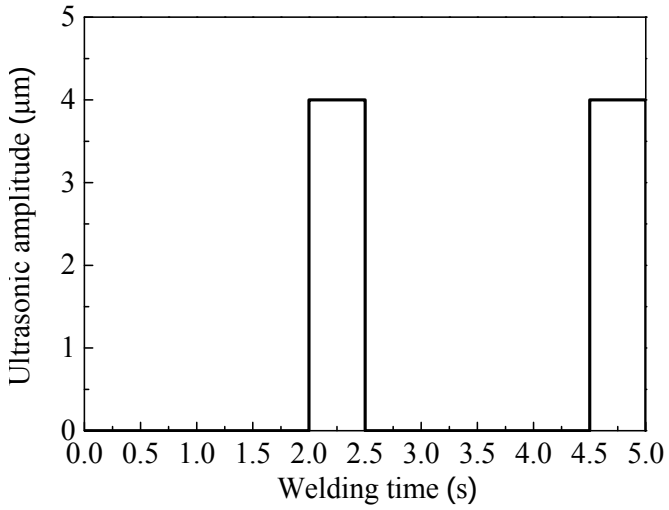

Fig. 3.12 The ultrasonic pulse operation mode (duty cycle of 20%).

Table 3.10 Joining parameters

Parameters	Value
Laser focal length	25 mm
Laser power	55 W
Welding speed	4 mm/s
Laser pulse frequency	20 Hz
Pulse duration	8 ms
Laser spot diameter	∅ 2.5 mm
Transducer vibration amplitude	4 μm

3.5.2.3 Using an open channel transducer tool

A tool with an open channel was designed (Fig. 3.13), aimed at creating a low pressure path for the laser induced bubbles to escape from the molten pool when ultrasonic vibration is applied. The ultrasonic device was operated at a duty cycle of 20%. Other joining parameters used are listed in Table 3.11. The analysis of the influence of the pressure field on the

movement of bubbles is presented in Section 8.4.

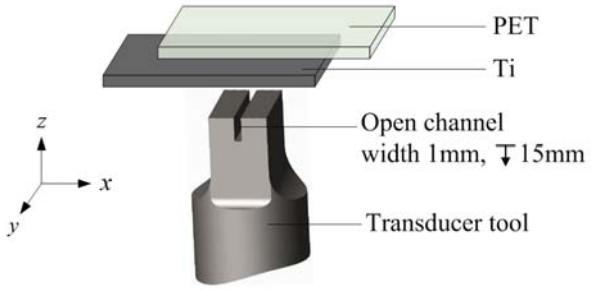

Fig. 3.13 Ultrasonic transducer tool with an open channel.

Table 3.11 Joining parameters

Parameters	Value
Laser focal length	25 mm
Laser power	45/55/65/75 W
Welding speed	2/4/6 mm/s
Laser pulse frequency	15/20/25 Hz
Pulse duration	8 ms
Laser spot diameter	∅ 2.5 mm
Transducer vibration amplitude	4 μm
Ultrasonic duty cycle	20%
Channel offset	0/ 0.5/1.5 mm

3.6 Joint properties evaluation

3.6.1 Microstructural characterization

Both optical microscopy and scanning electron microscopy (SEM) were used to study the characteristics of the bubbles formed in the joint. For the SEM study, the longitudinal sections of the specimens were examined (Fig.

3.14). The section of the specimen was prepared by mechanical grinding and polishing with 1 μm diamond paste.

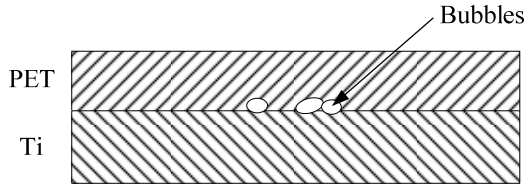

Fig. 3.14 A schematic diagram showing a longitudinal section of a joint.

3.6.2 Chemical bonding analysis

X-ray photoelectron spectroscopy (XPS) was utilized to obtain information on the chemical bonds at the Ti/PET interface. For the XPS analysis, the Ti/PET joined samples were separated at the interface by means of a shear test, and analysis was performed on the Ti part of the joint. To reveal the nature of the chemical bonding across the interface, ion milling was used to gradually thin the solidified PET layer till reaching the Ti substrate. This was accomplished using XPS analysis after each layer of plastic was removed, until Ti was detected. This level was designated d=0. The distances referred to in this research are measured from d=0. Then the Ti side of the sample was loaded onto the UHV chamber (pressure = 10^{-6} Pa) of the XPS analyser (ULVAC-PHI 1800) with an achromatic Al Kα X-ray source. Low-resolution spectra were recorded by using a pass energy of 187.85 eV; for high-resolution spectra, the pass energy was 58.7 eV. The analysis was conducted in a semi-quantitative mode, and the XPS data were fitted by using the curve-fitting program of the XPSPEAK software. The following constraints have been used for optimal fitting:

- The value of each peak position of the various compounds referred to the data in the published reference. However, since the uncertainty inherent in data obtained from experiment, an adjustment of ± 0.15 eV to each peak position, following the reference [2,117-118] was used.
- At all depths, the position of each peak was kept constant for various specimens. For example, for all depths, the Ti-C position was set to ~454.8 ± 0.15 eV for all specimens.
- The optimal spectral baseline as well as the peaks was described by the Shirley background.
- A Gaussian (80%)–Lorentzian (20%) combination function was applied to determine the curve-resolved shape.

3.6.3 Tensile shear test

An Instron testing machine with a load cell of 2 kN was applied to measure the tensile shear load of the joints at room temperature. Testing was conducted with a crosshead speed of 0.5 mm/min; the tensile shear load and displacement were measured. In order to ensure the reliability of the results, five samples were tested for each joining condition. The set-up for both the tensile test and the fatigue test is shown in Fig. 3.15.

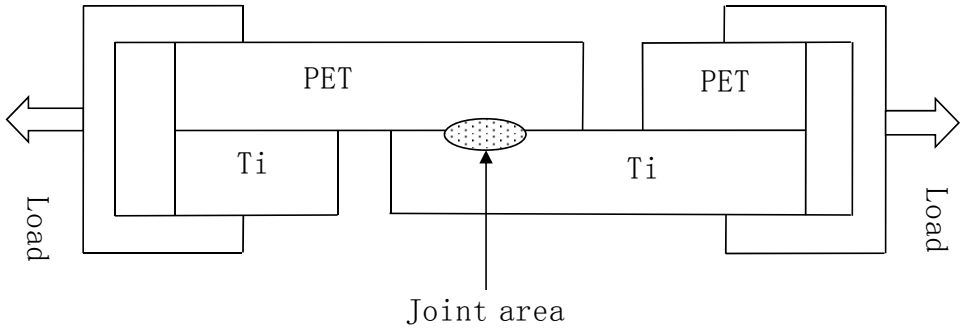

Fig. 3.15 A schematic diagram showing the set-up of the tensile test and the fatigue test.

3.6.4 Fatigue test

To compare the fatigue properties of the LAMP and U-LAMP joined specimens at room temperature conditions, load-controlled fatigue tests were performed using a servo-hydraulic MTS machine. The specimens were produced using laser powers of 30 W and 55 W (Tables 3.11), while other joining parameters were kept constant (pulsed frequency 20 Hz, pulsed duration 8 ms, welding speed 4 mm/s). These two laser power conditions were chosen because the fatigue properties of the specimens, with porosity and without obvious porosity, can be compared. The specimens were fatigue-tested using a tensile sinusoidal load with mean stress 200 N, load ratio (R_{load}) 0.25 and frequency (f) 2 Hz. The test was stopped when the specimen failed or if a specimen survived more than six hundred thousand cycles. Five samples were tested for each joining condition.

Chapter 4

Joining Titanium to PET Using LAMP

4.1 Introduction

Before a full study of joining Ti to PET using U-LAMP was conducted, a pilot study on LAMP was performed to establish the effects of laser power on joint performance, including bubble appearance, joint strength and interfacial chemical bonds. This information, in particular, the level of laser power that initiates bubble formation, is important for designing experimental conditions for the U-LAMP process.

4.2 Joint appearance as a function of laser power

The LAMP joined samples were examined using an optical microscope. Fig. 4.1 shows the joint appearance as a function of laser power. For Sample 1, which was processed using a laser power of 35 W, no sizeable porosity was observed in the joint. It was found that if a laser power higher than 45 W was used, a large amount of bubbles developed in the weld zone. The development of bubbles is due to the excessive laser energy causing decomposition of the polymer. It was noticed that the distribution of bubbles was also altered as the laser power was increased. It was observed that when a relatively low laser power was used, most of the bubbles formed along the centreline of the weld where the laser energy was concentrated, and the bubbles appeared in a somewhat discrete manner (Sample 2). When the laser power increased, more

bubbles were produced and would agglomerate and were connected (Sample 3). However, when the laser power was further increased, the bubbles became somewhat broken up (Sample 4). This could be due to the violent decomposition effect that occurs at high laser energies, causing the break up of the bubbles. The amount of bubbles (projected area) measured for samples, 2, 3 and 4, were 6.2 mm^2, 12.5 mm^2 and 34.8 mm^2 respectively.

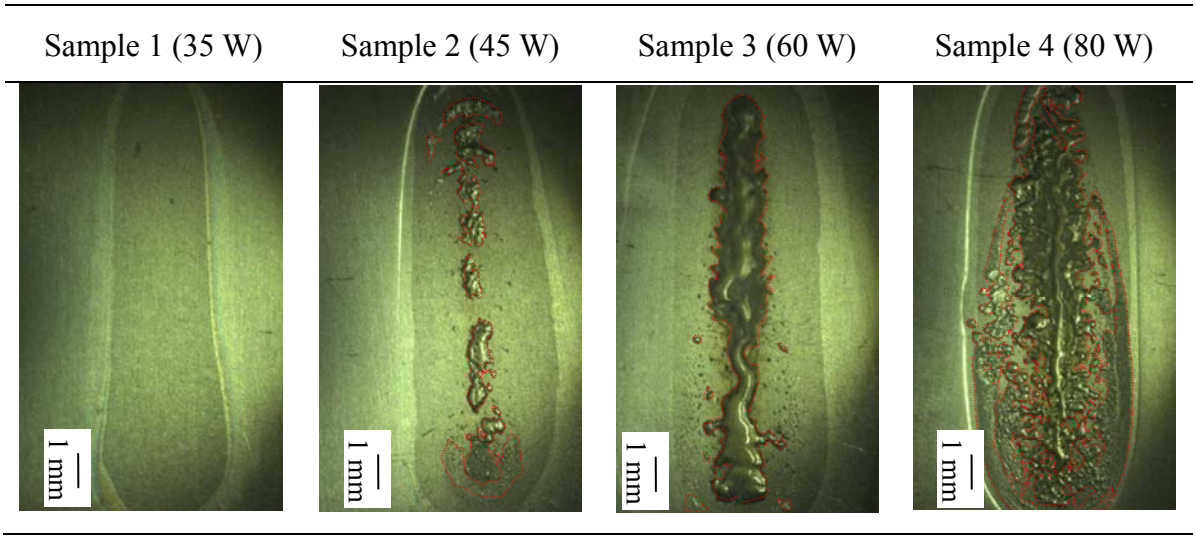

Fig. 4.1 Typical joint appearances as a function of laser power.

4.3 Effect of laser power on chemical bonds

4.3.1 C1s XPS spectra

The XPS analysis was performed in the centre of the joint. Fig. 4.2 shows a typical high-resolution XPS spectrum of the C1s lines of a laser joined sample which was ion milled to a depth just before reaching the chemically reacted PET/Ti interface zone (designated d=0). The C1s peak at ~284.8 eV, likely caused by the C–C bond [2], [117], and the peaks at approximately 286.6 eV and 289.2 eV correspond to –O–CH_2– and –C=O which originate from the

PET chain [117]. No new peak was detected, which suggests that some residual PET covered the Ti side after mechanical separation.

Fig. 4.3 shows the high-resolution C1s XPS spectra obtained from the Ti side of the four joined samples, produced by using different laser powers, after further ion-milling from (d=0) to different depths across the Ti/PET interface. After ion-milling to a further depth of 60 nm, a new weak peak at a binding energy of ~281.7 eV, believed to be the Ti–C bond [2], appeared in the spectra of the four samples. Mian [53] discovered that Ti atoms reacted with both five and six-fold rings of polyimide when laser welding polyimide to Ti sheets. It is likely that titanium atoms can react with the phenyl carbons of PET, just as in the case of polyimide/Ti produced by laser joining [53]. The areas of the C–C and Ti–C peaks decreased with increasing the ion milling depth (Fig. 4.3). The peaks at 284.8 eV and 281.7 eV disappeared at sputtering depths of 480 nm and 750 nm, respectively (Fig. 4.3 (a)). This suggests that the thickness of the interface containing the laser generated Ti–C bonds is between 720 nm and 750 nm. The data shown in Fig. 4.3 indicate that the thickness of the interface containing the new Ti–C chemical bond is ~1230 nm in Sample 2, ~1500 nm in Sample 3, and ~1710 nm in Sample 4. This indicates that more Ti atoms react with the phenyl carbons when the laser input energy is increased. Fig. 4.4 shows the relationship between laser power and the estimated Ti-C boned interface thickness.

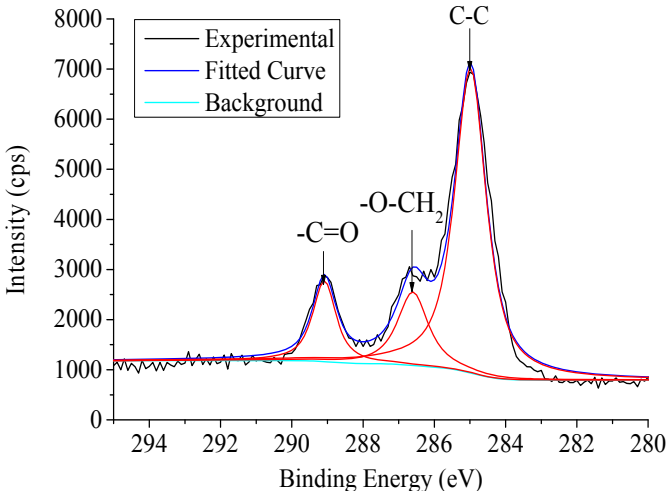

Fig. 4.2 Curve fitting of the C1s high resolution XPS spectra obtained from the Ti side of a laser joined sample.

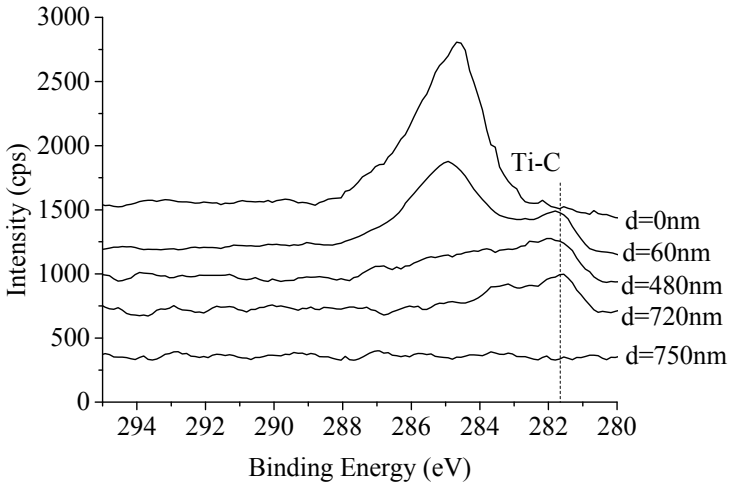

(a)

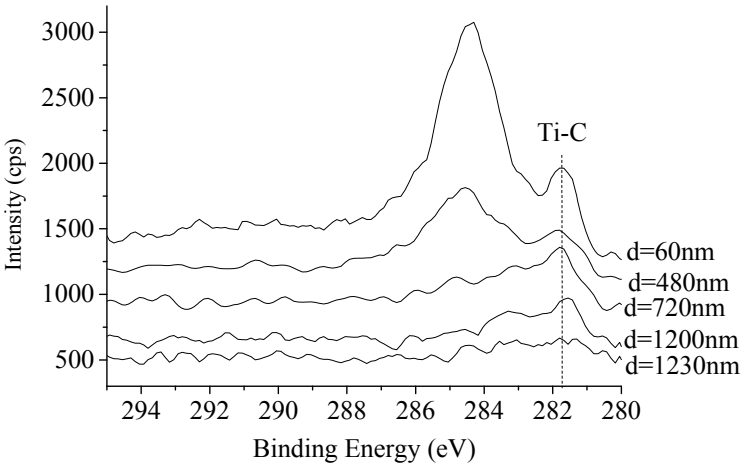

(b)

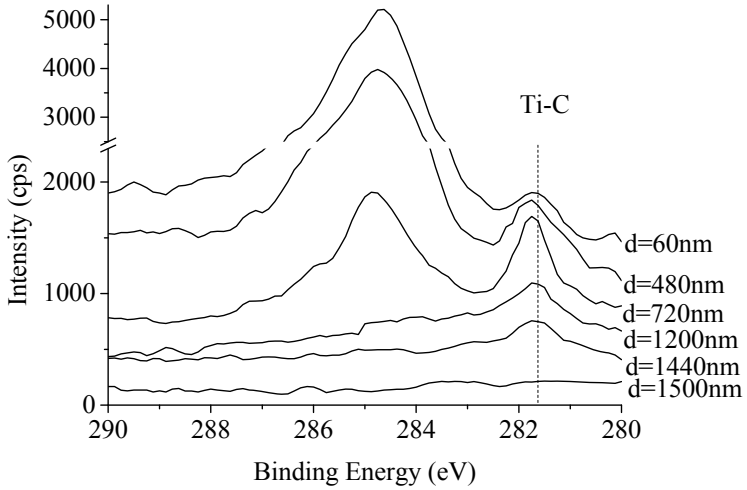

(c)

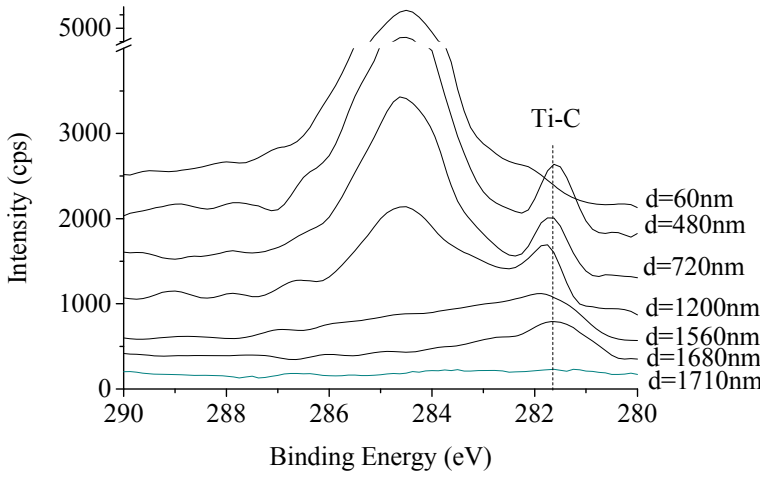

(d)

Fig. 4.3 High resolution of C1s XPS spectra obtained from the Ti side of the joined samples: (a) Sample 1, (b) Sample 2, (c) Sample 3, (d) Sample 4.

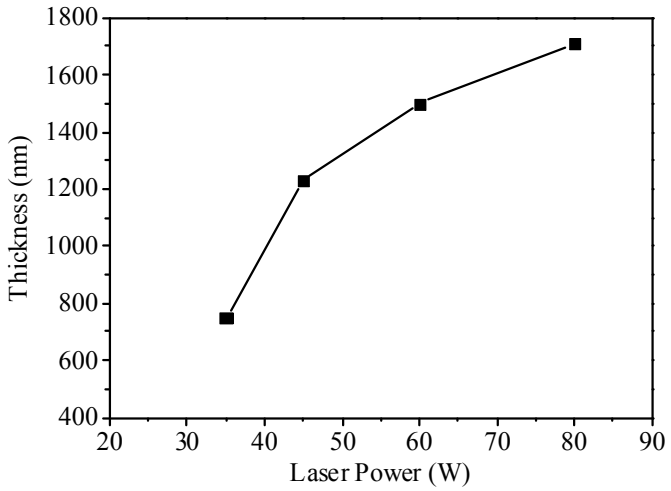

Fig. 4.4 The relationship between the laser power input and the thickness of the interface containing the chemical bond of Ti-C.

4.3.2 Ti2p XPS spectra

Fig. 4.5 shows the high-resolution Ti2p XPS spectra of the four samples at various sputtering depths (measuring from d=0). New chemical bonds (Ti–C, Ti–O and Ti_2O_3) were found in the joining process. At d=0, only the TiO_2 peak with a Ti2p3/2 binding energy of 459.3 eV was present; this phase is believed to be the naturally formed oxide at the Ti surface. After further ion milling to a depth 60 nm, a broad binding energy peak (453.7–456.5 eV) was obtained, which can be attributed to the formation of new Ti–C, Ti–O and Ti_2O_3 bonds. The peaks at 454.8 eV, 455.1 eV, and 456.8 eV were most likely due to the Ti–C bond [2], the Ti–O bond [2] and the formation of Ti_2O_3 [118], respectively.

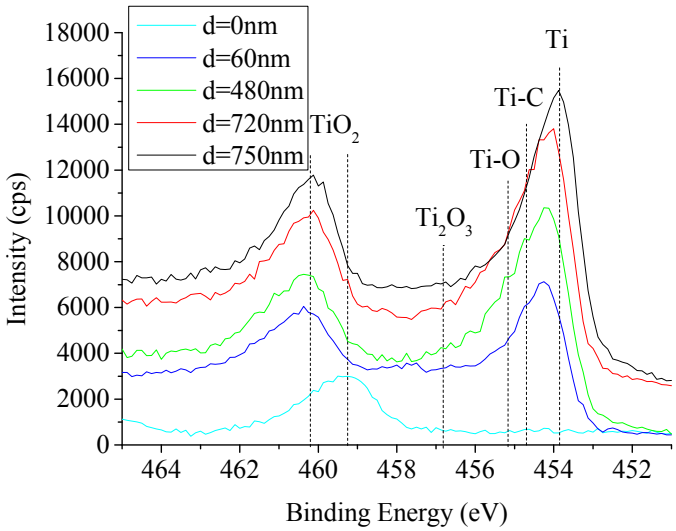
d=0nm
d=60nm
d=480nm
d=720nm
d=750nm
Ti
Ti-C
Ti-O
TiO2
Ti2O3
Intensity (cps)
Binding Energy (eV)

(a)

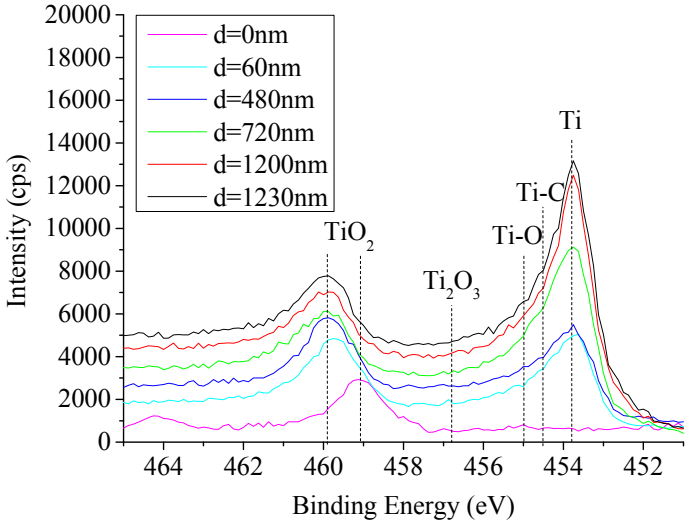
d=0nm
d=60nm
d=480nm
d=720nm
d=1200nm
d=1230nm
Ti
Ti-C
Ti-O
TiO2
Ti2O3
Intensity (cps)
Binding Energy (eV)

(b)

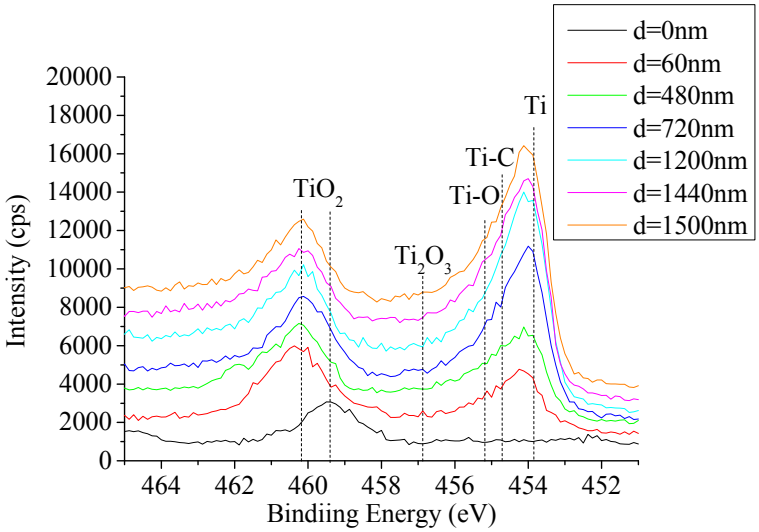
d=0nm
d=60nm
d=480nm
d=720nm
d=1200nm
d=1440nm
d=1500nm
Ti
Ti-C
Ti-O
TiO2
Ti2O3
Intensity (cps)
Bindiing Energy (eV)

(c)

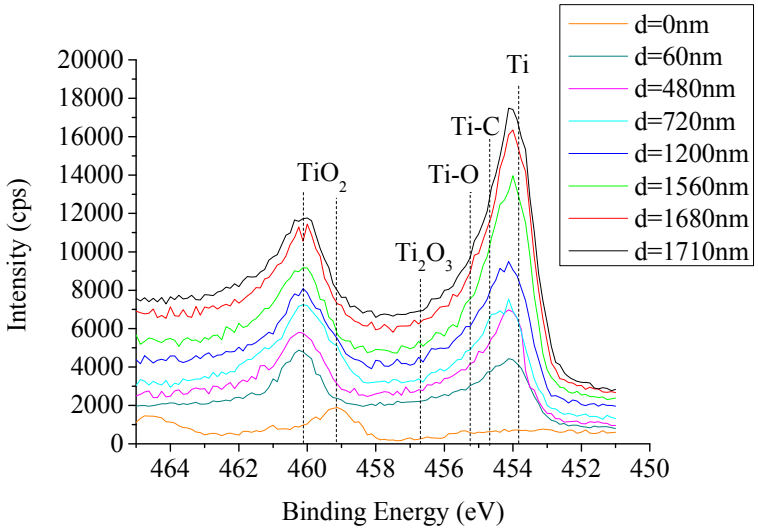

(d)

Fig. 4.5 High resolution of Ti2p XPS spectra taken from the Ti side of the joined samples after ion milling to the indicated depths: (a) Sample 1; (b) Sample 2; (c) Sample 3; (d) Sample 4.

4.3.3 Comparison of bond intensity

The Ti2p XPS curve-fitted spectra of the four samples measured at the Ti side, at various ion-milling depths, are given in Appendix A. A comparison of these spectra reveals that the chemical bonds in the four samples are identical. In other words, apart from Ti–O, Ti–C and Ti_2O_3, increasing the laser energy did not create any new chemical bonds. The area under each peak represents the bond intensity. The relative amounts of Ti–O, Ti–C, and Ti_2O_3 in the four samples at various sputtering depths are summarised in Table 4.1. The data show that the intensities of both the Ti–O and Ti–C bonds generated during the joining process increased noticeably with increasing laser power. Moreover, as the laser input energy increased, the thickness of the interface containing the Ti–O and Ti–C bonds also increased, as shown in Figure 4.4 and Table 4.1. On the other hand, the energy input effect on the intensity of Ti_2O_3 was relatively weak. This suggests that increasing the laser energy input mainly promotes the

generation of Ti–O and Ti–C bonds to a greater depth at the joint interface. It is reasonable because increased laser power raises the joint zone temperature and extends the heating time for chemical reaction. This promotes chemical reaction between titanium atoms and phenyl carbons and –C=O of PET chains.

Table 4.1 A comparison of the chemical bonds counts for different sputtering depths

Sample	Sputtering depth (nm)	Chemical bonds									
		Ti-C		Ti-O		Ti_2O_3		TiO_2		Ti	
		B.E. position	Peak area	B.E. position	Peak area	B.E. position	Peak area	B.E. position	Peak area	B.E. position	Peak area
Sample 1	60	454,8	3541	455.1	4744	456.78	2539	460.37	8241	453.96	8399
	480	454.78	2489	455.13	5755	456.8	1019	460.35	8681	453.93	10168
	720	454.82	2698	455.12	5052	456.83	587	460.29	10499	453.92	12756
	750	-	-	-	-	-	-	460.25	12335	454.02	22180
Sample 2	60	454.78	1861	455.1	770	456.8	221	459.73	6507	453.8	5191
	480	454.8	609	455.08	1971	456.78	1098	460.32	7160	453.79	6042
	720	454.82	1158	455.12	2767	456.79	819	460.25	7529	453.85	12039
	1200	454.83	2235	455.16	1535	456.83	860	460.03	6863	453.83	14743
	1230	454.79	630	455.2	648	-	-	459.94	6122	453.87	17860

Sample 3	60	454.8	332	455.1	2113	456.8	694	460.27	10771	453.96	3975
	480	454.8	1589	455.13	3086	456.83	1335	460.33	10582	453.98	7141
	720	454.8	2703	455.1	6110	456.87	2391	460.21	11398	453.96	9441
	1200	454.79	2358	455.1	5439	456.86	1712	460.2	9634	453.98	13424
	1440	454.8	2473	455.12	4265	456.82	102	460.19	8871	453.96	13725
	1500	454.83	814	455.09	872	456.78	0	460.04	8303	453.95	14316
Sample 4	60	455.8	1241	455.12	2278	456.8	1435	460.23	6080	453.94	3987
	480	454.83	1644	455.1	3601	456.84	1435	460.23	8697	454.04	5752
	720	454.8	3219	455.1	3876	456.83	500	460.17	11801	453.91	8419
	1200	454.8	4065	455.16	3657	456.78	943	460.03	10327	453.94	10537
	1560	454.79	2564	455.1	3129	456.83	1028	460.1	9267	453.92	14974
	1680	454.85	1302	455.08	2031	456.87	0	460.19	8355	453.86	17723
	1710	454.83	511	455.13	610	456.81	0	460.16	11280	453.93	19671

4.4 Tensile shear force

Typical tensile load-displacement curves of the four samples are shown in Fig. 4.6, with the average failure load presented in Fig. 4.7. Despite the fact that the amount of porosity in the joint increased as the laser power was increased, the failure load increased from 310 N to 823 N when the laser power increased from 35 W to 60 W. The failure load encountered a decrease when the laser power was raised to 80 W. This indicates that although the chemical bonding intensity at the interface was increased as the laser energy was increased, and this should enhance the joint strength, the amount of porosity in the joint also increased. The results thus show that when the amount of bubbles reaches a certain value, the bubble weakening effect would outweigh the strengthening effect obtained from a higher chemical bonding intensity.

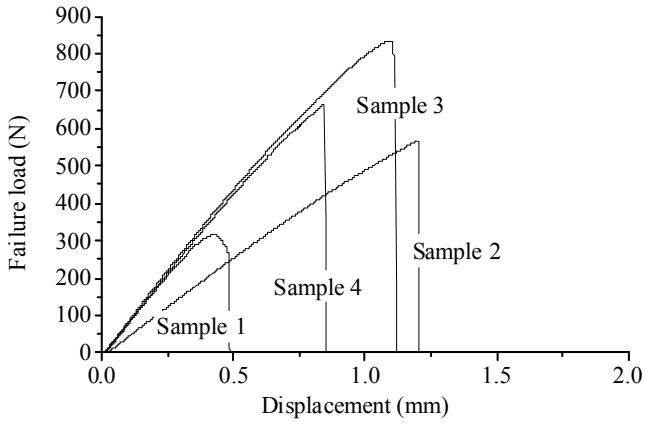

Fig. 4.6 Typical load-displacement curves of the LAMP samples.

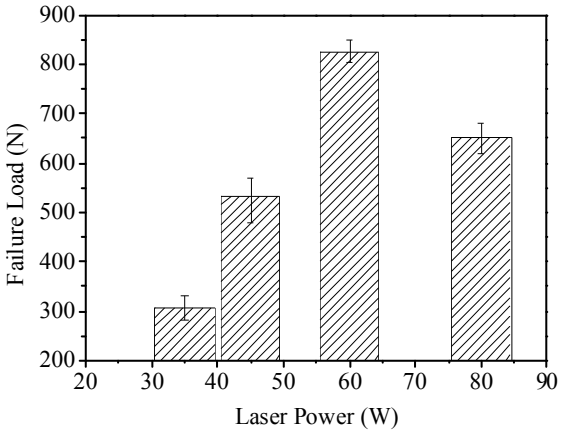

Fig. 4.7 Tensile failure load as a function of laser power.

4.5 Chapter summary

(i) Laser energy has a considerable effect on the formation of bubbles in the joint. A somewhat discrete distribution of bubbles was obtained when a relatively low laser energy was used, which in this study was 45 W. When the energy was raised to 60 W, large connected bubbles were formed along the centreline of the joint. Further increase of the energy to 80 W, produced more bubbles, although they became more dispersed and occupied a larger area of the weld.

(ii) The results of the XPS analysis demonstrated that the Ti-PET interface contained Ti–C, Ti–O and Ti_2O_3 bonds after laser irradiation, and the thickness of the interface, in general, increased with increasing laser energy input. Increasing the laser energy input also increased the intensity count of the chemical bonds.

(iii) Both the characteristics of the bubbles and the chemical bond intensities of the Ti–C and Ti–O species have pronounced effects on

the tensile failure load of the joints. When the amount of bubbles was high, the weakening effect of the bubbles outweighed the strengthening effect of the high chemical bonding intensity.

Chapter 5

U-LAMP Joining Titanium to PET Using a Low Laser Power

5.1 Introduction

In this chapter, a comparison of the joint appearance, chemical bonds at the interface, and failure load of the specimens produced by LAMP and U-LAMP at a low laser power is made. Based on the results of the study of the LAMP process in Chapter 4，the laser power used in the study described in this chapter was kept at 30 W to avoid decomposition of the polymer and the formation of laser-induced bubbles. In this case, the effects of ultrasonic vibration on joint performance can be studied, without the complication of the bubble effect. In this study, the only variable is the vibration amplitude, ranging from 0 to 6 μm.

5.2 Joint performance

Fig. 5.1 shows the joint appearance as a function of vibration amplitude. For all specimens which were processed using a laser power of 30 W, virtually no porosity was observed in the joint under an optical microscope at a magnification of 1000, except for two specimens (one LAMP and one U-LAMP) in which a few cases (less than four) of small porosity < 80 μm were found (Fig. 5.2). It is believed that these small bubbles may have come from trapped air at the metal-plastic interface. This result thus shows that a laser power of 30 W will melt the plastic but not cause decomposition of the polymer or forming gas

products due to pyrolysis reactions. If a laser power higher than 45 W is used, bubbles will develop in the joint as shown in Fig. 4.1. The development of bubbles is due to excessive laser power which causes decomposition of the polymer and the formation of some gas products [119].

Without ultrasonic Vibration (Specimen A1)	With vibration Amplitude = 2 μm (Specimen B)	With vibration Amplitude = 4 μm (Specimen C)	With vibration Amplitude = 6 μm (Specimen D)

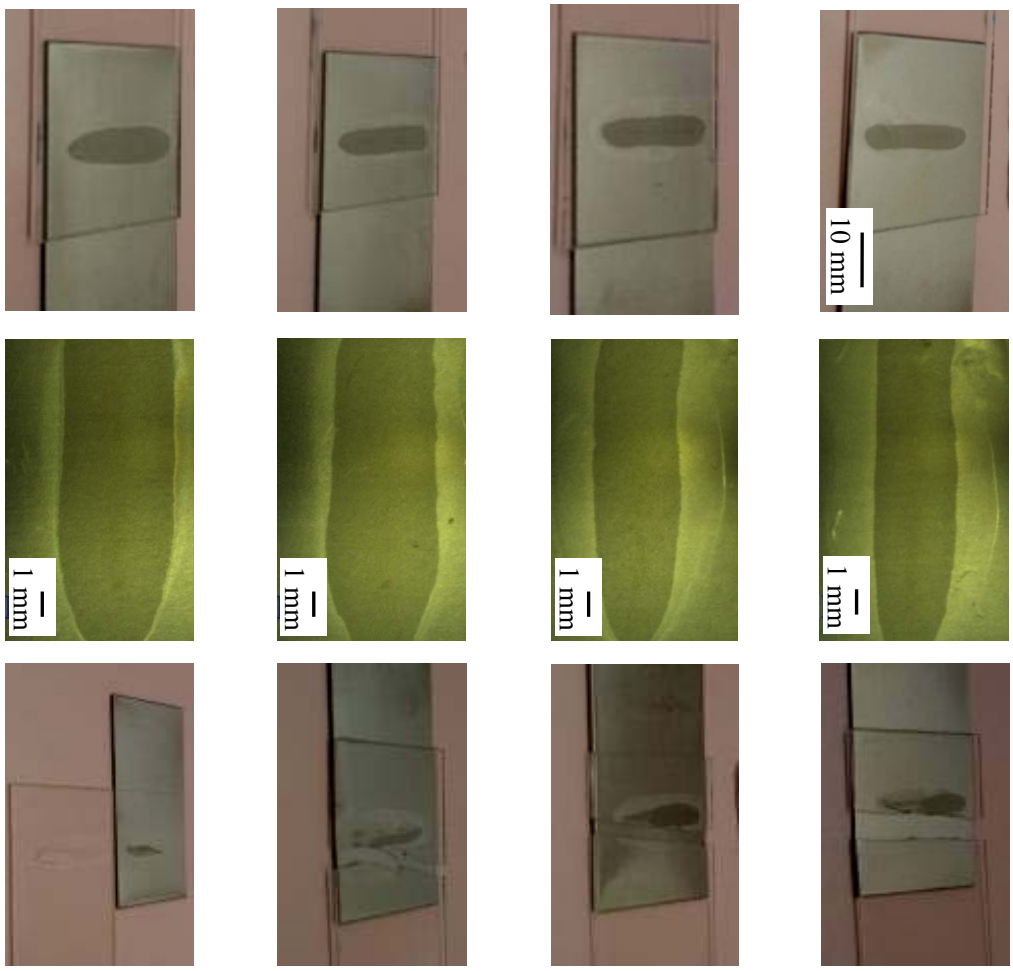

Fig. 5.1 Typical joints formed by the LAMP and U-LAMP processes with the fractured specimens shown at the bottom row.
(All specimens processed at laser power of 30 W; refer to Table 3.9 for designation of specimens)

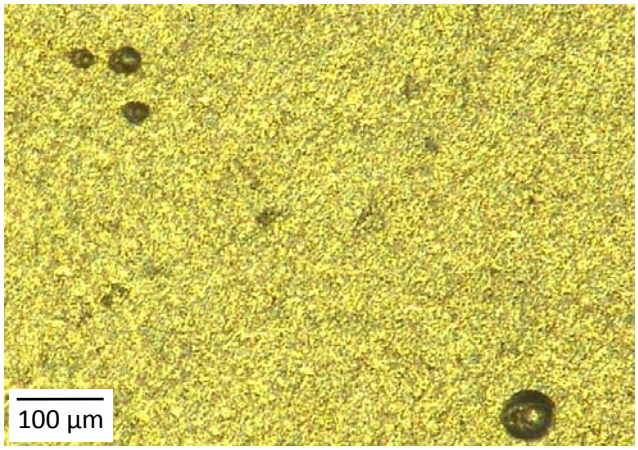

(a)

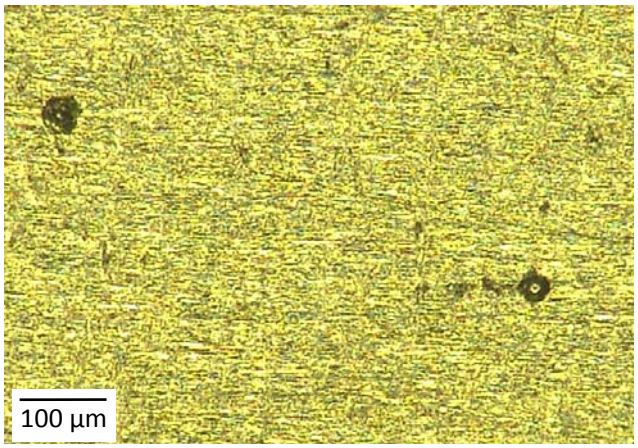

(b)

Fig. 5.2 Only very few relatively small bubbles appear in the joints produced using a laser power of 30 W: (a) a LAMP specimen, (b) a U-LAMP specimen.

5.3 Chemical bonds

5.3.1 C1s XPS spectra

XPS analysis was performed in the centre of the joint. Typical high-resolution XPS spectra of the C1s lines of the U-LAMP specimen without ion-milling are shown in Fig. 5.3. The spectra are similar to the LAMP

specimens (Fig. 4.2), with all the peaks originated from the PET chains [2, 117]. This means that the Ti surface of both the LAMP and U-LAMP specimens were covered with some residue of PET after mechanical separation. This suggests that the metal and plastic parts in the central area were not simply bonded together by mechanical keying.

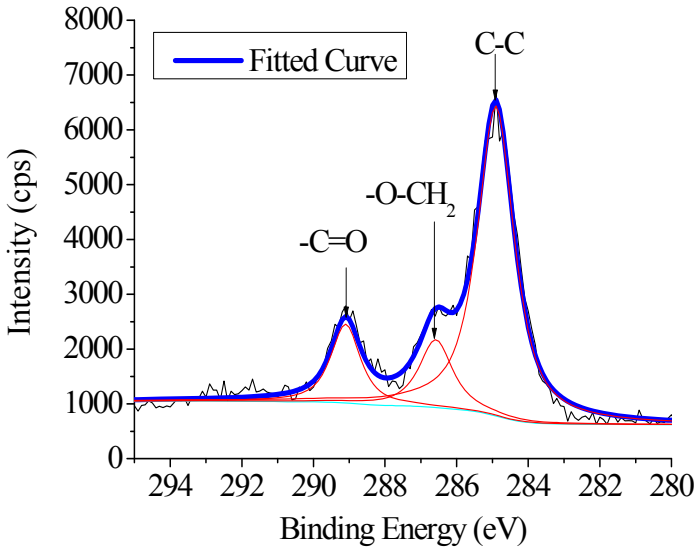

Fig. 5.3 Curve fitting conducted for C1s high resolution XPS spectra taken from the Ti side of the PET/Ti specimen produced by U-LAMP (Specimen C).

To investigate the nature of the bonding across the joint interface, XPS was performed by further ion-milling to different depths from the Ti surface (i.e. d=0) for both the LAMP and U-LAMP specimens. At a milling depth of 60 nm, the carbonyl group (at 289.2 eV) entirely disappeared for both LAMP and U-LAMP specimens (Fig. 5.4). On the other hand, the C1s line of Ti-C (at approximately 281.7 eV) was observed for all specimens. Such a peak was reported by Georgiev [56] and Wang [2]. Fig. 5.4 also shows that the areas of

the C-C peak and Ti-C peak both decreased as the ion-milling depth increased. For the LAMP specimen, the peaks at 284.8 eV and 281.7 eV disappeared when milling depth reached 660 nm. This suggests that the thickness of the interface containing the new chemical bond of Ti-C was about 600 nm. However, for all U-LAMP specimens, the Ti-C peak can still be clearly seen at a depth of 600 nm. The data shown in Fig. 5.4 suggest that the thickness of the interface containing the new Ti–C chemical bond is ~1230 nm in Sample B (amplitude = 2 μm), ~1710 nm in Sample C (amplitude = 4 μm), and ~1980 nm in Sample D(amplitude = 6 μm). These indicate that the thickness of the interface containing the new chemical bond of Ti-C was at least two times thicker than that of the LAMP joint. This result suggests that more titanium atoms reacted with the phenyl carbons of the PET chain in U-LAMP than in LAMP, and this activity becomes more pronounced as the vibration amplitude is increased. Fig. 5.5 shows the relationship between vibration amplitude and the estimated Ti-C boned interface thickness.

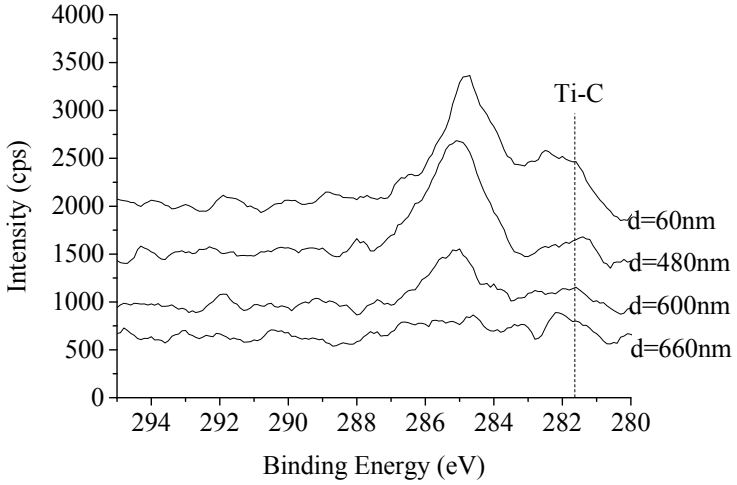
Intensity (cps)
Binding Energy (eV)
Ti-C
d=60nm
d=480nm
d=600nm
d=660nm

(a)

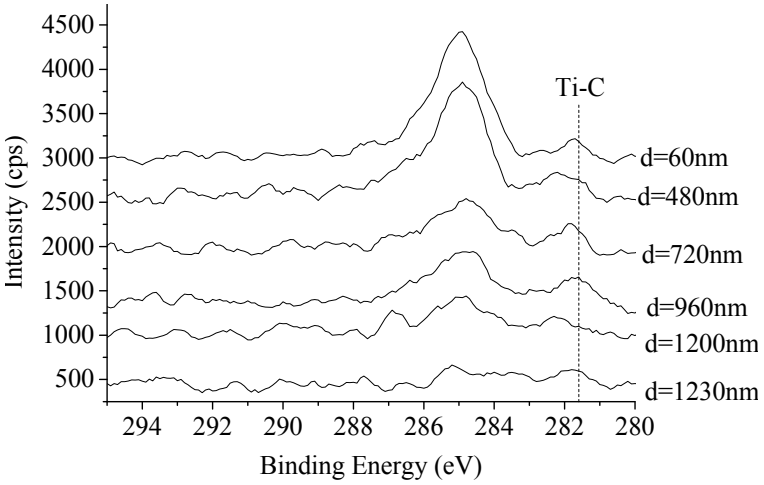
Intensity (cps)
Binding Energy (eV)
Ti-C
d=60nm
d=480nm
d=720nm
d=960nm
d=1200nm
d=1230nm

(b)

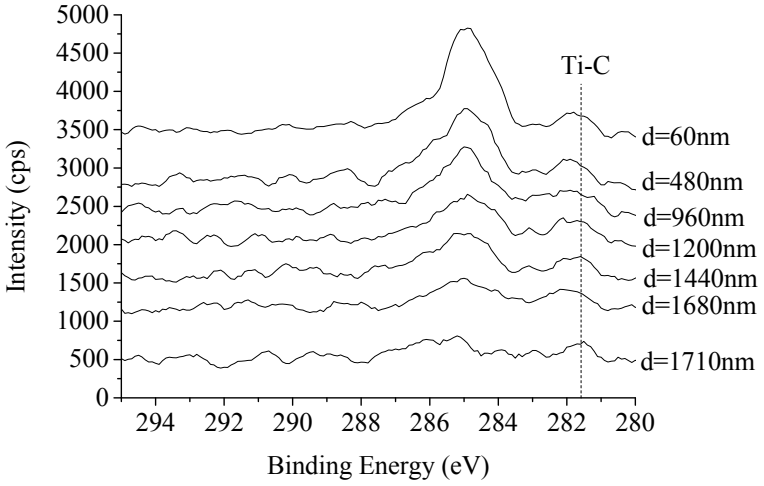
Intensity (cps)
Binding Energy (eV)
Ti-C
d=60nm
d=480nm
d=960nm
d=1200nm
d=1440nm
d=1680nm
d=1710nm

(c)

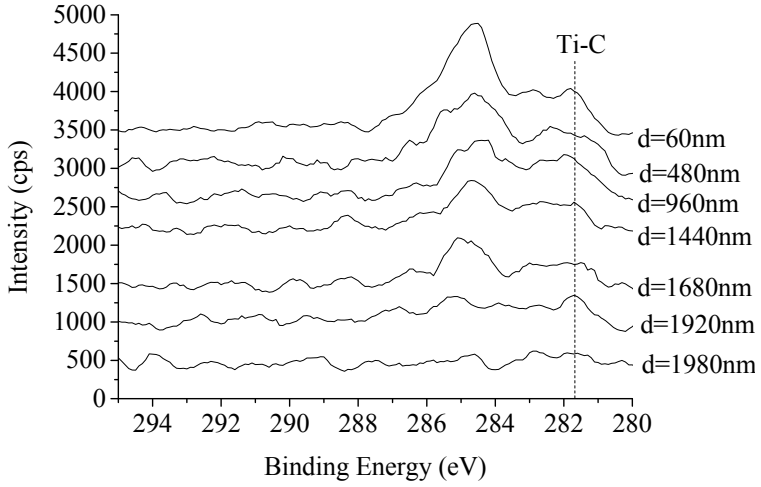

(d)

Fig. 5.4 High resolution C1s XPS spectra taken from the Ti side at different ion-milling depths of LAMP and U-LAMP specimens: (a) LAMP specimen; (b) U-LAMP specimen with amplitude = 2 μm; (c) U-LAMP specimen with amplitude = 4 μm; (d) U-LAMP specimen with amplitude = 6 μm.

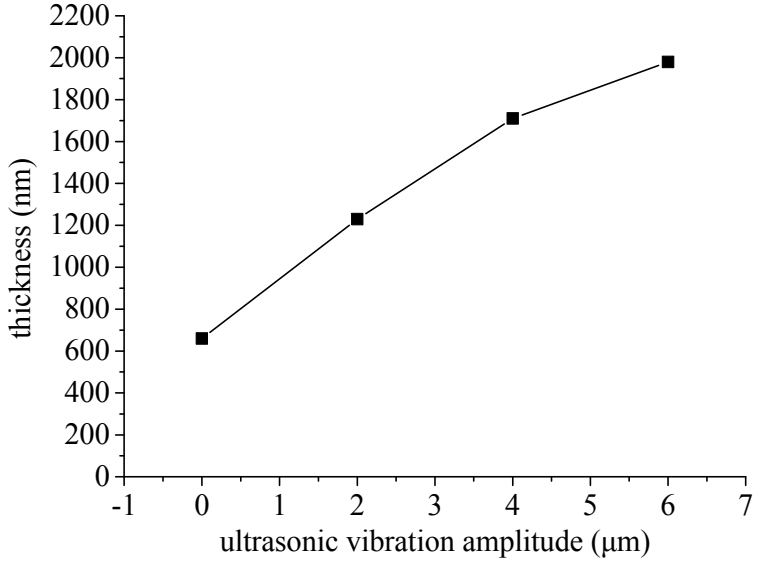

Fig. 5.5 The relationship between vibration amplitude and thickness of the interface containing the chemical bond of Ti-C.

5.3.2 Ti2p XPS spectra

In addition to the high resolution of the C1s XPS spectra, the results of high-resolution XPS spectra of the Ti2p lines were also obtained for the LAMP and U-LAMP specimens at various sputtering depths (measuring from d=0) (Fig. 5.6). Both the LAMP and U-LAMP joints have similar chemical bonds consists of Ti-C, Ti-O, TiO_2, Ti_2O_3. The XPS binding energy peak values of these bonding species were obtained from [2, 56, 57, 118].

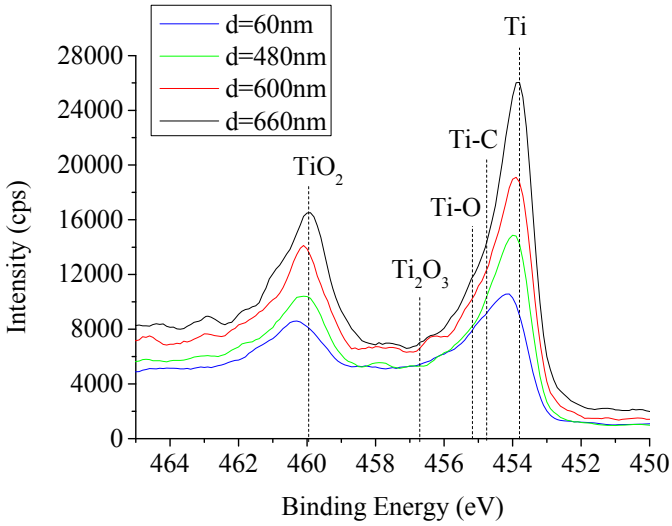

(a)

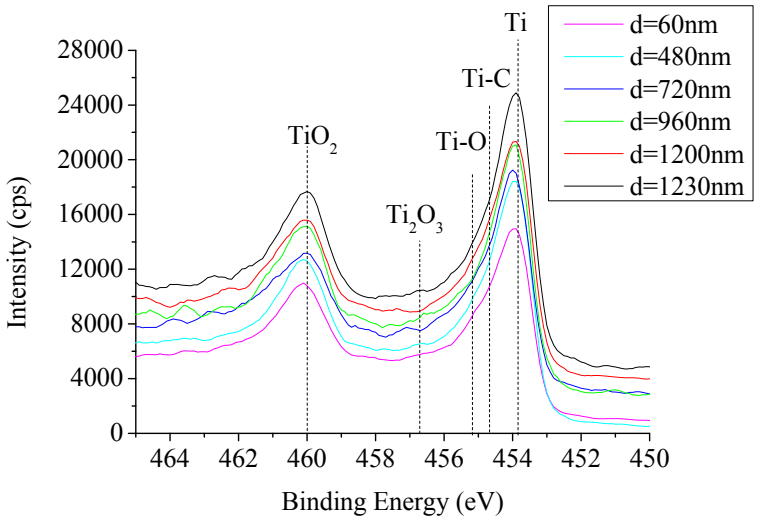

(b)

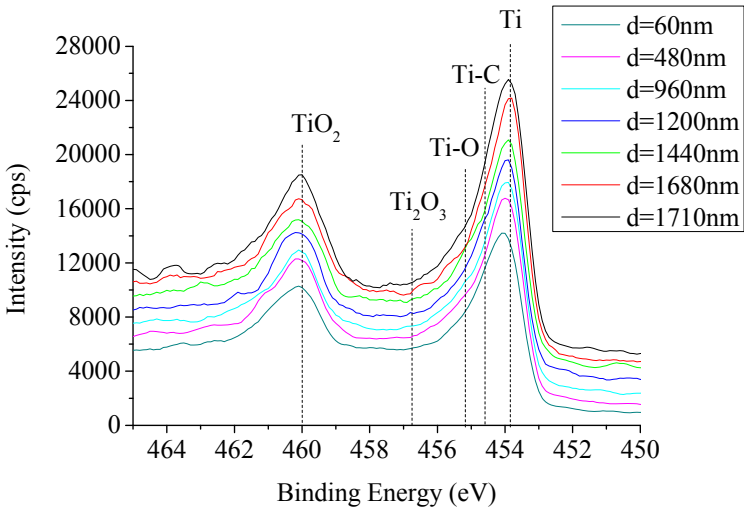

(c)

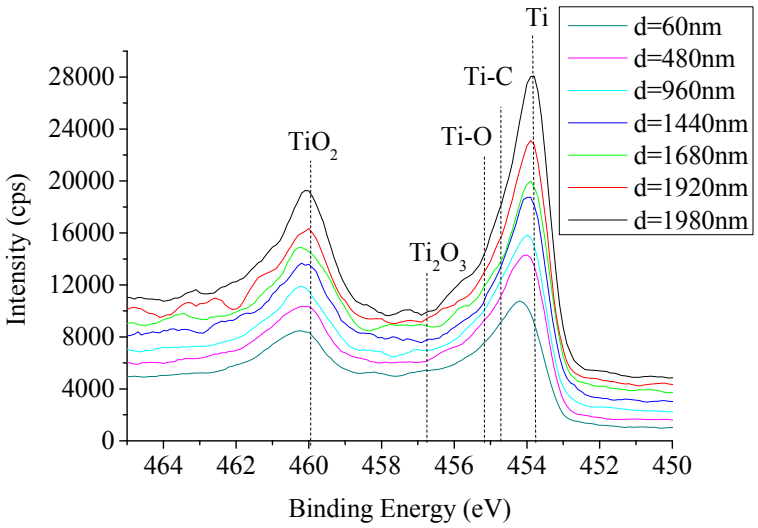

(d)

Fig. 5.6 High resolution Ti2p XPS spectra taken from the Ti side at different ion-milling depths of LAMP and U-LAMP specimens: (a) LAMP specimen; (b) ULAMP specimen with amplitude = 2 μm; (c) U-LAMP specimen with amplitude = 4 μm; (d) U-LAMP specimen with amplitude = 6 μm.

5.3.3 Comparison of chemical bond intensity

The Ti2p XPS curve-fitted spectra of the joint interfaces of the LAMP and U-LAMP specimens were obtained from the Ti side, at various ion-milling

depths. The XPS spectra obtained for the LAMP and U-LAMP specimens are given in Appendixes A and B. A comparison of these spectra reveals that the nature of the chemical bonds of all samples is similar; the bonds found at the interface were: Ti–O, Ti–C and Ti_2O_3, and increasing the ultrasonic vibration amplitude did not create any new chemical bonds. The relative amounts of Ti–O, Ti–C, and Ti_2O_3 for the LAMP and U-LAMP specimens at various sputtering depths are summarised in Table 5.1. The intensities of the Ti–O, Ti–C and Ti_2O_3 bonds generated during joining increased noticeably with increasing vibration amplitude. The thickness of the interface containing these three chemical bonds also increased, as shown in Figure 5.5 and Table 5.1. It is concluded that an increasing of vibration amplitude promotes the formation of Ti–O, Ti–C and Ti_2O_3 bonds. The main reason why a thicker bond interface and large amounts of chemical bonds were obtained for the U-LAMP specimens is believed to be due to a more intimate contact between Ti and the molten polymer being obtained because ultrasound exerts an extra pressure with an oscillation effect on the molten polymer. This can facilitate chemical reactions at the interface. On the other hand, ultrasonic vibration generates extra energy and this could raise the temperature of the joint zone as well as prolonging the heating time for the chemical reactions between the titanium atoms and phenyl carbons, and the oxygen double bonded carbon in the carbonyl groups -C=O of the PET chain. Thermal analyses of the LAMP and U-LAMP processes and the changes of joint zone temperature as a result of ultrasonic vibration are presented in the following chapter.

Table 5.1 A comparison of the chemical bonds counts for different sputtering depths

Sample	Sputtering depth (*nm*)	Chemical bonds									
		Ti-C		Ti-O		Ti_2O_3		TiO_2		Ti	
		B.E. position	Peak area	B.E. position	Peak area	B.E. position	Peak area	B.E. position	Peak area	B.E. position	Peak area
LAMP(30 W)	60	454.8	5296	455.1	4349	456.8	3909	460.2	9998	454.0	8272
	480	454.8	4496	455.1	7444	456.8	5761	460.2	16982	453.9	15635
	600	454.8	3764	455.1	3438	-	-	460.1	11331	453.9	19902
	660	454.8	818	455.1	937	-	-	460	13583	453.9	33409
U-LAMP (amplitude=2 μm)	60	454.8	2612	455.1	4112	456.8	784	460.1	8090	453.9	14968
	480	454.8	2749	455.1	10178	456.8	6468	460.1	18161	453.9	21794
	720	454.8	3029	455.1	8397	456.8	5836	460.1	10401	453.9	19526
	960	454.8	4607	455.1	7676	456.8	2645	460.1	16709	453.9	21054
	1200	454.8	1910	455.2	6047	456.8	1260	460.1	16210	453.9	19745
	1230	454.8	300	455.1	519	-	-	460	15157	453.9	25187

U-LAMP (amplitude=4 μm)	60	454.8	4663	455.1	5024	456.8	3492	460.2	12409	453.9	12449
	480	454.8	4911	455.1	11012	456.8	7161	460.2	19955	453.9	14384
	960	454.8	5306	455.1	9983	456.8	5671	460.2	17066	453.9	15138
	1200	454.8	4563	455.1	7180	456.8	3875	460.1	11933	453.9	15576
	1440	454.8	3246	455.1	7016	456.8	2396	460.1	15335	453.9	17006
	1680	454.8	2578	455.1	6418	456.8	557	460.1	14371	453.9	20525
	1710	-	-	455.1	566	-	-	460.1	12888	453.9	12888
U-LAMP (amplitude=6 μm)	60	454.8	2903	455.2	4739	456.9	4021	460.3	11004	453.9	10356
	480	454.8	6166	455.1	4309	456.8	3538	460.2	12702	453.9	13395
	960	454.8	3366	455.1	4466	456.8	2285	460.2	14149	453.9	15830
	1440	454.8	1704	455.1	4980	456.8	2489	460.1	13785	453.9	19379
	1680	454.8	6629	455.1	6730	456.8	2674	460.1	18887	453.9	18067
	1920	454.8	5082	455.1	6060	456.8	1887	460.1	16240	453.9	21251
	1980	454.8	696	455.2	918	-	-	460.1	18951	453.9	32579

5.4 Tensile shear strength

Figs. 5.7 and 5.8 show the results of the tensile shear tests of the joints formed with and without ultrasonic vibration. The various test specimens' designations are given in Table 3.8. The results clearly illustrate that the failure load increases significantly when ultrasonic vibration is applied (Fig. 5.7). Moreover, within the range of this study, the improvement can be as high as fourfold (comparing Specimen A1 and Specimen B). It was interesting to find that high vibration amplitudes greater than 2 μm yield a low failure loads. One possible reason for this is because high vibration amplitudes can induce mechanical activation of the covalent bonds and result in some degree of degradation of the polymer. The difference in failure load between the joints formed with and without ultrasonic vibration becomes apparent when their failure modes are considered. The one without vibration failed at the interface between the metal and plastic parts; while for the specimens with ultrasonic aid, failure always occurred in the plastic part (Fig. 5.1). To make a comparison on the joint strength of the specimens produced by the conventional LAMP (i.e. a relatively high laser power is used to cause some decomposition of the polymer in use), some joints were prepared using a laser power of 45 W and without ultrasonic vibration. Fig. 5.7 shows that the joint formed using a laser power of 45 W (Fig. 4.1) which contained bubbles, has an average failure load of 563 N (Specimen A2). Although the load is double that of Specimen (A1) (272 N) (which has no bubbles and was produced without ultrasonic vibration), when compared to the joints formed with ultrasonic vibration and containing no bubbles, the latter's failure stress (Specimen B) was double that of Specimen A2.

The ductility of the U-LAMP specimens was also much higher than that of the LAMP specimens (Fig. 5.8). These results clearly demonstrate the superiority of the new U-LAMP method over the conventional LAMP method. The main reason for this is believed to be due to the absence of bubbles in the joint as a result of the low laser power used. In addition, the stronger interface formed between the Ti and PET due to ultrasonic vibration is also a key element that contributes to the improvement of joint strength.

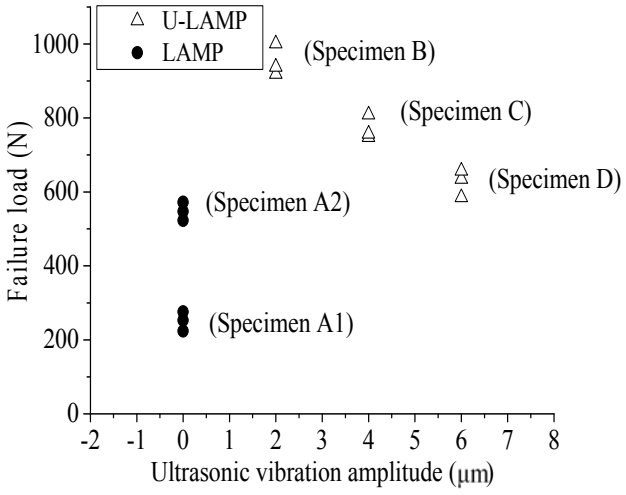

Fig. 5.7 A comparison of fracture stress for the LAMP and U-LAMP specimens.

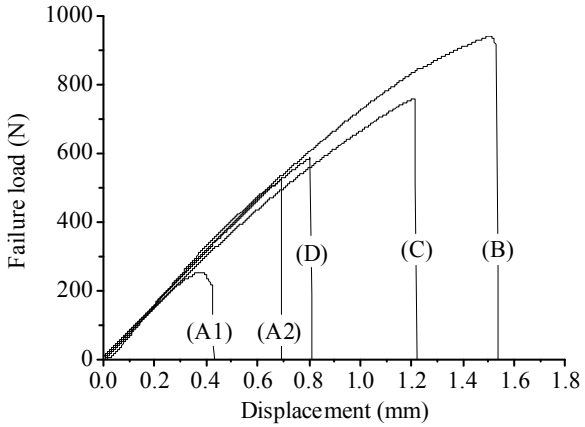

Fig. 5.8 Typical load-displacement curves obtained for the LAMP and U-LAMP specimens.

5.5 Chapter summary

(i) For specimens joined at 30 W (no bubbles were observed), the strength of the joint produced using ultrasonic aiding, in terms of tensile failure load, was always higher than that of the joint formed without any ultrasound aid. This improvement can be as high as three times. When compared to the joint produced using a higher laser power (45 W) and without any ultrasonic aid, and where bubbles had formed, the joint strength of the ultrasonic-aid specimen (laser power 30 W) was nearly doubles the former.

(ii) Ultrasonic vibration promotes chemical reaction between molten PET and Ti metal. The XPS results showed that the U-LAMP specimens have higher bond intensities of Ti-C, at the joint interface, than the LAMP specimens. This is considered to be primarily due to a more intimate contact being obtained between molten PET and Ti metal under the action of vibration.

Chapter 6

Temperature field simulation of the molten pool

For both LAMP and U-LAMP joining, the formation of bubbles in the joint depends greatly on the temperature of the molten polymer pool, which also affects the size of the bonding area. The XPS results presented in Section 5.2 show that the application of ultrasonic vibration did facilitate chemical reactions at the joint interface. This could, to a degree, be due to the vibration energy causing the temperature of the molten polymer to increase, thus promoting the chemical reaction. To determine the degree of the effect, this chapter presents analyses of the thermal fields of the joints in the LAMP and U-LAMP processes.

6.1 Description of the thermal field model

Laser rapid heating followed by rapid cooling, is a typical thermal cycle in the analysis of a nonlinear transition heat conduction process. When the laser heat source moves, the temperature of the joint changes significantly as a function of time and space, and this can result in a drastic change of the thermophysical properties of the material. The governing equation of a nonlinear transient heat conduction event based on the law of conservation of energy and the Fourier thermal conductivity law can be expressed as [120],

$$\rho c(T)\frac{\partial T}{\partial t} = k(T)\left(\frac{\partial^2 T}{\partial x^2} + \frac{\partial^2 T}{\partial y^2} + \frac{\partial^2 T}{\partial z^2}\right) + Q(x, y, z, t) \tag{6.1}$$

where *(x, y, z)* represents the coordinate system of the moving heat source, *T* is

the temperature (K) of the field of the study, t is the time (s), ρ is the density of the working material (kg/m^3), c is the material's specific heat capacity (J/(kg·K)), k is the material's thermal conductivity (W/(m·K)), and Q is the power of the heat source/unit volume (W/m^3).

6.1.1 Material properties

During the temperature field simulation, the thermo-physical properties of the joining material change with temperature, however, very limited thermal-physical data as a function of temperature are available for PET. For simplicity, the phase change of PET in this study is not considered and the thermal and physical properties of PET are assumed to be constant. The properties of Ti and PET used in the model are given in Tables 3.5 and 3.6, respectively. The absorption of laser light at the surface of the Ti sheet is an important factor in calculating the temperature field during laser joining. The absorption coefficient (η) at the Ti sheet surface can be determined using [121]:

$$\eta = 0.365\left\{\rho_R\left[1+\beta\left(T-20\right)/\lambda_{laser}\right]\right\}^{1/2} \tag{6.2}$$

where ρ_R is the resistivity of Ti sheet at 25 ℃, β is the temperature coefficient of resistance, T is the temperature, and λ_{laser} is the wavelength of the laser beam.

6.1.2 The heat source

During LAMP joining, the laser light will pass through the PET sheet which is placed on top of the Ti sheet. When the laser beam strikes the surface of the bottom Ti sheet, a temperature field is generated at the laser-metal interacting spot. Some of the heat energy generated at the Ti surface is conducted back to the top PET sheet through the metal-plastic interface. Based

on the work of Wu [122], the total heat energy generated at the material can be determined and is equal to the effective power of the laser beam, thus:

$$q_m = \frac{3\eta P_{laser}}{\pi {R_{laser}}^2} \tag{6.3}$$

where q_m is the highest heat-flow density in the centre of the laser, η is the absorption coefficient of the material, P_{laser} is the power of the laser, and R_{laser} is the laser spot size.

A number of heat source models have been put forward, such as the half ball model, the ellipsoid model, the Gaussian model and the Rosonthal model. As the thickness of the PET and Ti sheets are only 1mm, the temperature variation in the thickness direction can be ignored. Therefore, in this study, the surface heat source adopts the Gaussian model, which has the heat flux characteristics as shown in Fig. 6.1, and can be represented by the Gaussian function [123]:

$$q(r) = \begin{cases} q_m \exp(-3{r_{laser}}^2 / {R_{laser}}^2), & r_{laser} \le {R_{laser}}^2 \\ 0, & r_{laser} > {R_{laser}}^2 \end{cases} \tag{6.4}$$

where $q(r)$ is heat-flow density, r_{laser} is the distance from the centre of the heat source, q_m is the maximum heat flux in the laser centre, and R_{laser} is the radius of the laser spot.

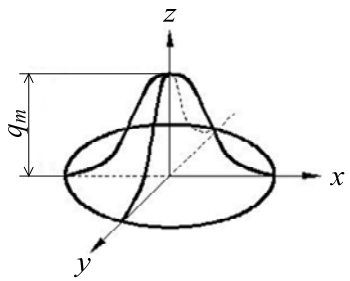

Fig. 6.1 The Gaussian model of the heat flux.

6.1.3 Moving of the heat source

The thermal field analysis uses ANSYS software that considers a moving Gaussian heat source along the joint seam (y-axis):

$$q(x,y,t)=\begin{cases} q(x,y,t)=\dfrac{3\eta P_{laser}}{\pi {R_{laser}}^2}\exp\{-\dfrac{3}{{R_{laser}}^2}[x^2+(y-v(t-\tau))^2]\}, & r_{laser}\le {R_{laser}}^2 \\ 0, & r_{laser}>{R_{laser}}^2 \end{cases} \tag{6.5}$$

where η is light absorption coefficient of the material, P_{laser} is the power of the laser, R_{laser} is the radius of laser spot, t is joining time, v is the moving speed of the heat source, and r_{laser} is the distance from any point of the material to the centre of the light spot.

The APDL programming language of ANSYS is applied to describe the moving Gaussian laser heat source. A node in the joint is identified as the centre of the Gaussian laser heat source; the load is defined using the APDL programming language after all the nodes have been determined around the laser source centre. With the moving laser heat source, the node is redefined with its load updated continuously. The loop statement of *DO—*ENDDO is applied to redefine the load.

6.1.4 Initial and boundary conditions

The geometry and the properties of the materials, the initial condition and the boundary condition of the joint are all required for conducting the simulation. The initial condition of the nonlinear heating event is the temperature field of the initial status. The boundary condition is the temperature and the thermal conduction condition of the target boundary.

In this analysis, the initial condition is:

$$T(x,y,z) = T_0(x,y,z), \quad (x,y,z) \in D \tag{6.6}$$

where T_0 (K) is ambient temperature, T (K) is the surface temperature of the material.

The boundary condition can be defined as

$$k\frac{\partial T}{\partial n} - q + h(T - T_0) + \sigma\varepsilon(T^4 - T_0^4) = 0, \quad (x,y,z) \in S, t > 0 \tag{6.7}$$

where k is thermal conductivity, h is heat transfer coefficient for convection (W/(m^2·K)), σ is Stefan-Boltzmann constant for radiation, and ε is the emissivity.

6.2 Simulation results

The temperature field of the joint was simulated for different laser processing powers with a laser travel speed of 4 mm/s and pulsed duration 8 ms. The results showed that after a processing time of 2 s, the temperature field reached a quasi-steady state. Fig. 6.2 shows the temperature field at the interface between the PET and Ti sheets as a function of time under the joining condition

of a laser processing power of 55 W. A greater temperature gradient was found in front of the moving laser spot. The join temperature increases gradually as the joining process proceeds from 0.5 s to 2 s. After 2 s, the thermal profile reaches a quasi-steady state on which the temperature rises slowly.

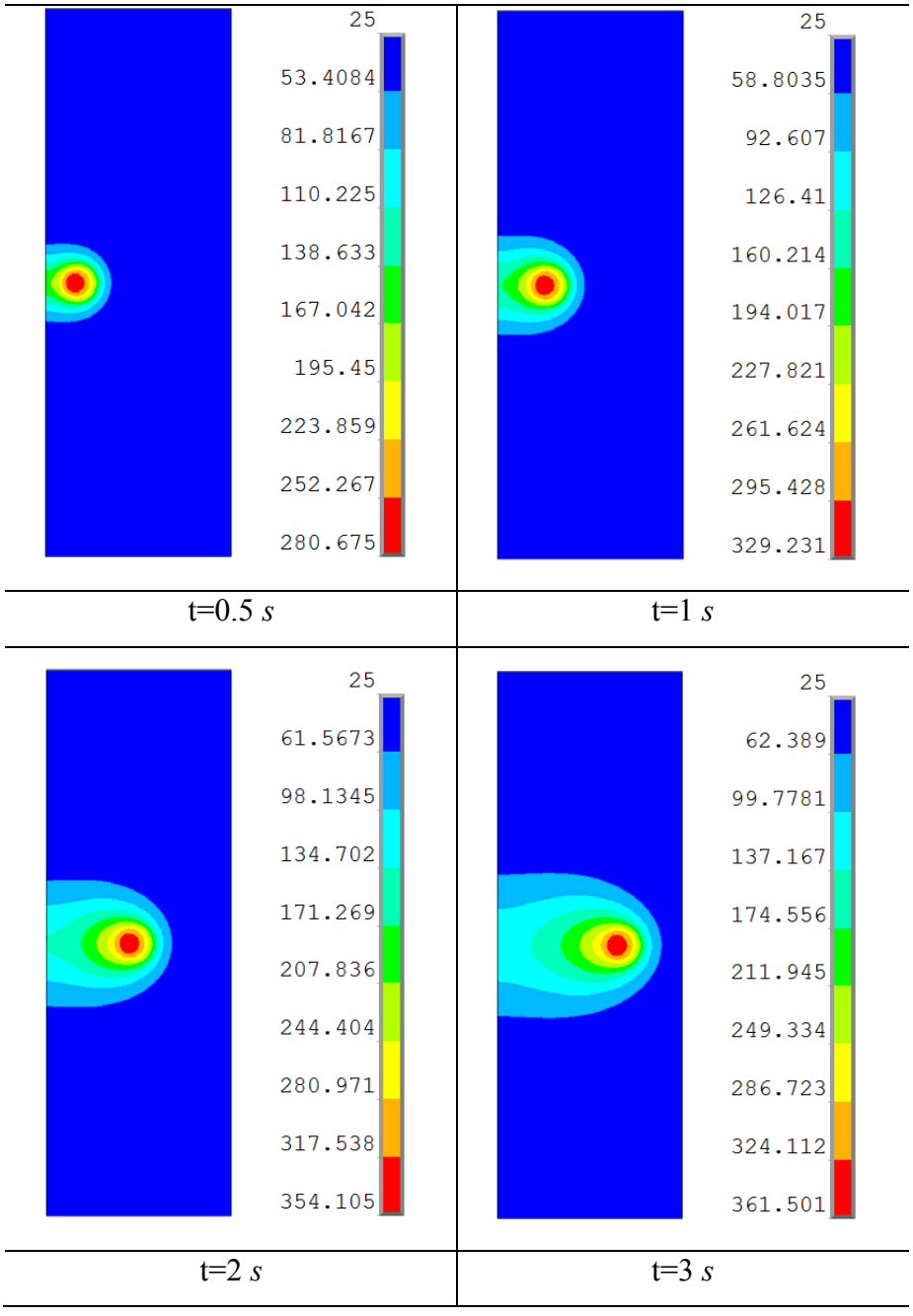

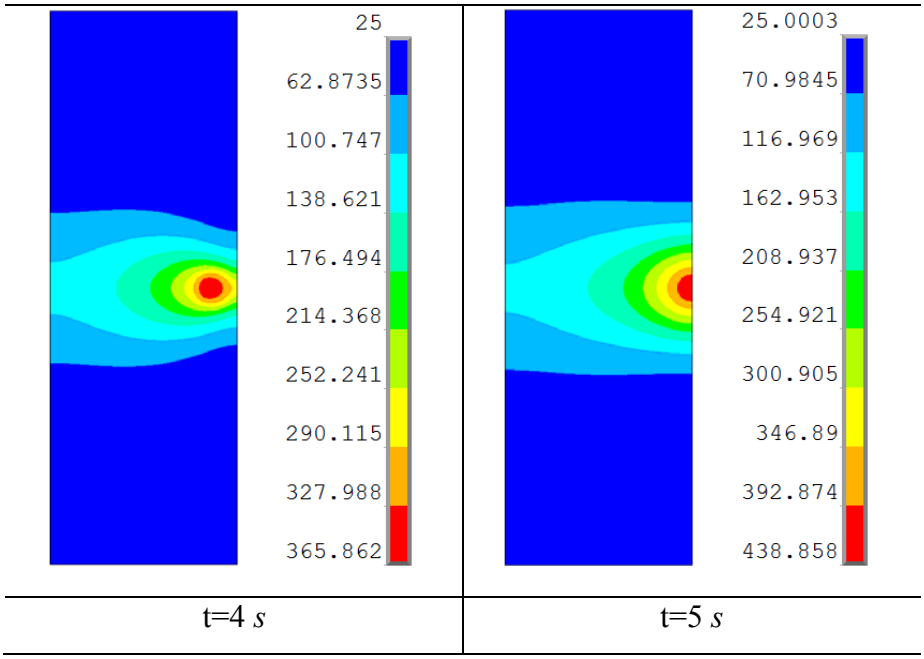

Fig. 6.2 The temperature field of at the PET-Ti interface of a LAMP joint as a function of time (laser power 55 W, laser travel speed 4 mm/s, pulsed duration 8 ms).

An example of the temperature profile of the joins formed using different laser power outputs at a processing time of 3 s is shown in Fig. 6.3. The maximum temperatures at the centre of the join line for laser powers of 30 W, 45 W, 55 W, 65 W and 75 W were 268 °C, 321 °C, 362 °C, 383 °C, and 416 °C, respectively. Given that the melting point of PET is about 260 °C [49] and the pyrolysis temperature is about 300 °C [124], it is apparent that a laser power of 30 W is sufficient to melt the PET material. To verify the simulated temperature of the join, a thermal infrared imager was used to capture the temperature of the join. Fig. 6.4 compares the temperature recorded by the imager and the simulated temperature obtained at the centre of the join. The results show that the two set of data compared satisfactorily. The cause of the temperature peak at the end of a laser scan is at present unsure. This may be due

to the low thermal conductivity of Ti at about 600K (327℃) [125] as well as the increase in laser absorption coefficient when the surface temperature increases.

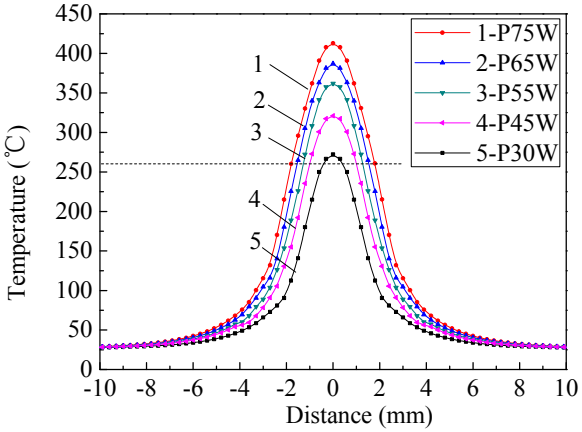

Fig. 6.3 The temperature profile across the centre of the join line for different laser processing powers at a joining time of 3 s.

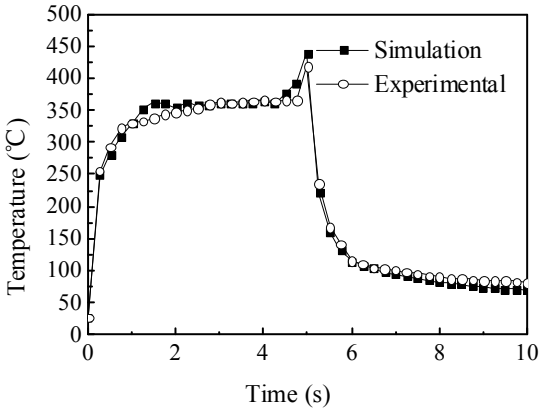

Fig. 6.4 A comparison of the simulated and measured temperatures of the centre of the join (laser power 55 W, travel speed 4 mm/s and pulsed duration 8 ms).

Using the results of Fig. 6.3 and assuming that a bond starts to form at a temperature of 260 °C (i.e. the melting point of PET), the join width can be determined. Fig. 6.5 shows the predicted bond width using the simulated

temperature data and the measured width from the experimental results. The two set of data compare well. The results presented in Figs. 6.4 and 6.5 indicate that the ANSYS thermal analysis is acceptable for the simulation of the temperature profile of the joint in the LAMP process.

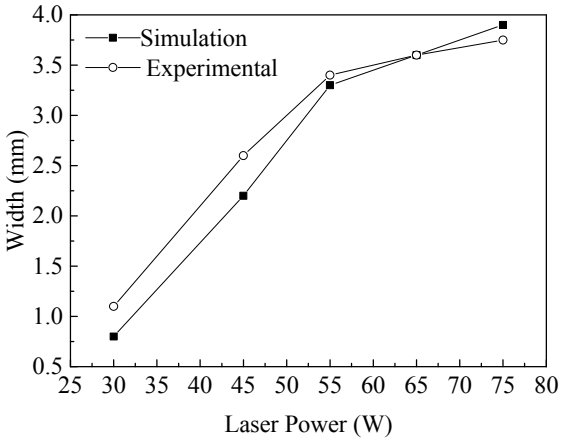

Fig.6.5 The predicted and the measured bond width for various laser processing powers.

6.3 Simulation of joint temperature profile for U-LAMP

For the U-LAMP joining process, both the laser source and ultrasound are the energy providers. Since the applied laser energy, other material properties and initial boundary conditions remain unchanged for both LAMP and U-LAMP, the study therefore just focued on the effect of ultrasound on the temperature changes. The established models for ultrasonic plastic joining [126-132] were used as the basis of this analysis, in which interfacial friction and volumetric viscoelastic heating mechanism both play a key role.

With regard to friction, the difference in stiffness between plastic and metal will cause a difference in longitudinal deformation between the two materials and leads to slippage and friction at the interfaces during ultrasonic

joining [133]. However, this effect is considered important when the plastic is in a solid state. Once the plastic melts, friction becomes insignificant. Therefore, the effect of ultrasonic vibration on temperature change only applies to areas of the joint where the temperature is below the melting point of the plastic, which in this case is 260 °C.

Pertaining to volumetric viscoelastic heating, it is caused by deformation of the plastic at relatively high temperatures due to ultrasonic vibration. Viscoelastic heat is generated because a hysteresis loop forms in the loading and unloading of the plastic material at elevated temperatures. The work done by the ultrasonic sonotrode is to overcome the internal friction of macromolecular segments of the polymer [134].

To study the effect of friction and viscoelastic heating on thermal behaviour, a coupled structural-thermal model was proposed with the following assumptions:

(i) Ultrasound absorption in plastic is considered to be uniform and is independent of temperature.

(ii) The shape of the polymer sheet is considered to be unchanged during vibration.

(iii) The energy for bubble formation and subsequent changes are not considered.

Both the friction and viscoelastic induced-heating effects originate from deformation of the plastic material. The following section examines the deformation behaviour of the material.

6.4 Numerical analysis of deformation behaviour

Under the condition of ultrasonic vibration, deformation of the polymer sheet can be determined using the following wave-motion equation in solids [135]:

$$\left(\gamma_{lame}+2\mu_{lame}\right)\nabla\left(\nabla\cdot u\right)+\mu_{lame}\nabla^2 u=\rho\frac{\partial^2 u}{\partial t^2} \tag{6.8}$$

where γ_{lame} and μ_{lame} are Lame constants, ρ is the material density. This wave-motion can be solved using the equation:

$$\mathrm{M}\ddot{u}\left(t\right)+\mathrm{C}\dot{u}\left(t\right)+\mathrm{K}u\left(t\right)=F\left(t\right) \tag{6.9}$$

where M, K and C represent the structural mass, stiffness, and damping matrixes, respectively.

Excitation of ultrasound ($F(t)$) can be expressed as:

$$F_A\left(t\right)=\begin{cases} W_1F_0\sin\left(2\pi ft\right), & \dfrac{1}{f}\left(n-\dfrac{1}{2}\right)\le t\le\dfrac{n}{f} \\ 0, & \dfrac{1}{f}\left(n-1\right)\le t\le\dfrac{1}{f}\left(n-\dfrac{1}{2}\right) \end{cases} \tag{6.10}$$

where f is the ultrasonic frequency, n stands for the cycle numbers, W_1 is the ultrasonic wave transmission coefficient of the transducer tool (including the Ti and PET sheets), F_0 represents the amplitude of the excitation force, which can be expressed as :

$$F_0 = 2\rho f \xi \tag{6.11}$$

where ξ is the amplitude along the ultrasonic transverse direction.

When the vibration of the ultrasonic horn is in the vertical direction, a compressive force is produced in the workpiece; this induced compressive force will only be active when the horn is in contact with the specimen (i.e. only during half-period of each vibration cycle Fig. 6.6). Therefore, the compressive force appears in the form of a half-sinusoidal wave of frequency 28 kHz.

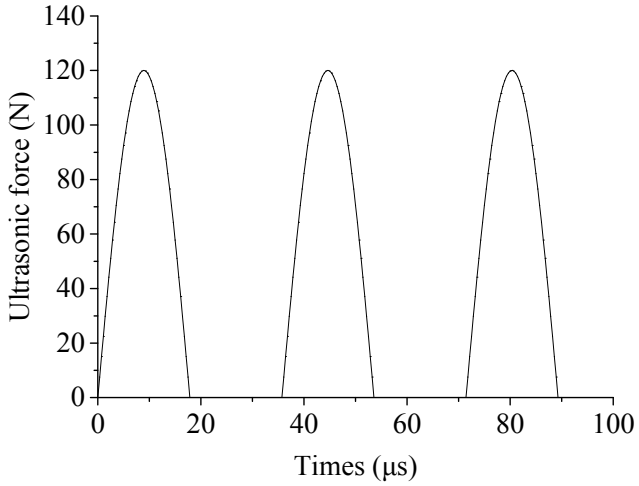

Fig. 6.6 Measured force signal during ultrasonic excitation.

Based on Eqns. (6.8) – (6.10), transient structural analysis can be achieved under a given cyclic excitation condition. The analysis was simplified by applying a 2-dimensional model. The physical properties of the PET sheet are presented in Table 3.5. ANSYS software was used to simulate ultrasound propagation and was employed for transient structural analysis. The changes of strain of the polymer due to vibration produce viscoelastic and friction induced-heating effects which are studied in the following sections.

6.5 Numerical analysis of the heating effects

6.5.1 Viscoelastic heating

Polymer deformation at elevated temperatures caused by ultrasonic vibration will generates viscoelastic heat. Based on the generalised Maxwell model, the Arrhenius and semi-empirical WLF models [129-130, 136-137], a model to study viscoelastic heating was established.

It is assumed that each unit cell inside the polymer experiences a uniaxial normal stress ($\sigma(t)$) that is in the form of sine function with the same frequency of an ultrasound (Fig. 6.7). Also, the polymer material does not contain any internal imperfections and the ultrasound does not introduce any to the polymer either, during processing. The frequency and the amplitude of vibration are the same as the sonotrode.

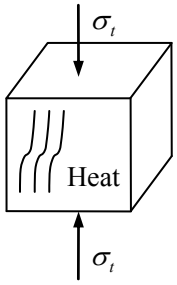

Fig. 6.7 Simplified loading conditions for one-unit cell of the polymer sheet [134].

Mathematical Modelling

Figure 6.8 shows an illustrative stress–strain curve of plastic materials in one cycle of vibration. Since, the loading curve and the unloading curve do not follow each other, a hysteresis loop is formed. The area of the hysteresis

loop relates to the work done by the ultrasonic sonotrode to overcome the internal friction of the macromolecular segments during one cycle of vibration. Thus, the heat induced via the micro unit cell in each unit time is calculated as [134]:

$$Q_{bulk} = f\oint \sigma(t)\,d\varepsilon(t) = f\sigma_0\varepsilon_0\omega\int_0^{2\pi/\omega}\sin\omega t\cos(\omega t-\delta)\,dt = f\pi\sigma_0\varepsilon_0\sin\delta \quad (6.12)$$

in which f is the vibration frequency, ε_0 and σ_0 are strain and stress, respectively; δ is the strain loss angle (from the result of rotational rheometer analysis, the loss angle (δ) of PET film was determined to be 0.559); ω is the sonotrode's angular frequency.

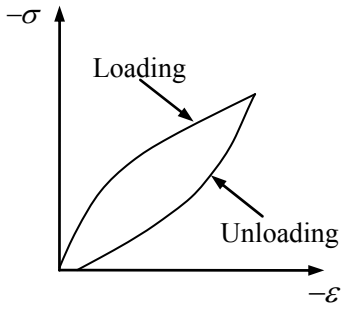

Fig. 6.8 Illustrative stress-strain curve of a polymeric material in one cycle of vibration.

The complex modulus of the plastic can be simplified through describing the stress and strain in a form of complex number, which is given as [134]:

$$E^* = \left(\frac{\sigma_0}{\varepsilon_0}\right)(\cos\delta + i\sin\delta) = E' + iE'' \quad (6.13)$$

where the storage modulus (*E'*) and the loss modulus (*E''*) can be written as [134]:

$$E' = \sigma_0 \cos\delta / \varepsilon_0 \tag{6.14}$$

$$E'' = \sigma_0 \sin\delta / \varepsilon_0 \tag{6.15}$$

By substituting Eqn (6.15) into Eqn (6.12), the heat generation rate (Q_{bulk}) can be rewritten [134] as:

$$Q_{bulk} = f\pi\varepsilon_0^{\,2}E'' \tag{6.16}$$

According to Eqn 6.16, it is clear that viscoelastic heating is correlated to the frequency and amplitude of vibration, and the polymer loss modulus (*E''*). Given that the thickness of both the Ti and PET sheets are just 1 mm, amplitude attenuation of vibration in the propagation direction of ultrasound can be ignored. Both loading frequency and temperature affect the loss modulus of the plastic. At high-frequency loading conditions (e.g. ultrasonic vibration), the loss modulus can be obtained by the method of Time-Temperature-Superposition [138–140]. Therefore, the complex modulus as a function of frequency and temperature can be expressed using the generalized Maxell model:

$$E^* = \sum_{j=1}^{n} \frac{E_j \omega^2 \tau_j^{\,2}}{1+\omega^2 \tau_j^{\,2}} + i\sum_{j=1}^{n} \frac{E_j \omega \tau_j}{1+\omega^2 \tau_j^{\,2}} \tag{6.17}$$

in which *j* represents the order number of the model, E_j and τ_j are the relaxation time and static relaxation modulus of relevant Maxwell unit. Ω represents the angular frequency of the applied loading.

The time of relaxation can be determined by applying the

semi-empirical WLF [136, 137] and the Arrhenius equations [129]:

$$\begin{cases} \tau_j(T) = 10^{\frac{H}{2.303R_0}\left(\frac{1}{T}-\frac{1}{T_S}\right)} \times \tau_j(T_S) & T \le T_g \\ \tau_j(T) = 10^{\frac{-C_1(T-T_S)}{C_2+T-T_S}} \times \tau_j(T_S) & T \ge T_g \end{cases} \tag{6.18}$$

in which $\tau_j(T)$ is the relaxation time, $\tau_j(T_s)$ is the relaxation time under a relevant reference temperature T_s, R_0 is the gas molar constant, H is the activation energy, and C_1 and C_2 are constants.

Using Eqns 6.16)–(6.18), the viscoelastic heating rate as a function of temperature and frequency can be written as:

$$\begin{cases} Q_{bulk}(T,\omega,\mathrm{z}) = f\pi\varepsilon_0{}^2 \sum_{j=1}^{n} \dfrac{E_j\omega 10^{\frac{H}{2.303R_0}\left(\frac{1}{T}-\frac{1}{T_S}\right)} \times \tau_j(T_0)}{1+\omega^2 10^{\frac{2H}{2.303R_0}\left(\frac{1}{T}-\frac{1}{T_S}\right)} \times \tau_j{}^2(T_0)} & T \le T_g \\ Q_{bulk}(T,\omega,\mathrm{z}) = f\pi\varepsilon_0{}^2 \sum_{j=1}^{n} \dfrac{E_j\omega 10^{\frac{-C_1(T-T_S)}{C_2+T-T_S}} \bullet \tau_j(T_0)}{1+\omega^2 10^{\frac{-2C_1(T-T_S)}{C_2+T-T_S}} \bullet \tau_j{}^2(T_0)} & T \ge T_g \end{cases} \tag{6.19}$$

6.5.2 Friction

Since the stiffness of the PET sheet is significantly lower than that of the Ti sheet, deformation of the plastic is greater than that of the Ti sheet. This leads to slippage and friction occurring at the PET-Ti interface. The heat generation by friction under an ultrasonic cycle can be expressed as [133]:

$$Q_{\mathrm{fric}}(x) = \alpha_h^2 \frac{\omega}{\pi} \mu \left| \sigma_{yy}^*(x) \delta u^*(x) \right| \tag{6.20}$$

where μ is the coefficient of friction, α_h is an empirical hammering correction factor. If no hammering occurs, α_h=1, with $\delta u^*(x)$ the horizontal displacement discontinuity at the interface and $\sigma_{yy}{}^*(x)$ the vertical stress at the interface. These two values can be obtained by using the deformation analysis presented in Section 6.4, which can be expressed as [133]:

$$\delta u^*(x) = \frac{\delta u(x)}{\sin(\omega t)} \tag{6.21}$$

$$\sigma_{yy}^*(x) = \sigma^*(x) \bullet e_y \bullet e_y \tag{6.22}$$

6.6 Results and discussion

Fig. 6.9 shows the temperature field of a U-LAMP join at the PET-Ti interface as a function of time under the condition of a laser processing power of 55 W. Comparing the results with those of a LAMP joint (Fig. 6.2), the temperature increase caused by ultrasound was insignificant, a maximum increase of about 2% in temperature was obtained at any position of the bonded area. The results reveal that the influence of ultrasonic vibration on temperature rise due to friction and viscoelastic heating effects is negligible. This is considered to be reasonable, when considering the friction effect, since the simulation results show that the temperature of the un-melted plastic ahead of the laser source reaches the melting point very quickly (less than 0.11 s). The slippage and friction at the interface virtually disappear once the plastic is melted. Therefore, the temperature increase due to friction heat is very limited. For viscoelastic heating, when the temperature reaches the glass transition temperature (Tg), the viscoelastic effect is at its maximum [133]. In U-LAMP,

the length of time dwell around Tg is very short (less than 0.06 s), and in this case, the ultrasonic vibration application time spent is too brief. Thus, the total heat input caused by viscoelastic dissipation is also limited.

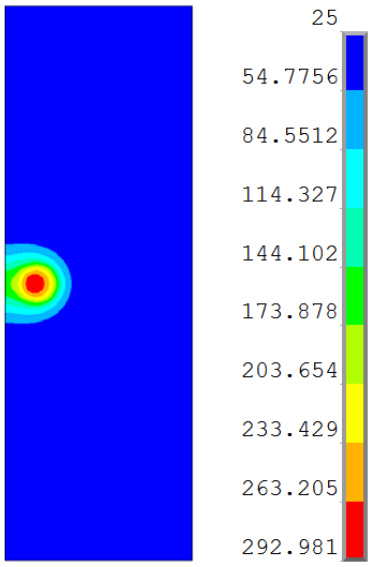

t=0.5 *s*

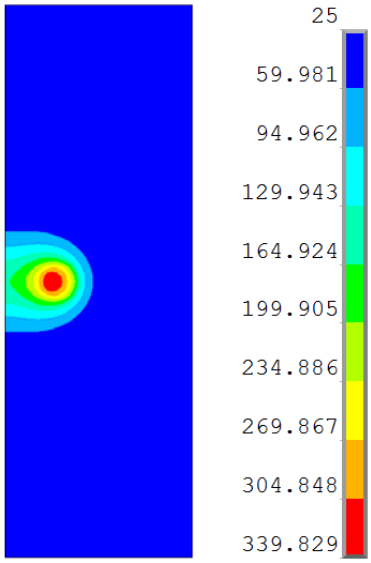

t=1 *s*

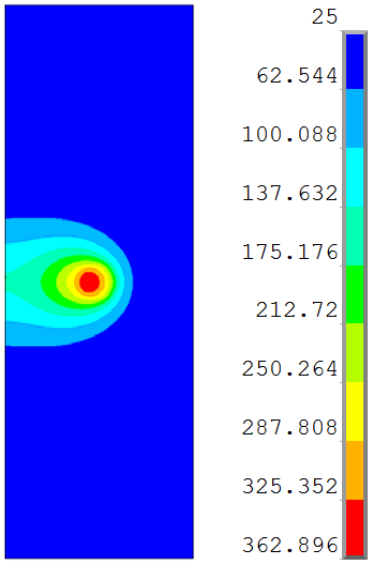

t=2 *s*

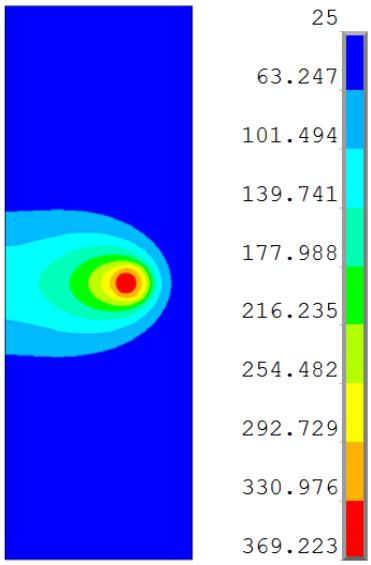

t=3 *s*

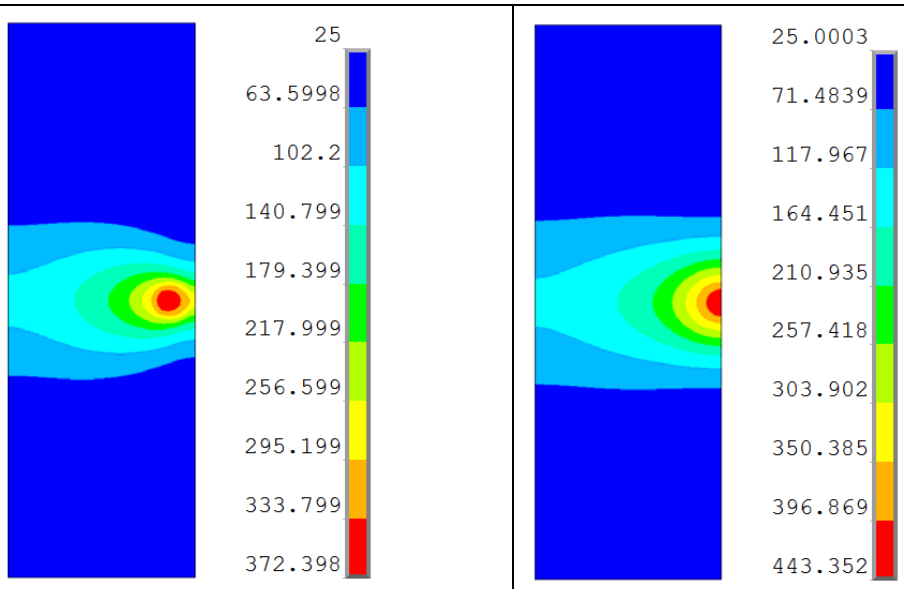

t=4 *s*	t=5 *s*

Fig. 6.9 The temperature field of at the PET-Ti interface of a U-LAMP joint as a function of time (laser power 55 W, laser travel speed 4 mm/s, pulsed duration 8 ms).

6.7 Chapter summary

(i) The ANSYS thermal analysis is acceptable for the simulation of the joint temperature profile of the LAMP and U-LAMP processes.

(ii) The effect of ultrasonic vibration on raising the joint temperature due to friction and viscoelastic heating effects is insignificant.

Chapter 7

Ultrasound-Aided Laser Joining with a Three Holes Transducer Tool

7.1 Introduction

The new ultrasound-aided laser joining method (U-LAMP) has been demonstrated in the previous chapter through a study of joining polyethylene terephthalate (PET) to pure titanium (Ti) under a low laser power condition. U-LAMP has been shown to be superior to LAMP in terms of failure load. The formation of bubbles was prevented as a low laser power was used to avoid decomposition of the plastic, and therefore the laser-induced bubble problem was not encountered. Under a low laser power condition, the benefit of ultrasonic action is to obtain a better contact between the metal surface and molten plastic.

Building on the realisation of the low laser power study, the present chapter presents a further development of U-LAMP to address the laser-induced bubble problem, with the aim of controlling the movement of bubbles at the plastic-metal join interface when a relatively high laser power is used. A three-blind-holes transducer tool was employed to prove the idea that under ultrasonic vibration, bubbles will move and be collected in low pressure regions above the location of the cavities during the joining process. The effect of the surface profiles of the ultrasonic tools, including a flat surface tool and a three-blind-holes tool, on joint appearance is firstly presented. The movement of the bubbles is described in Section 7.3.4 and is based on consideration of the

secondary Bjerknes forces.

7.2 Joint appearance

Examples of the joint appearance of the LAMP and U-LAMP samples are shown in Fig. 7.1. Both specimens were joined using the same laser conditions as shown in Table 3.10, but with the latter, ultrasound (28 kHz) was employed. One of the transducer tools used for the experiment has a flat and smooth surface configuration (Fig. 3.9), and with such an arrangement, it is expected that the join area will experience a uniform pressure induced by ultrasound vibration. An optical examination of the LAMP joints, i.e. without ultrasonic aid, found that networks of bubbles were developed and remained in the centre of the joint, after the plastic had solidified, where the laser power is considerably higher. This happened because decomposition of the polymer occurred (Fig. 7.1(a)). On the other hand, though bubbles were still found in the U-LAMP joints, they were in a dispersed fashion (Figs. 7.1(b), (c)).

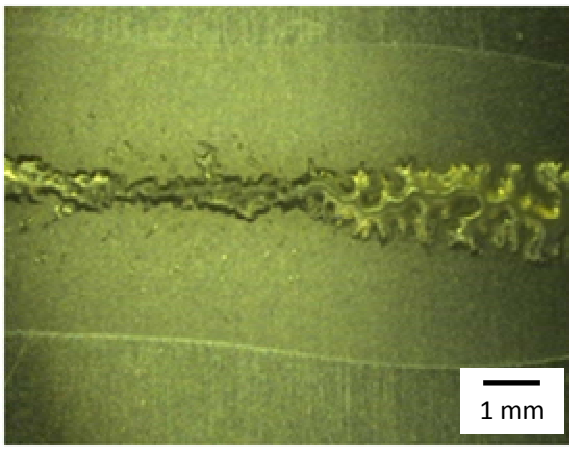

(a)

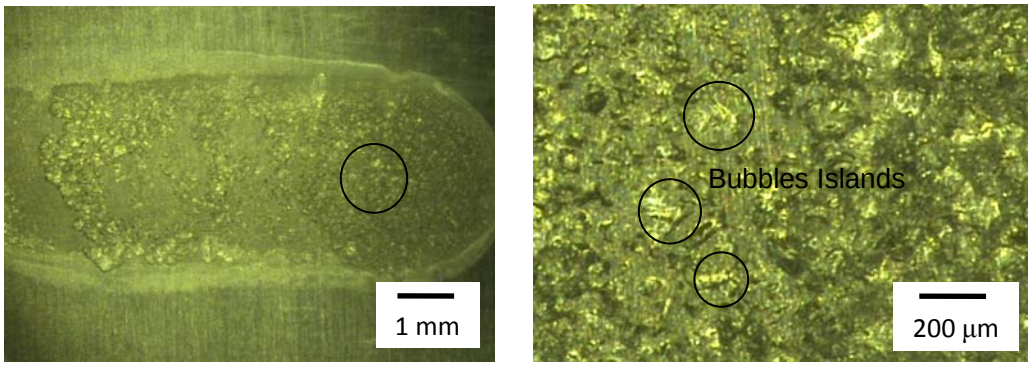

(b) (c) An enlargement of (b)

Fig. 7.1 Joint appearance of the (a) LAMP and (b, c) U-LAMP joined samples.

Fig. 7.1 shows that using an ultrasonic-aid tool with a flat surface can disperse the bubbles in the joint area. This may help to improve the strength of the joint. It is envisaged that if bubbles can be removed from the join, then a significant improvement in joint strength can be attained. With this in mind, a flat surface ultrasonic tool with circular blind holes was designed (Fig. 3.11), which was based on the concept that a cavity in the tool surface will cause a low pressure region to develop in the molten plastic, and this may cause bubbles to be collected in the designated region. This concept can be used to manipulate the movement of bubbles in the molten plastic before the polymer is solidified. The experimental results obtained for the blind-hole-design tool agree well with our expectation in which most of the bubbles were collected and coalesced into pockets of voids (Fig. 7.2). The locations of these pockets match the positions of the holes in the tool surface. The processing parameters of this specimen were exactly the same as those used for the LAMP specimen (Fig. 7.1). The following section examines the effect of the ultrasonic induced pressure in the workpiece on bubble movement.

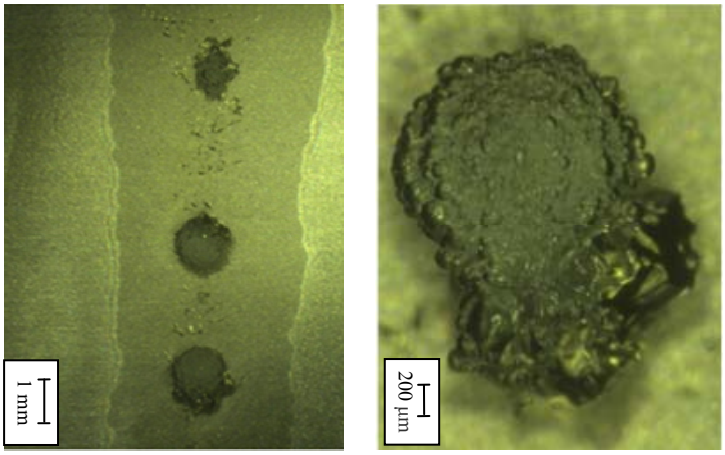

Fig. 7.2 Joint appearance of the sample produced using a tool surface with 3 circular holes, (L) showing the bubbles collected at regions above the holes; (R) an enlargement of one of these regions (laser power 55 W, frequency 20 Hz and joining speed 4 mm/s).

7.3 Mathematical model for bubble movement

In order to analyse the effect of the surface features of the ultrasonic tool on the movement of bubbles, it is necessary to study the pressure generated in the molten plastic by the ultrasonic tool. Applications of ultrasonic waves often require the transmission from one medium to another where their effects are to be realised. Considering the case of an ultrasonic transducer tool with a surface structure having 3-blind holes (Fig. 3.11), at position A of the workpiece, which is relatively far from a location of a surface hole, and position B, which is located above a surface blind hole. The transmission and reflection of ultrasonic waves from the transducer to the workpiece at these two locations are different, causing a pressure difference between these two locations.

7.3.1 Pressure at position A

At position A, the effects of transmission and reflection of ultrasonic

waves take place at the interface between the transducer tool and the metal specimen, where the transducer is sending out a plane pressure wave towards the Ti sheet. Since the acoustic properties of the transducer tool and Ti sheet are different, partial reflection at the interface is expected with a certain degree transmitted through to the Ti sheet (Fig. 7.3).

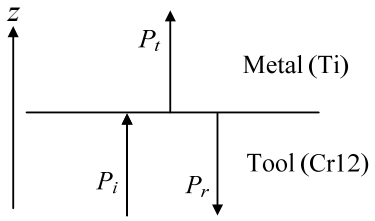

Fig.7.3 Reflection and transmission at the interface between transducer tool and Ti sheet.

The incident waveform (P_i), the reflected waveform (P_r), and the transmitted waveform (P_t), can be represented as [141]

$$P_i = \xi \exp j(\omega t - k_1 x) \tag{7.1}$$

$$P_r = \xi R_{tool-Ti} \exp j(\omega t + k_1 x) \tag{7.2}$$

$$P_t = \xi T_{tool-Ti} \exp j(\omega t - k_2 x) \tag{7.3}$$

where ξ is the vibration amplitude, $j=\sqrt{-1}$, z is displacement, k_1 *and* k_2 are the stiffness coefficients of the transducer tool and the Ti sheet, respectively. ω is the angular frequency, $R_{\text{tool-Ti}}$ and $T_{\text{tool-Ti}}$ are the pressure reflection and transmission coefficients between the transducer tool and the Ti sheet, respectively.

It is assumed that the transducer tool and Ti sheet are in intimate contact and the boundary conditions of pressure and velocity (displacement) at z=0 at the interface between the tool and the Ti sheet remain the same. Based on the definition of acoustic impedance:

$$1 + R_{tool-Ti} = T_{tool-Ti} \tag{7.4}$$

$$\frac{1}{Z_{tool}}\left(1 - R_{tool-Ti}\right) = \frac{T_{tool-Ti}}{Z_{Ti}} \tag{7.5}$$

where Z_{tool} and Z_{Ti} are the characteristic acoustic impedances of the transducer tool and the concerned Ti sheet. Using Eqns. (7.4) and (7.5), the pressure transmission coefficient and the reflection coefficient can be determined:

$$T_{tool-Ti} = \frac{2Z_{Ti}}{Z_{Ti} + Z_{tool}} \tag{7.6}$$

$$R_{tool-Ti} = \frac{Z_{Ti} - Z_{tool}}{Z_{Ti} + Z_{tool}} \tag{7.7}$$

where $Z_{\text{tool}} = \rho_1 u_1$, $Z_{\text{Ti}} = \rho_2 u_2$; and ρ_1, ρ_2 and u_1, u_2, are the densities and sound propagation velocities of the transducer tool and the Ti sheet, respectively, which are given in Table 7.1.

Table 7.1 Density and sound velocity of the media

Media	Density (ρ) (kg/m^3)	Sound velocity (u) (m/sec)
Cr12 steel	7870	5948
Ti	4500	6069
air	1.19	330

At normal incidence, the intensity of the sound wave travelling in a material can be expressed as [141]:

$$I \equiv P_{\max}{}^2 / 2Z \tag{7.8}$$

$P_{\max}$ is the maximum pressure and can be expressed as [140]:

$$P_{\max} = 2\pi\xi f \rho u \tag{7.9}$$

where f is the vibration frequency, ρ is the density of the material, u is the velocity of the ultrasound. In the case of U-LAMP, the transducer sends out a plane pressure wave towards the Ti sheet, and the maximum incident pressure at the transducer tool surface ($P_{\max\,\mathrm{tool}}$) can be written as:

$$P_{\max tool} = 2\pi\xi f \rho_1 u_1 \tag{7.10}$$

The acoustic intensity of transmission between the transducer tool and Ti sheet can be conveniently determined based on the definition of acoustic intensity [141],

$$I_{Ti} = \frac{Z_{tool}}{Z_{Ti}} \left| T_{tool-Ti} \right|^2 I_{tool} \tag{7.11}$$

By Eqns (7.8), (7.10) and (7.11), the maximum transmission pressure that is transmitted to the Ti sheet ($P_{\max\,\mathrm{Ti}}$) is given by:

$$P_{\max Ti} = T_{tool-Ti} \times P_{\max tool} \tag{7.12}$$

Since the thickness of the Ti sheet (1 mm) is much smaller than the length of the transducer, the thickness of the Ti sheet can be ignored. Therefore,

the Ti sheet can be considered to be vibrated in phase with the transducer. Combining equations (7.10) and (7.11), the maximum pressure exerted on the molten plastic through the Ti sheet at position A can be expressed as:

$$P_{\max A} = P_{\max Ti} = T_{tool-Ti} \times P_{\max tool} = 2\pi T_{tool-Ti} \xi f \rho_1 u_1 \qquad (7.13)$$

7.3.2 Pressure at position B

Consider position B, which is located above a blind hole in the transducer tool. In this case, the ultrasonic wave is transmitted from the transducer, through the air, to the Ti sheet (Fig.7.4).

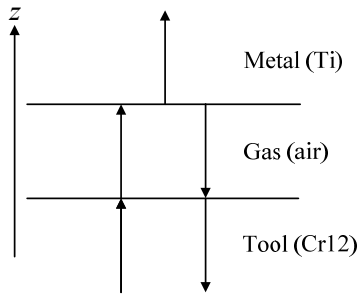

Fig. 7.4 Reflection and transmission at the interfaces of the compounded layer (the transducer tool, air and Ti sheet).

The multiple reflection and transmission of acoustic waves in the transducer tool, air and the Ti sheet can be treated as occurring in a compound layer (Fig. 7.4). The transmission coefficient of the compounded layer can be expressed as [141]:

$$T_{tool-air-Ti} = \left| \frac{4Z_{Ti}Z_{air}\left(\cos\psi - i\sin\psi\right)}{\left(Z_{Ti} - Z_{air}\right)\left(Z_{air} - Z_{tool}\right) + \left(Z_{Ti} + Z_{air}\right)\left(Z_{air} + Z_{tool}\right)\left(\cos\psi - i\sin\psi\right)^2} \right| \quad (7.14)$$

where Z_{air} is the characteristic acoustic impedance of air, and ψ is the phase advance of the plane wave passing through the air, which can be determined by [141]:

$$\psi = 2\pi f d_{hole} / u_{air} \quad (7.15)$$

where d_{hole} *=15* mm is the depth of the holes (air) in the transducer tool, u_{air} is the sound velocity in air, and in this case, $\psi = \pi/2$. (Substitute f=28 kHz, d=15 mm, u_{air}= 330 m/s into equation (7.15) yields $\psi \approx 2.5\pi$. The cycle function of cos x and sin x is 2π, then, in this case, $\psi = \pi/2$). Substituting $\psi = \pi/2$ into equation (7.14) yields

$$T_{tool-air-Ti} = \frac{4Z_{Ti}Z_{air}}{Z_{Ti}^{\ 2} + Z_{air}^{\ 2} + 2Z_{Ti}Z_{tool}} \quad (7.16)$$

By Eqns (7.10) and (7.16), the maximum pressure exerted on the molten plastic through the Ti sheet at position B can be expressed as:

$$P_{\max B} = T_{tool-air-Ti} \times P_{\max tool} = 2\pi T_{tool-air-Ti} \xi f \rho_1 u_1 \quad (7.17)$$

Substituting the data given in Table 7.1 into Eqns (7.6) and (7.16) yields:

$$\frac{T_{tool-Ti}}{T_{tool-air-Ti}} > 1 \quad (7.18)$$

Hence,

$$P_{\max A} > P_{\max B} \tag{7.19}$$

The above analysis shows that a surface cavity in the transducer tool causes a corresponding low pressure region to be developed in the molten plastic. This induced pressure change in the molten plastic has an effect on the movement of the laser-induced vapour bubbles. In the case of the 3-blind holes ultrasonic tool, the pressure acting at a position away from the hole (position A) is greater than that acting above the hole (position B). The pressure difference between these two regions can be determined using equations (7.13) and (7.17). The pressure difference in the molten plastic in turn creates an extra force acting on the bubbles which are located at high pressure regions. Therefore, under the influence of pressure difference, bubbles in the relatively high pressure regions (away from the hole) will migrate to the relatively low pressure regions (above the hole) and form a relatively large bubble there (Fig. 7.2).

7.3.3 Verification of pressure change due to surface cavities

To verify that the surface holes in the transducer tool can change the pressure acting on the molten plastic, the vibration amplitude at the two locations, position A and position B, were measured using a laser Doppler vibrometer (Polytec, PSV-400) (Fig. 7.5) (pressure is proportional to vibration amplitude, Eqn 7.9). The displacement measurements for these two positions are given in Fig. 7.6. The measured vibration amplitude of position A was about two times that of position B. This means that the pressure acting at position A should be greater than that acting at position B, i.e. $P_{max\,A} > P_{max\,B}$, which is in agreement with the pressure analysis results presented in sections 7.3.1 and 7.3.2.

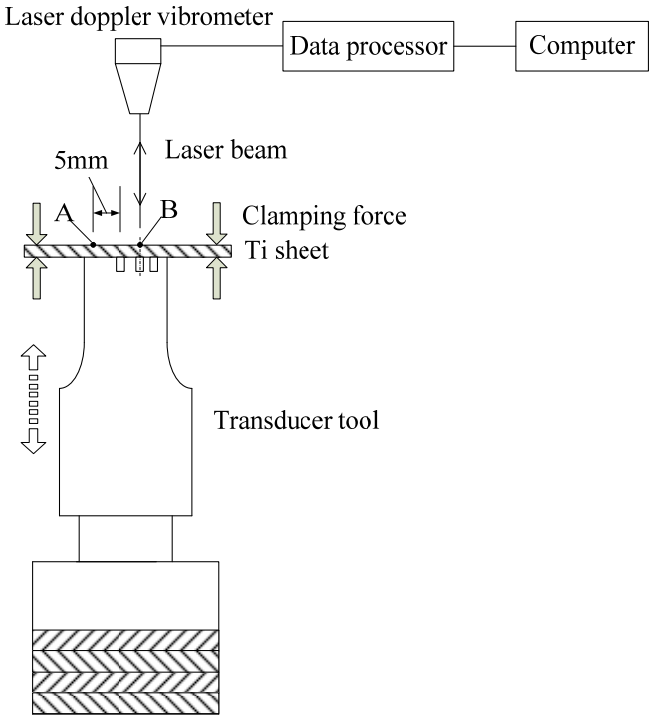

Fig. 7.5 The laser doppler vibrometer set up.

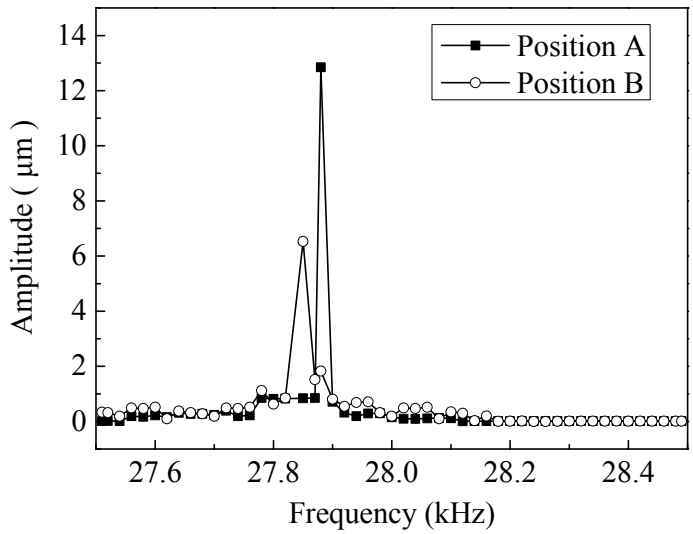

Fig. 7.6 Vibration amplitude of position A (away from the hole), and position B (just above a blind hole).

7.3.4 Bubble movement due to secondary Bjerknes force

In addition to the pressure difference effect, Bjerknes forces also play a part in causing bubbles to migrate to low pressure regions (position B). It has been recognised that the position and size of a bubble which is travelling in an acoustic field are mainly governed by the primary Bjerknes force (F_p) [34]:

$$F_p = -4/3\pi F_0 k_w \sin\left(k_w d\right) R^3\left(t\right)\sin\left(\omega t\right) \tag{7.20}$$

where k_w is the wave number, F_0 is amplitude of the acoustic pressure at the pressure antinodes, R is the time-dependent radius, ω is the angular frequency, t is time, and d is the distance between the bubble centre and the closest pressure antinodes. In U-LAMP joining, since the thickness of the PET sheet used is only 1 mm, and this dimension is relatively small when compared to the acoustic wavelength (212.5 mm), the bubbles in the joint are considered to be at the same plane, and therefore the primary Bjerknes force (F_p) can be ignored. Also, since the movement of the bubbles is confined to two dimensions, i.e. in the x and y directions, therefore the buoyancy force can also be ignored. With these conditions applied, the relative position of any two bubbles and the external forces acting on them can be illustrated with the schematic diagram shown in Fig. 7.7.

The secondary Bjerknes force between two adjacent bubbles travelling in an acoustic field is considered important, and is expressed as [142]:

$$F_B = -\frac{\rho}{4\pi {r_{12}}^2}\left\langle \dot{V}_1 \dot{V}_2 \right\rangle \tag{7.21}$$

where $\langle\ \rangle$ denotes the time average, ρ is the liquid density, $\dot{V}_1$ and $\dot{V}_2$ are

the derivatives of the volume of bubble_1 and bubble_2 respectively, and r_{12} is the space between two adjacent bubbles.

In an acoustic field, a bubble also experiences hydrodynamic forces, of which the drag forces acting along the x and y axes can be, respectively, expressed as [143]:

$$F_{vx} = 6\pi\mu R\dot{x}\frac{e + r_b\left(2\mu + 3\mu'\right)}{e + 3r_b\left(\mu + 3\mu'\right)} \tag{7.22}$$

$$F_{vy} = 6\pi\mu R\dot{y}\frac{e + r_b\left(2\mu + 3\mu'\right)}{e + 3r_b\left(\mu + 3\mu'\right)} \tag{7.23}$$

where μ is the liquid viscosity, e is surface viscosity coefficient, r is the bubble's radius (assuming a sphere), $\mu^{'}$ is the gas viscosity within the bubble, and y is the bubble centre co-ordinate on the y axis. Since the bubble is drifting in an acoustic field, the bubble radius $r_b \gg e$ and $\mu \gg \mu'$, equations (7.22) and (7.23) can be, respectively, shortened to:

$$F_{vx} = 4\pi\mu R\dot{x} \tag{7.24}$$

$$F_{vy} = 4\pi\mu R\dot{y} \tag{7.25}$$

According to Eqns (7.24) and (7.25), it can be deduced that the drag forces acting on a bubble are related to the liquid viscosity and the bubble's radius, which means that the larger the bubble is, the greater will be the drag force.

In the case of the 3-blind holes tool, the relatively large bubble produced at position B due to the pressure difference effect experiences a

greater drag force than the small bubbles under the action of the secondary Bjerknes force (F_B) (a mutual force). As a result, small bubbles will move towards the large bubble (Fig. 7.8).

The results obtained so far have shown that under the influence of ultrasonic vibration, a cavity in the transducer tool creates a low pressure region in the specimen above the location of a cavity. An analysis for the feature of an open channel in the ultrasonic tool also shows that a low pressure region is present above the channel, and is discussed in the Section 7.4.2.

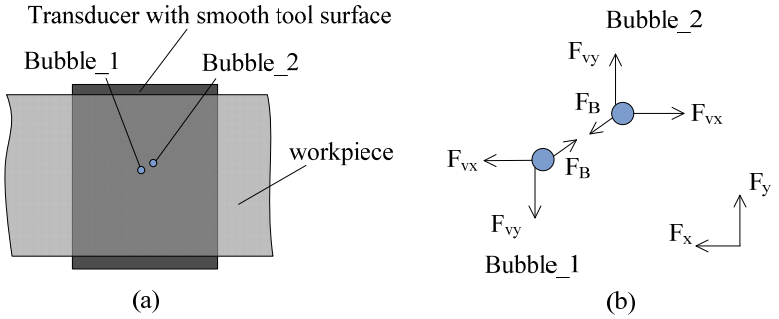

Fig. 7.7 (a) Relative position of the two bubbles in the molten plastic; (b) different external forces acting on bubble_1 and bubble_2 (of the same size).

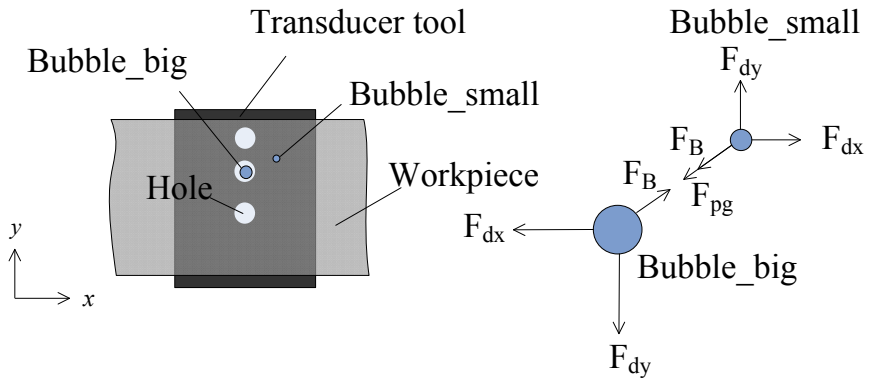

Fig. 7.8 Various external forces acting between a large bubble and a small bubble.

7.4 Chapter summary

Using ultrasonic-aid tools with a flat surface enable dispersion of the bubbles in the joint area. In order to investigate the movement of bubbles in the molten plastic, a three-blind-holes transducer tool was employed to test the idea that under ultrasonic vibration, bubbles would move to a low pressure region above the location of a cavity. A mathematical model has been established to describe the movement of laser-induced bubbles under the effect of ultrasonic vibration. The locations of pockets of bubbles found in the joint zone coincided with the positions above the blind holes of the transducer tool, where pressure is relatively low, and this result agrees well with the theoretical predictions.

Chapter 8

Ultrasound-Aided Laser Joining with an Open Channel Transducer Tool

8.1 Introduction

Given the promising results of being able to move bubbles in the molten plastic pool using an ultrasonic tool with three-blind-holes, it was envisaged that it may be possible to "drain" away bubbles in the joint by an appropriate transducer tool. With this in mind, the transducer tool with an open channel, which aims to provide a low pressure region for the bubbles to escape from the molten pool, was explored for U-LAMP.

The effects of the temperature field and the pressure field of the molten plastic on bubble movement were studied and analysed using finite element simulation, and the predicted results were validated with high speed camera images.

8.2 Joint appearance of U-LAMP joints

When the centre of the channel aligned with the joint centreline, laser-induced bubbles were developed along the centreline region of the joint where the laser power is at its peak (Fig. 8.1a). Based on the analysis presented in Chapter 7 for the blind hole transducer tool, accordingly, if the open channel is placed offset from the centreline of the joint, the bubbles could migrate from the central region of high pressure to the region of low pressure where the channel is lying underneath (Fig. 8.2).

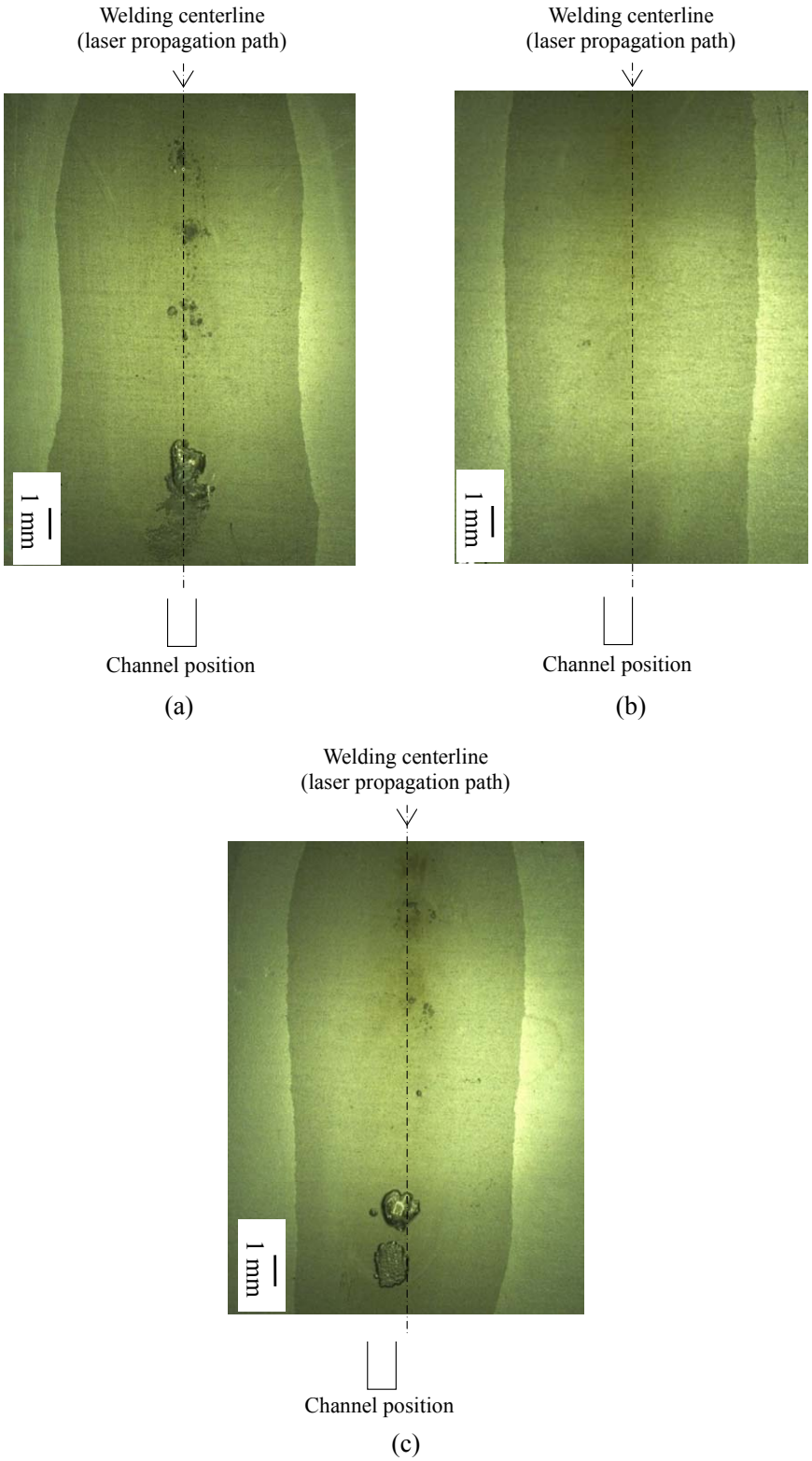

Fig. 8.1 Appearance of the joints produced using an open channel transducer with different offset to the left of the joint centreline (a) offset=0; (b) offset=0.5 mm; (c) offset=1.5 mm. (laser power 55 W, joining speed 4 mm/s, pulsed duration 8 ms)

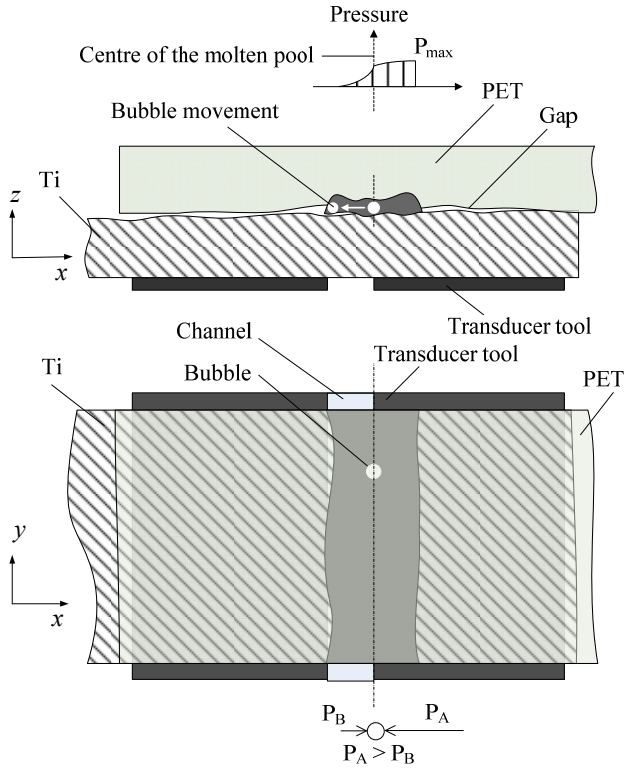

Fig. 8.2 A schematic diagram showing the effect of pressure difference on the movement of bubbles.

Fig. 8.1 shows the appearance of the joints produced by using an open channel transducer with different offsets to the left of the centreline of the weld, while the processing parameters remain the same as the joints shown in Fig. 8.1(a). In the case where there is no offset (0 mm) (Fig. 8.1a) or a relatively large offset (i.e. 1.5 mm (Fig. 8.1c), there are bubbles trapped in the joint. Fig. 8.3 shows the balance of forces for these two cases. On the contrary, if the edge of the open channel is in line with the centreline of the joint (offset = 0.5 mm), no large bubbles were found (Fig. 8.1b), and only few small pores were observed (Fig. 8.4). This demonstrates the effects of the induced pressure difference in driving bubbles away and escaping from the molten pool of the joint (Fig. 8.2). A detailed analysis on the combined effects of pressure field due

to transducer offset and thermal profile in laser joining on bubble motion is presented in section 8.4.

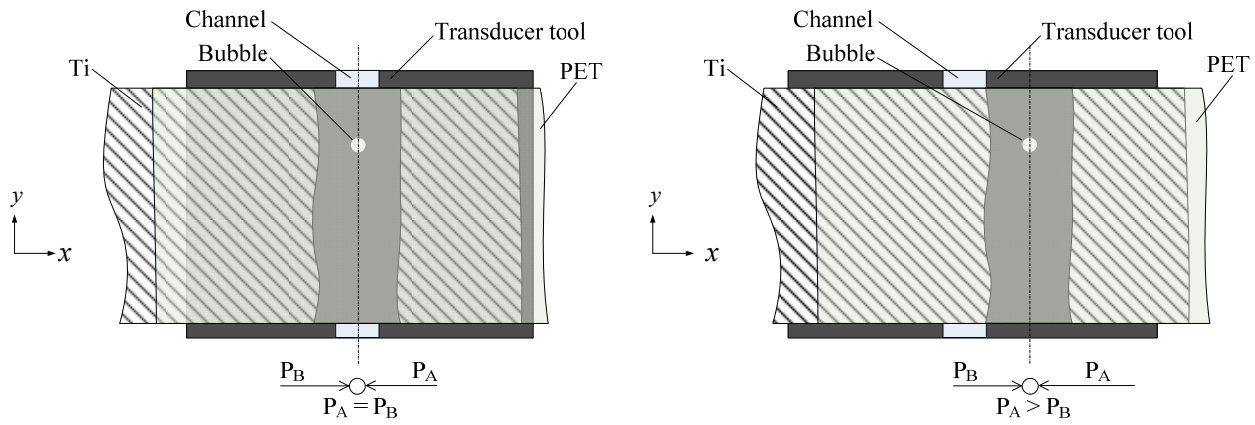

(a) (b)

Fig.8.3 A schematic diagram showing the pressure acting on a bubble (a) without offset of the transducer; (b) with a large offset of the transducer.

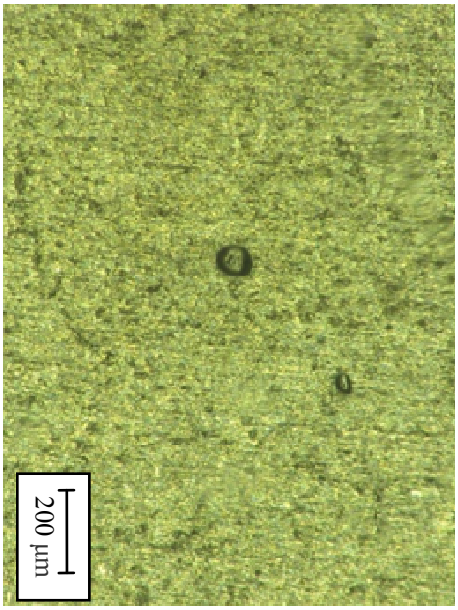

Fig. 8.4 Only few small bubbles can be found in the U-LAMP specimens produced by an open-channel tool with offset 0.5 mm to the left of the joint centreline.

8.3 Comparison of joint appearance produced by LAMP and U-LAMP

A series of experiments were conducted at different processing parameters using an open channel transducer with an offset 0.5 mm. Figs. 8.5-8.7 show the results of the joint appearance as a function of laser power, laser travel speed and laser pulsed frequency, respectively. These figures also compare the samples produced using LAMP, i.e. without ultrasound applied but using the same laser processing parameters.

In comparing the U-LAMP and the LAMP specimens, very encouraging results were obtained for the U-LAMP process. With the new ultrasound-aided laser joining method – using the conjoint action of a laser and ultrasound – and the offset technique, the amount of bubbles was significantly reduced and in most cases no sizable bubbles could be observed under an optical microscope. An examination of the cross-sections of the joined specimens showed that many bubbles were trapped at the interfaces of the joints of the LAMP specimens, while hardly any were found in the U-LAMP joined specimens (Fig. 8.8). The elimination of bubbles at the joint zone increases the joint strength.

The results also show that for both the U-LAMP and LAMP joints, the amount of bubbles appearing increases when the laser power and frequency increase; while increases in laser travel speed reduces the amount of bubbles. This is considered to be reasonable, since any increases in the energy absorbed by the metal part, either by increasing the laser power or frequency or by reducing the laser travel speed, can cause more polymer to be decomposed and form bubbles.

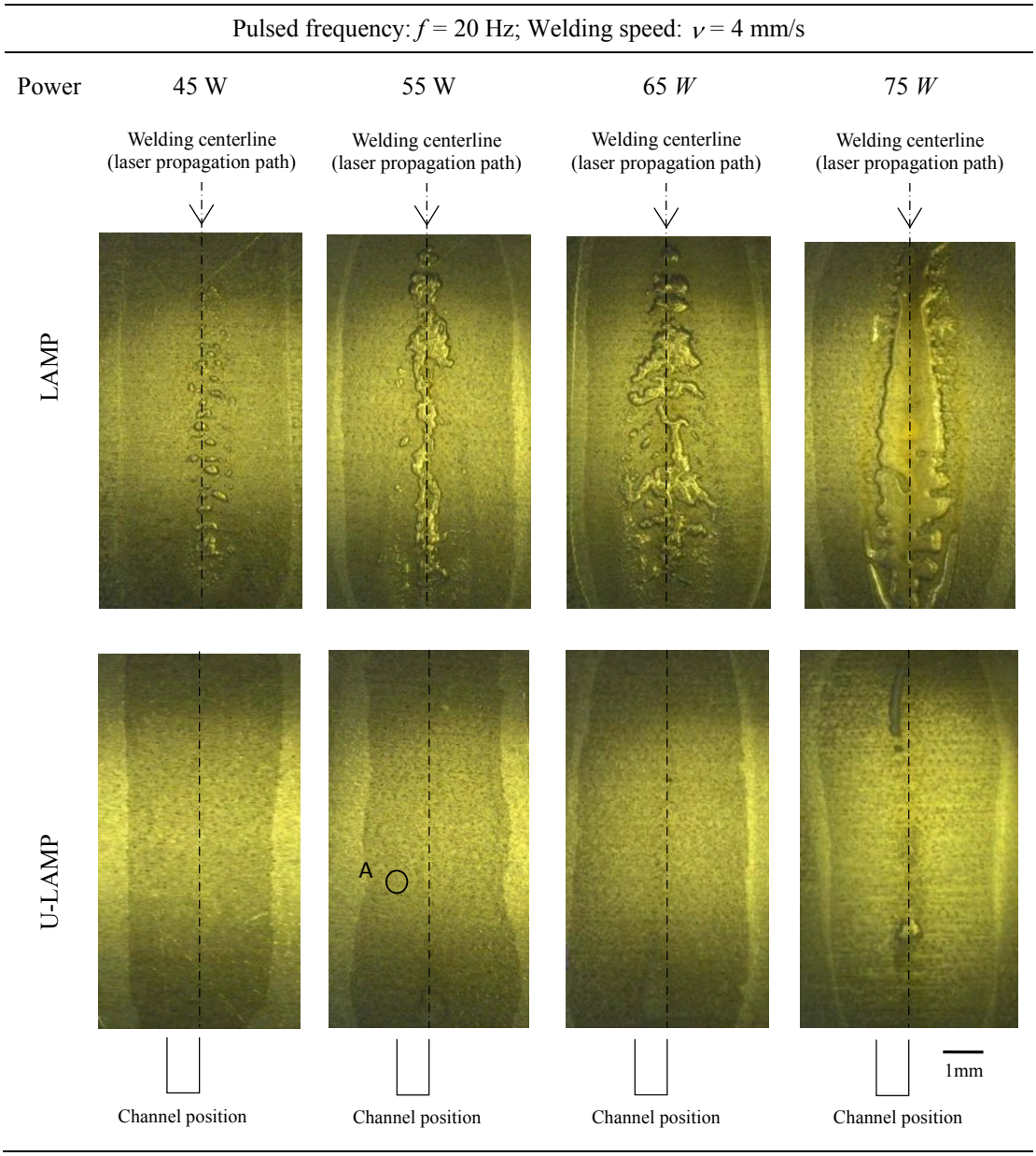

Fig. 8.5 Typical joint appearance as a function of laser power for both the LAMP and U-LAMP joining processes.

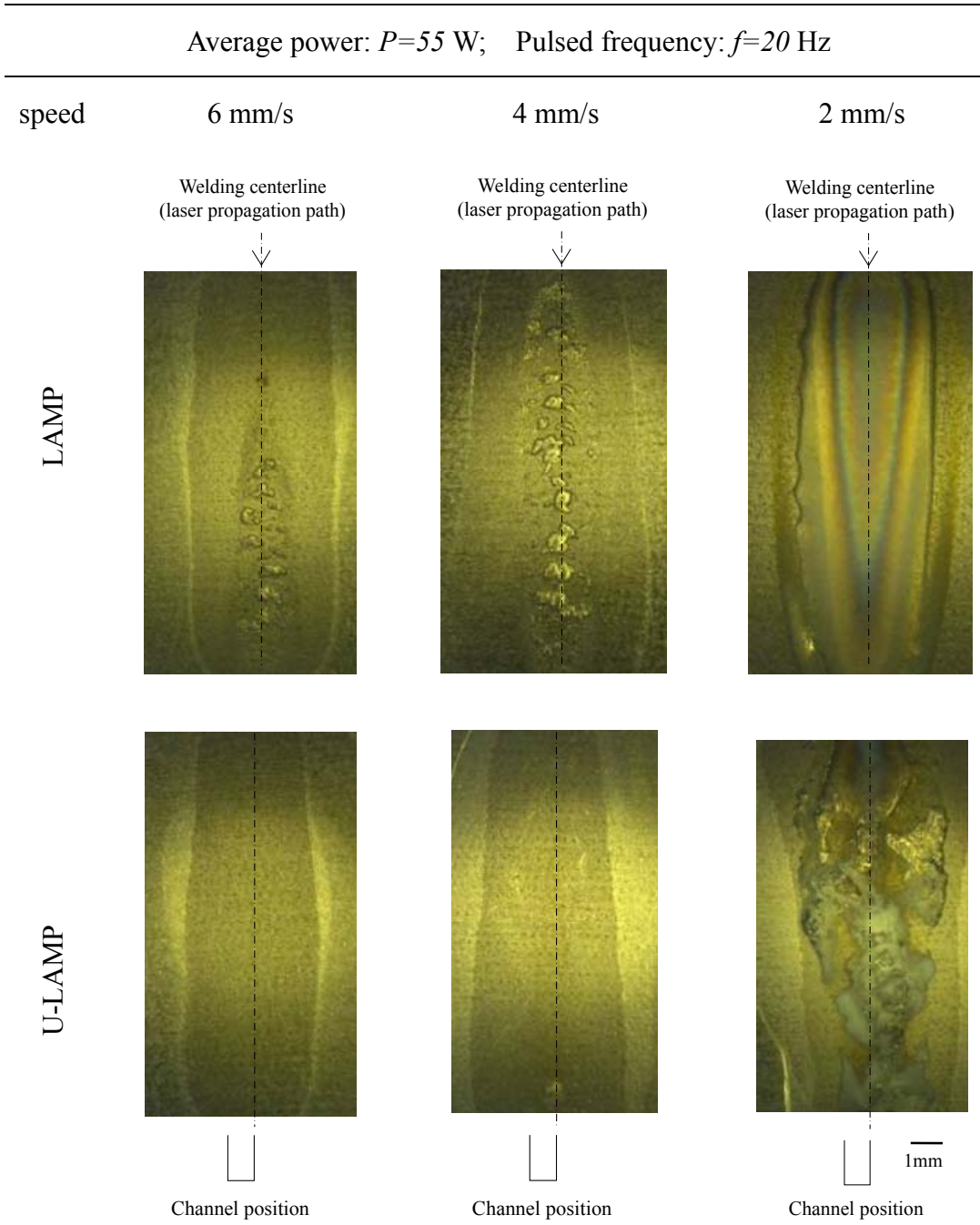

Fig.8.6 Typical joint appearance as a function of laser speed for both the LAMP and U-LAMP joining processes.

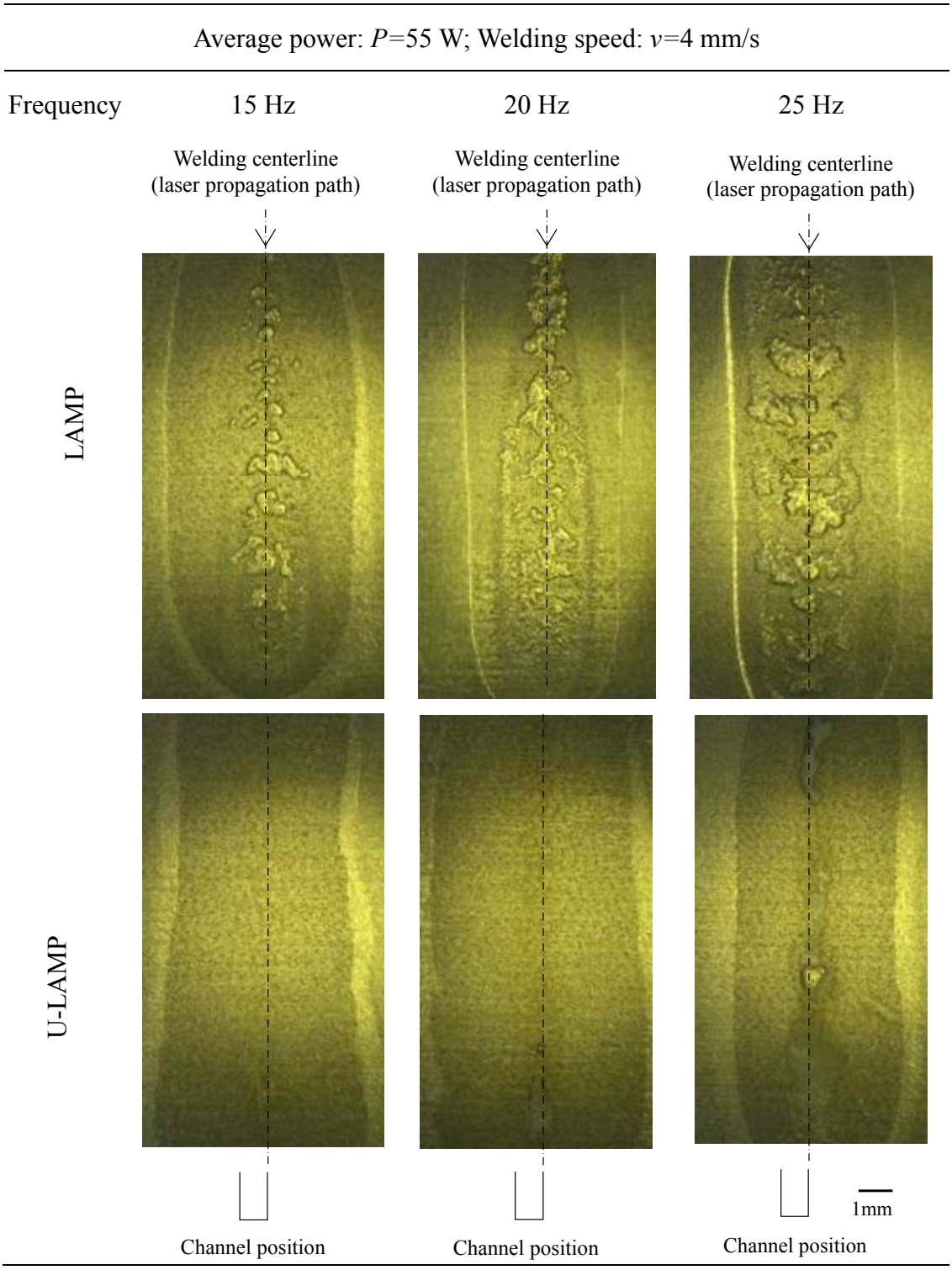

Fig. 8.7 Typical joint appearance as a function of laser frequency for both the LAMP and U-LAMP joining processes.

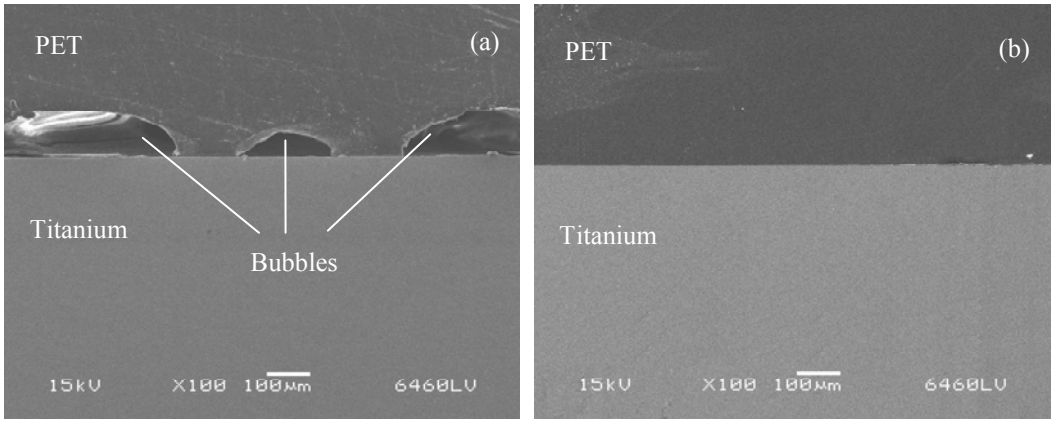

(a) (b)

Fig. 8.8 Cross-sections of the joins, showing the join interfaces of the (a) LAMP specimen and (b) the U-LAMP joined specimen (laser power 55 W, frequency 20 Hz and joining speed 4 mm/s).

8.4 Bubble trajectory

8.4.1 Effect of temperature field on bubble motion

The movement of bubbles in a fluid is affected by the temperature field. Under the condition of a temperature gradient, the evaporation momentum force becomes an important element in directing the trajectories of bubbles [144]. The evaporation momentum force (vapour recoil) is a force acting at the vapour-liquid interface caused by liquid to vapour phase transformation due to a rapid expansion of the evaporating liquid. Since the density of a vapour is much smaller than that of liquid, the evaporation momentum force acts on the interface in the form of equal and opposite reactions resulting from the increasing momentum of the evaporation mass on the interface [144].

When the bubble is growing, it expands outwards in all directions by the evaporation momentum force; if the temperature around the bubble is uniform, no resultant force will be present. However, if the temperature around

the sides of the bubble is not uniform, a higher evaporation rate occurs on the higher temperature side. This leads to a greater evaporation momentum force acting on the higher temperature side of the bubble compared to the lower temperature side. In this case, a resultant force is generated [144]. Kandlikar [145] proposed that such an effect can be used to control the trajectory of bubbles.

The temperature field analyses of LAMP and U-LAMP presented in Chapter 6 show that there is a temperature gradient in the molten plastic pool along the laser travelling direction. In this case, bubbles will move from a relatively cold zone towards a relatively high temperature region due to unbalanced evaporation momentum force.

8.4.1.1 Evaporation momentum force and pressure

The component force in the horizontal direction of the evaporation momentum force (F_M) can be expressed as [146]

$$F_M = \frac{q_I H_b}{h_{fg}} \frac{q_I}{h_{fg}} \frac{H_w}{\rho_v} = \left(\frac{q_I}{h_{fg}} \right)^2 \frac{H_w}{\rho_v} H_b \tag{8.1}$$

where q_I can be treated as the flux of interfacial heat, h_fg is the latent heat of vaporisation, ρ_v are the densities of vapour phases, H_b and H_w represent the height and width of the bubble, respectively.

Consider a vapour–liquid interface at which the liquid moves towards the interface at a rate v_l and the vapour travels away from the interface at a rate v_v (Fig. 8.9). The mass balance equation for an infinitesimal region (dA) at the interface can be written as [144]

$$\rho_l v_l dA = \rho_v v_v dA \tag{8.2}$$

where ρ_l is the density of the liquid phase.

Since the densities of the liquid and vapour phases are different, the vapour phase leaves the interface with a much greater velocity than that of the approaching liquid. The consequence is that the momentum of the evaporation mass on the interface is increased. The relationship between mass transfer along the bubble interface, the expansion speed of bubble, and the relevant evaporation momentum pressure (P_M) can be written as [144]:

$$P_M = \frac{F_M}{Area} = \frac{4\pi R^2 \dot{R} \rho_v}{4\pi R^2} v_l \left(\frac{v_v}{v_l} - 1 \right) \tag{8.3}$$

where F_M is the evaporation momentum force acting on the interface, which equals to the momentum variation rate of the evaporating mass; R is the radius of the bubble.

Based on the mass conservation equation (Eqn 8.2), the velocity ratio in Eqn (8.3) can be expressed in terms of the densities of the liquid and the vapour. Also, the velocity of the liquid can be related to the bubble growth rate. Thus, Eqn (8.3) can be written as [144]:

$$P_M = \dot{R} \rho_v \left(\frac{\dot{R} \rho_v}{\rho_l} \right) \left(\frac{\rho_l}{\rho_v} - 1 \right) \tag{8.4}$$

The density of the liquid is significantly larger than that of the vapour by several orders of magnitude. The term $\left(\frac{\rho_l}{\rho_v} - 1 \right)$ can be simplified to $\frac{\rho_l}{\rho_v}$.

This approximation has been widely employed in bubble growth models (such as Mikic et al. [147]). Thus, the pressure of the evaporation momentum can be expressed as:

$$P_M \approx \dot{R}^2 \rho_v \tag{8.5}$$

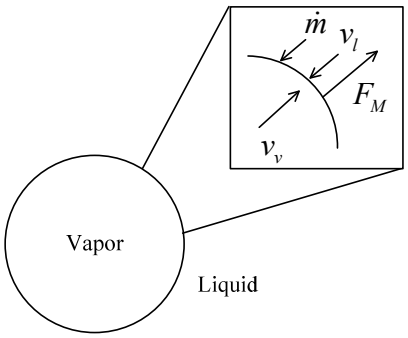

Fig. 8.9 A schematic diagram showing mass transfer of liquid and vapour on the interface of a bubble [147].

8.4.1.2 Temperature dependence of evaporation momentum pressure

The temperature profile of the molten plastic in laser joining is considered to influence the mass evaporation rate of the bubble, which is proportional to the evaporation momentum pressure [144]. Nikolayev et al. [148] found that the evaporation momentum pressure (P_M) (vapour recoil force/interface area) is related to the mass evaporation rate (flux) φ as:

$$P_M = \varphi^2 \left(\rho_v^{-1} - \rho_l^{-1} \right) \tag{8.6}$$

where φ represents the mass evaporation rate along the liquid–vapour interface.

The relationship between mass evaporation rate and the local liquid superheating can be expressed [144] as:

$$\varphi = c_p \Delta T \tag{8.7}$$

where c_p is the proportionality coefficient, ΔT represents the liquid superheat. The rate of change of the bubble mass can be calculated by integrating the flux of the mass of the interface [144]:

$$\dot{m} = 2\int_{-90}^{90-\theta_c} c_p \Delta T \pi R^2 \cos\theta d\theta \tag{8.8}$$

Also, the rate of change of bubble mass is related to the bubble growth rate as:

$$\dot{m} = 4\pi R^2 \dot{R} \rho_v \tag{8.9}$$

The proportionality constant (c) can be calculated by equating Eqns. (8.8) and (8.9).

Now, the evaporation momentum force in the horizontal direction can be determined [144]:

$$F_M = \int_{-90}^{90-\theta_c} \left(c_p \Delta T\right)^2 \left(\rho_v^{-1} - \rho_l^{-1}\right) \pi R^2 \cos^2\theta d\theta \tag{8.10}$$

8.4.1.3 Bubble encountered with asymmetric temperature distribution

To evaluate the effect of the resultant force of the evaporation momentum on the movement of a bubble as a result of uneven temperature distributions, the forces acting on a bubble were considered (Fig. 8.10), in which $T_1 > T_2$. Apart from the changes of liquid temperature in the vicinity of the

bubble, the thickness of the boundary layer as well as the temperature changes inside the layer are considered. The resultant force in the horizontal direction can be determined from the corresponding force on either side of the bubble (i.e. F_{M1} and F_{M2}), which can be calculated using Eqn 8.10.

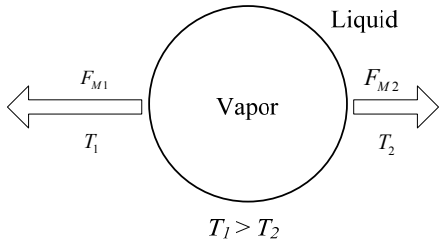

Fig. 8.10 A bubble presents in a temperature gradient, with the evaporation momentum forces acting on the bubble ($T_1 > T_2$) [147].

The difference between the horizontal forces (F_{M1} and F_{M2}) is the resultant force. The Marangoni force is ignored since the difference in surface tension is exceedingly small across the bubble.

8.4.1.4 Effect of evaporation momentum force on bubble in LAMP

The experimental results showed that many gas bubbles were produced during laser joining of PET to Ti when the laser power was higher than 45 W. It is believed that when the temperature of the molten plastic is higher than the pyrolysis temperature of PET (about 300 ℃), gaseous products are produced.

To demonstrate the effect of bubble movement due to the temperature difference in the molten plastic, the case of laser joining using a power of 55 W (welding speed 4 mm/s, pulsed frequency 20 Hz) was analysed. The temperature profile of the joint was simulated based on the thermal analysis

model presented in section 6.1, using ANSYS. The Fig. 8.12 shows the temperature obtained for Point (A) in Fig. 8.11 (x = 0 mm, y = 12 mm, z = 1 mm) as a function of time. At t = 2.2 s, the temperature of point A reaches 300 ℃, and assumed that a bubble is formed. The temperature of Point A will further increase to above 350 ℃ before starting to decrease at time 3 s. The temperature profile of the joint at t = 2.2 s is shown in Fig. 8.13. The bubble is positioned in a temperature gradient along the welding direction, with temperature on the left higher than that on the right. Based on the analysis presented in sections 8.4.1.2 and 8.4.1.3, the force of evaporation momentum (F_{M1}) is higher than (F_{M2}), and as a result, the bubble will move to the left (Fig. 8.13).

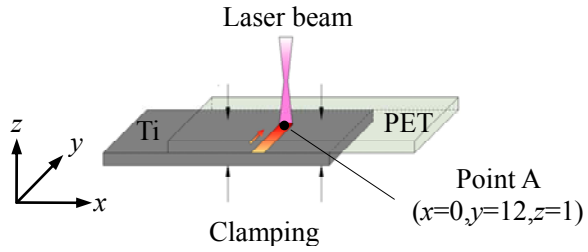

Fig. 8.11 Point A in the weld (x=0 mm, y=12 mm, z=1 mm).

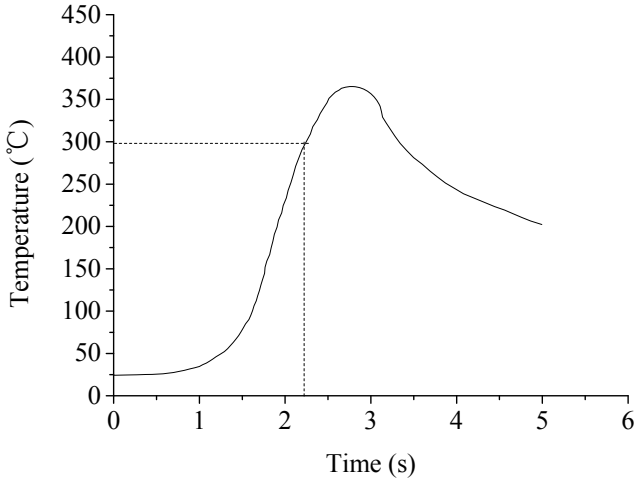

Fig. 8.12 The temperature of Point A in Fig. 8.11 as a function of time.

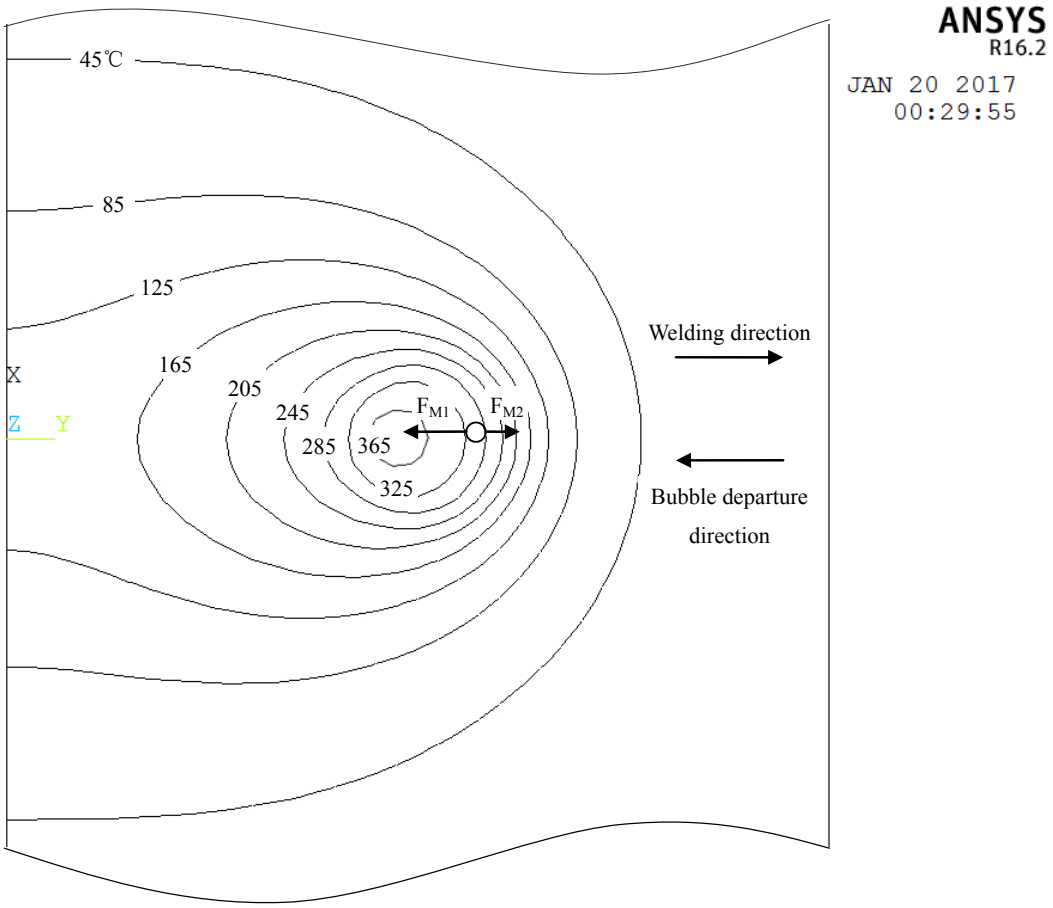

Fig. 8.13 Temperature profile of the joint at t = 2.2 s, also showing is the evaporation momentum forces acting on the bubble.

8.4.2 Ultrasonic vibration induced pressure field

8.4.2.1 Simulation method

A schematic physical model of the finite element analysis of the ultrasonic vibration induced pressure field is shown Fig. 8.14. The edge of the open channel is in line with the centreline of the joint (offset = 0.5 mm). To simplify the model, the roughness of the Ti and PET sheets is neglected. The ultrasonic vibration effect operates on the mode of half of a sinusoidal wave (Fig. 6.6).

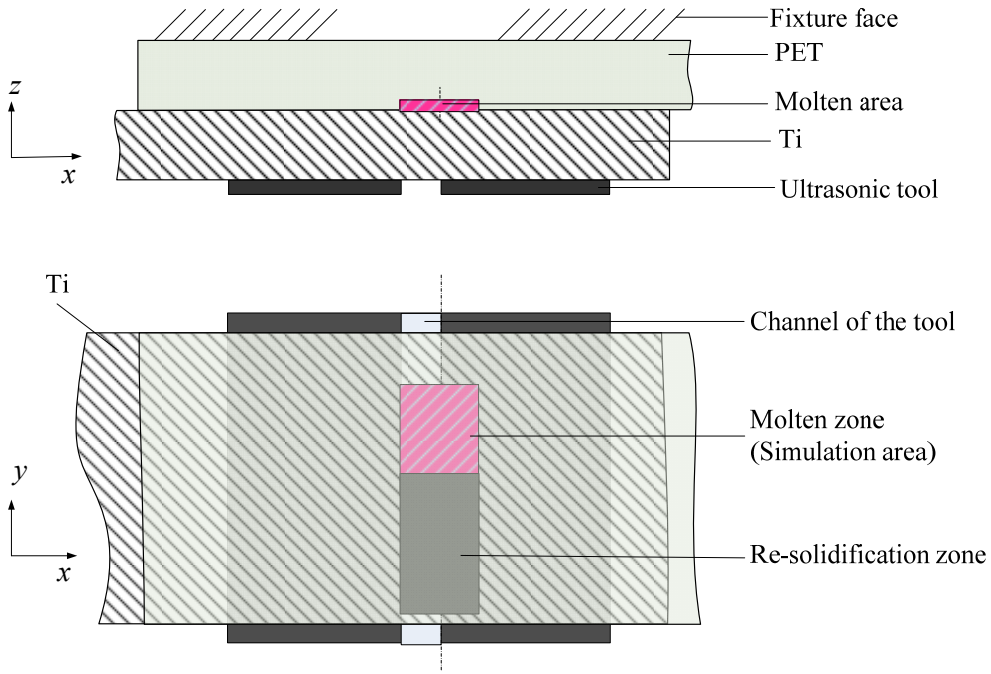

Fig. 8.14 The schematic diagram of the physical model.

The default Pressure Acoustics feature of ANSYS was used for simulating the pressure profile in U-LAMP joining, which models harmonic sound waves in a homogeneous liquid domain, with the sound pressure determined using the Helmholtz equation [149]:

$$\nabla^2 p(\vec{r}) + k_w{}^2 p(\vec{r}) = 0 \tag{8.11}$$

in which, $p = p_0 e^{iwt}$ is the sound pressure, $\vec{r}$ is the spatial variable $\vec{r} = [x, y, z]$, and $k_w = w/u$ represents the wave number (w is the angular frequency and u is the sound velocity).

The relationship between displacement of the workpiece and acoustic pressure is [150]:

$$\frac{\partial p}{\partial n} = -\rho \frac{\partial^2 U_n}{\partial t^2} \tag{8.12}$$

where n is a normal vector to the Ti sheet, ρ is the density of the molten PET, t is the time, $U_n = \xi \sin(wt)$ is the displacement of the Ti sheet in the direction perpendicular to the boundary. In the case of using an open channel transducer tool, the measured vibration amplitude (ξ) of position A was about twice that of position B (Fig. 7.6). The pressure-acoustic module of the finite element commercial software ANSYS was employed to solve Eqns (8.11) and (8.12), and was based on acoustic-piezoelectric coupling frequency domain analysis. The boundary conditions are: (i) U (displacement) = U_0 at the ultrasonic tool/Ti sheet interface, (ii) the top free surface of the quartz plate and the solid PET around the molten PET are fixed constraints, i.e. U = 0, (iii) the vibration velocity u = 0 at the free quartz plate surface. A triangular mesh generation technique has been employed in this simulation. The physical parameters employed in the simulation analysis are listed in Table 3.5.

8.4.2.2 Results and discussion

Figs. 8.15-8.17 display the pressure distribution that occurs in the molten PET in one specific loading cycle (T/16~T/2) in U-LAMP joining when an open channel tool with different amounts of offset are analysed.

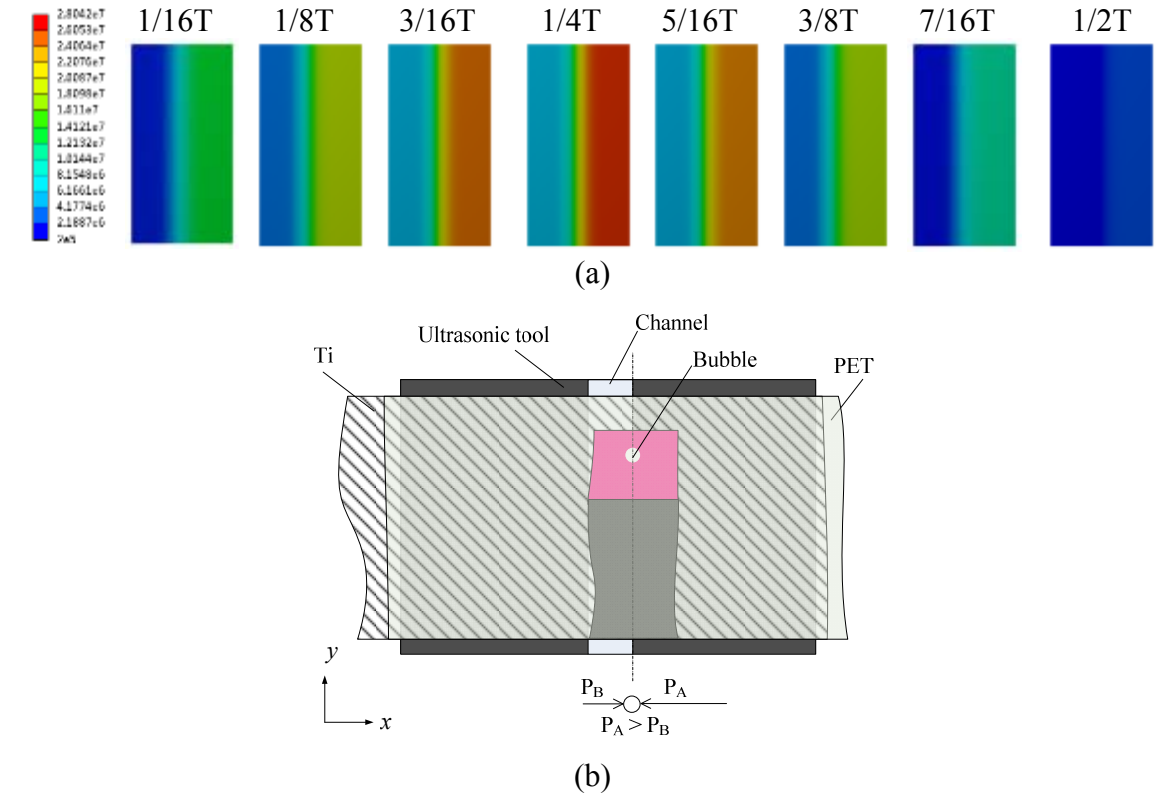

Fig. 8.15 (a) The pressure distribution in a loading cycle (T/16 ~ T/2) with 0.5 mm offset, (b) showing an unbalanced pressure acting on the bubble.

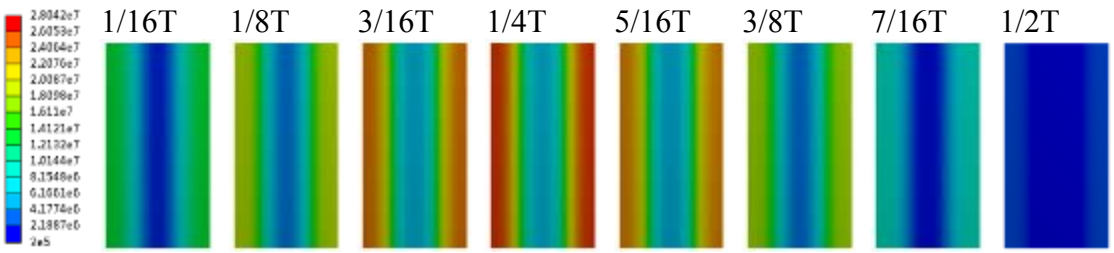

(a)

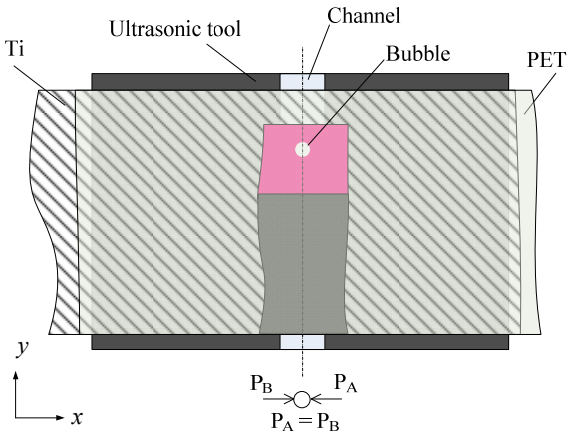

(b)

Fig. 8.16 The pressure distribution in a loading cycle (T/16 ~ T/2) with no offset.

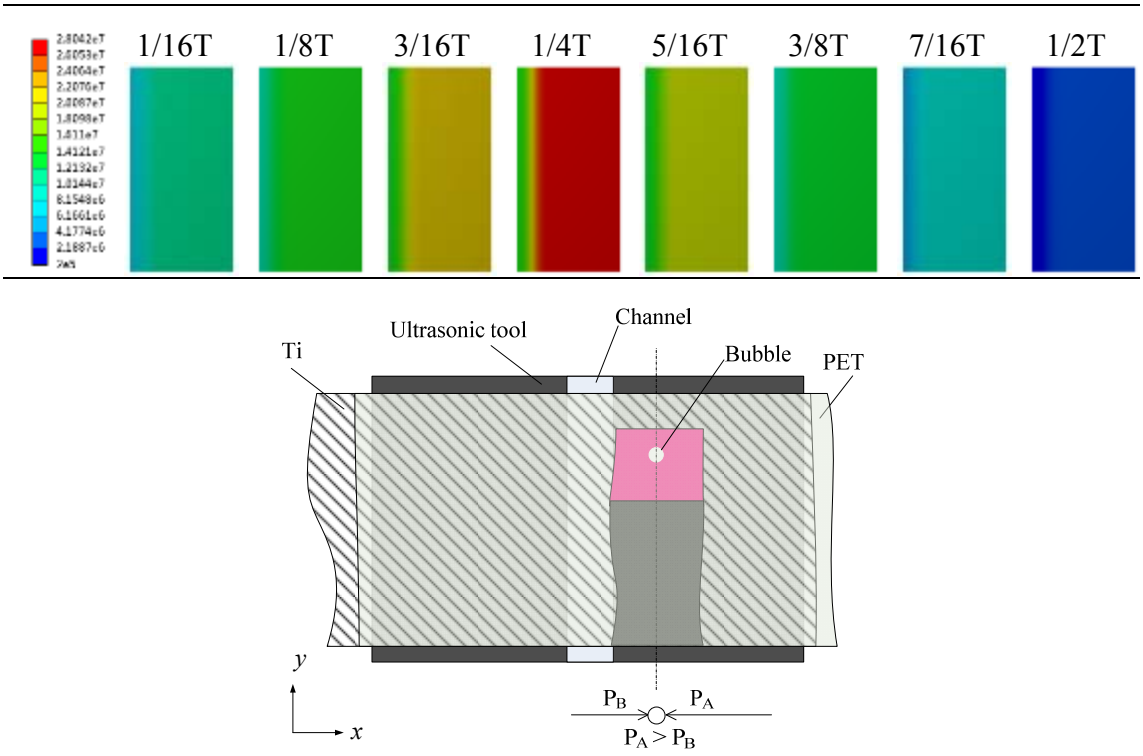

Fig. 8.17 The pressure distribution in a loading cycle (T/16 ~ T/2) with 1.5 mm offset.

Comparing these three situations, a large unbalanced pressure is developed on the bubble along the x-axis, if the edge of the open channel is aligned with the centreline of the joint, i.e. an offset of 0.5 mm (Fig. 8.15). The pressure acting on the right hand wall (P_A) is greater than that on the left hand wall (P_B) of the bubble (Fig. 8.15b). In other words, a net force (F_{pg}) is created as a result of the pressure difference, which forces the bubble to move to one side of the molten zone and can cause the bubble to escape from the PET/Ti interface. In the case where there is no offset (Fig. 8.16) or if the offset is too large (Fig. 8.17), there is not such a large pressure difference around the bubble, therefore, bubbles largely remain stagnant and are not likely to be able to escape from the joined zone.

8.4.3 Verification of bubble movement by high speed camera images

For the case of an open channel transducer tool with an appropriate offset to the weld centreline, the external forces acting on a bubble (including the evaporation momentum force (F_M) caused by temperature difference, and a net force (F_{pg}) caused by pressure difference and drag forces (F_{dx} and F_{dy}) dictate the direction of the bubble movement (Fig. 8.18a), the resultant force (F_r) acting on the bubble can be considered as the combined effects of F_M and F_{pg}. Therefore, based on the above analyses of the temperature and ultrasonic vibration induced pressure effects, the trajectory of bubbles in the molten PET should follow the path shown in Fig. 8.18(b), and have the chance to escape through the PET/Ti interface.

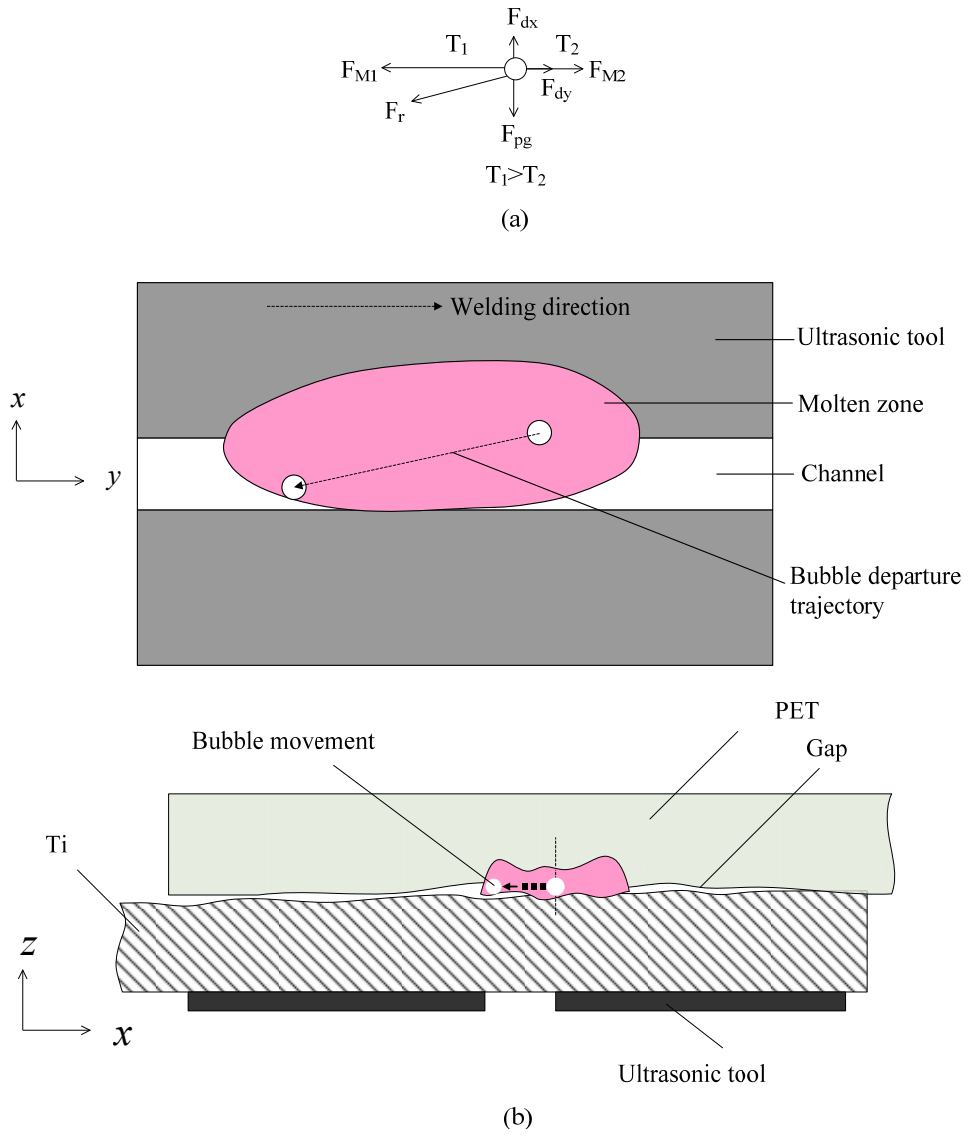

Fig. 8.18 (a) the various external forces acting on a bubble; (b) the predicted trajectory of a bubble in the molten PET (offset = 0.5 mm).

In order to determine the movement track of the bubbles, a high-speed camera (Phantom, Miro LAB320) operates at 23,000 frames/sec was employed to capture the image of the entire bonded area (Fig. 8.19). Fig. 8.20 shows the images of the positions of a bubble captured by the high-speed camera in a time series in the molten PET. The trajectory is depicted in Fig. 8.21, which matches with the predicted direction illustrated in Fig. 8.18(b).

The theoretical analyses of the trajectory of the bubbles under the influence of vibration induced pressure field and the thermal field in laser joining, and by high-speed camera images are in good agreement with the experimental results of U-LAMP (Figs. 8.5-8.7) is that ultrasonic vibration can drive bubbles out of the joined zone during the laser joining of PET to Ti. Based on the images captured by the high-speed camera, it was found that the time for a bubble to escape from the molten pool is very short, and it will not experience the next laser pulse. Therefore, there is no need to consider the overlap effect on bubble motion.

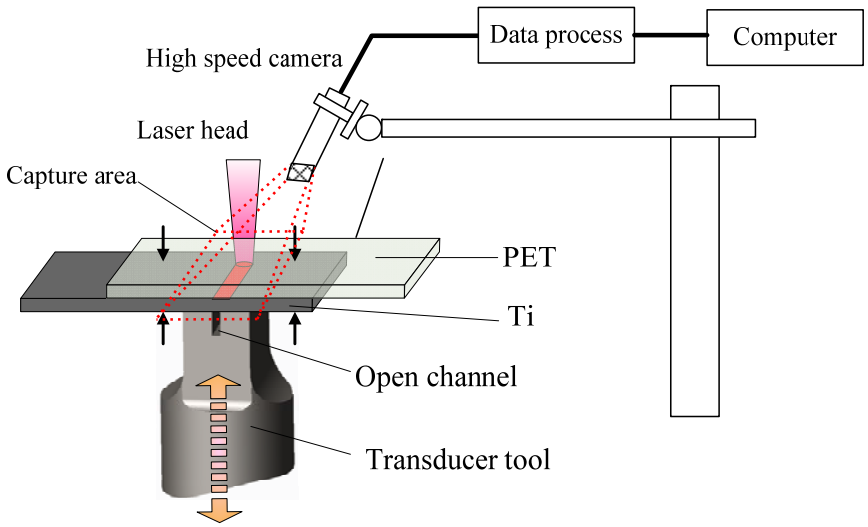

Fig. 8.19 A schematic diagram showing the set-up of the high-speed camera.

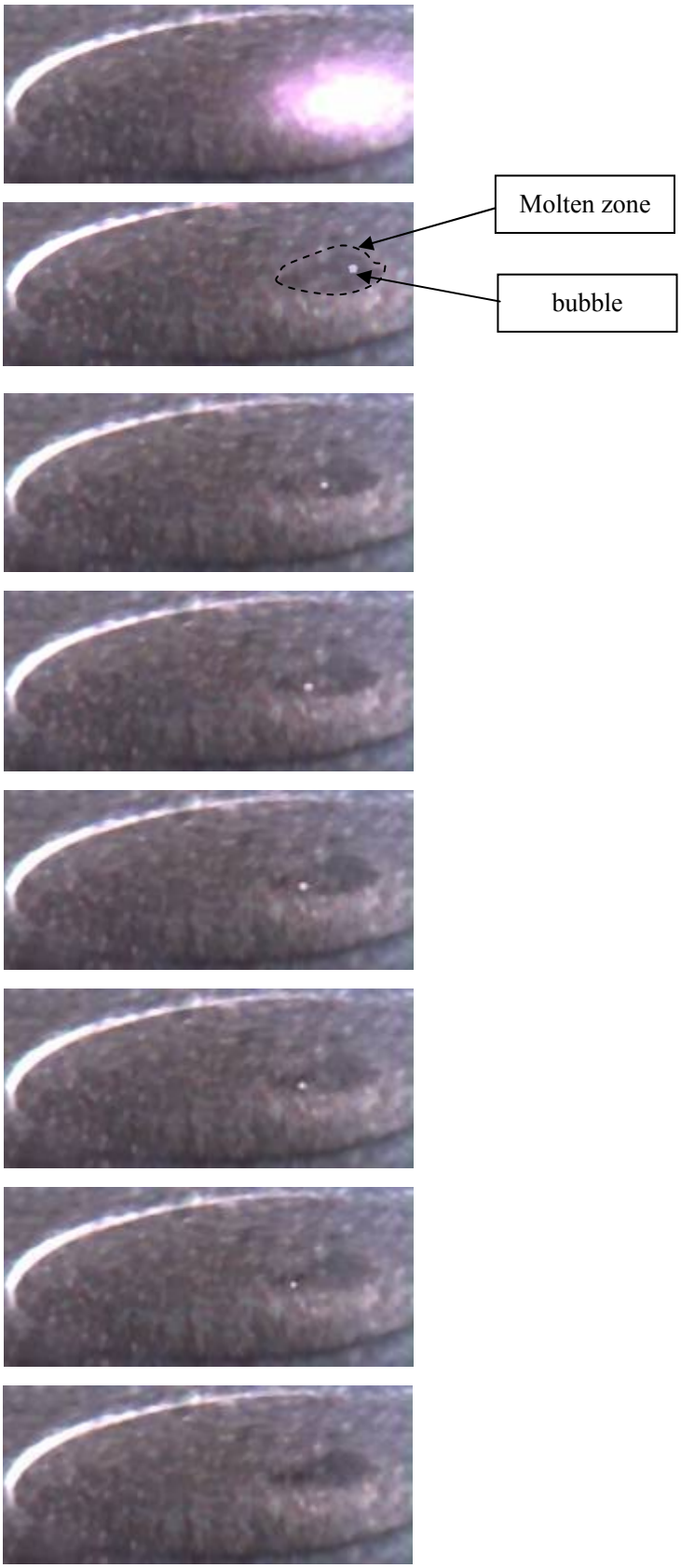

Fig. 8.20 High speed camera images showing positions of a bubble in a time series in molten PET. (joining conditions: laser power 55 W, laser speed 4 mm/s, pulsed frequency 20 Hz, vibration amplitude=4 μm)

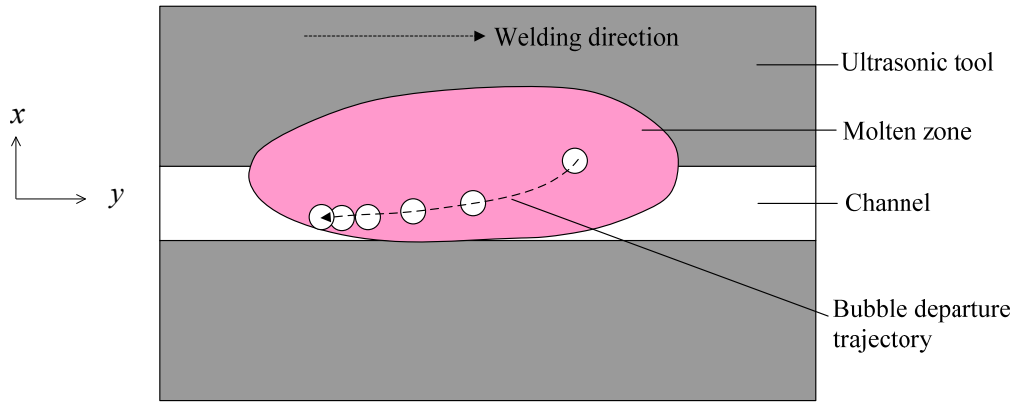

Fig. 8.21 An illustration of the trajectory of a bubble in molten PET.

8.5 Shear test results and failure analysis of joints

Fig. 8.22a shows the effect of laser power on the failure load for both LAMP and U-LAMP specimens. The area of bonded surface of the joint was measured before the shear test, and the area increased as laser power increased (Fig. 8.23). To better reflect joint performance, Fig. 8.22a was re-plotted in terms of failure stress (Fig. 8.22b). Typical fracture appearances of the LAMP and U-LAMP specimens are shown in Fig. 8.24. The former fractured at the metal-plastic interface and resulted in separation of the metal and plastic parts, while the latter fractured in the parent plastic part. It is clear that the fracture stress of the U-LAMP specimen is significantly higher than that of the LAMP specimens (at least four times higher) and their fracture mechanisms were different. This is considered to be caused by a reduction of the bubbles and a stronger metal-plastic interface obtained for the U-LAMP specimens. This strong interface of the U-LAMP specimens is supported by a higher level of Ti-C bond intensity and a greater depth of the reaction zone of the Ti-C bond measured across the interface. The results obtained for some LAMP and

U-LAMP specimens are given in Fig. 8.25. The XPS spectra obtained for the LAMP and U-LAMP specimens are given in Appendix A and Appendix B; the analysing technique for determining the reaction depth was the same as described in Section 4.3.

For the LAMP specimens, the failure stress initially increased with increase in laser power and reached a maximum at 55 W. It then decreased when the power was increased further (Fig. 8.22b). The level of laser power is considered to have a direct effect on the formation of the chemical bonds at the joint interface, as well as on the polymer degradation. Too low a laser power will reduce chemical bonding between the metal and plastic parts, whereas, too high laser power will result in the formation of many bubbles, as well as causing degradation of the polymer, thus resulting in a relatively weak joint. Fig. 8.26 reveals that the final fracture area of LAMP_55W was much larger than that of a LAMP specimen produced using lower laser power (LAMP_30W) (cf. Fig. 8.26a & Fig. 8.27a), with a high degree of plastic drawing (cf. Fig. 8.26b & Fig. 8.27b). This leads to the conclusion that bubble-induced pressure acting on the molten plastic does help to form a stronger bond at the interface. However, if too many bubbles are formed when high laser powers are used, the counter-effect of the bubbles (themselves defects) becomes significant.

Examining the results of the U-LAMP specimens, the failure stress did not change significantly within the range of laser power used (i.e. 30 W to 75 W), except that when the laser power was above 55 W, where the fracture strength slightly decreased. This indicates that when the laser-bonded joint is largely free from porosity, increasing the laser power will not result in higher

strength, and if the power is too high, it may even cause a reduction in strength due to damage made to the plastic. Fig. 8.28 shows that fracture of the U-LAMP specimens occurred in the parent plastic material (specimens U-LAMP_30W and U-LAMP_55W), and the final bonded area between the PET and the Ti sheets was larger for the latter. For U-LAMP_30W, a relatively large part of the originally bonded surface had already debonded. This indicates that, although the overall interfacial bond strength of U-LAMP_55W was higher than that of U-LAMP_30 W, especially in regions further away from the centre of the weld line, a high interfacial bond still occurs near the joint centreline of U-LAMP_30W. This is reasonable because the laser output has a Gaussian distribution and the highest power is experienced at the centre of the weld. This means that towards the end of the tensile shear test, the remaining bonded surface along the centreline has sufficient interfacial strength to hold the PET and Ti parts together and eventually the fracture occurrs in the plastic part. This is considered to be the reason why the failure stress did not change considerably with laser power.

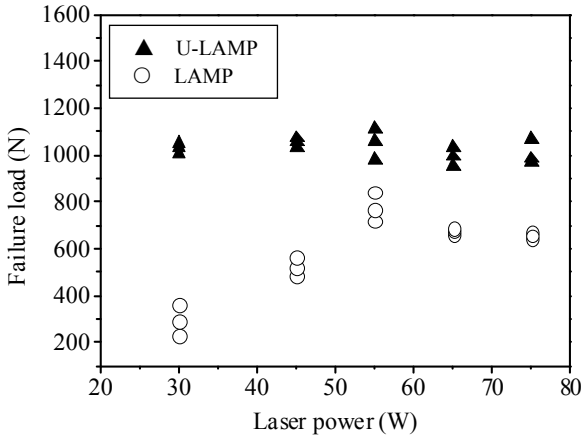

(a)

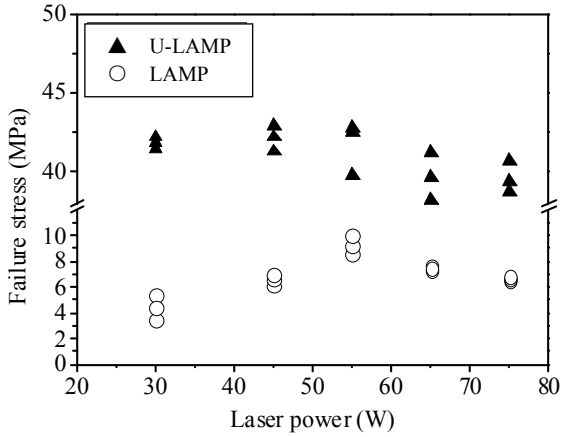

(b)

Fig. 8.22 The effects of laser power on (a) failure load, (b) failure stress.

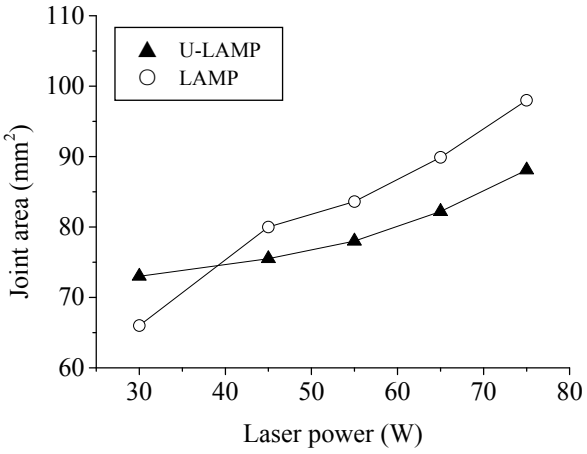

Fig. 8.23 The relationship between laser power and bonded area.

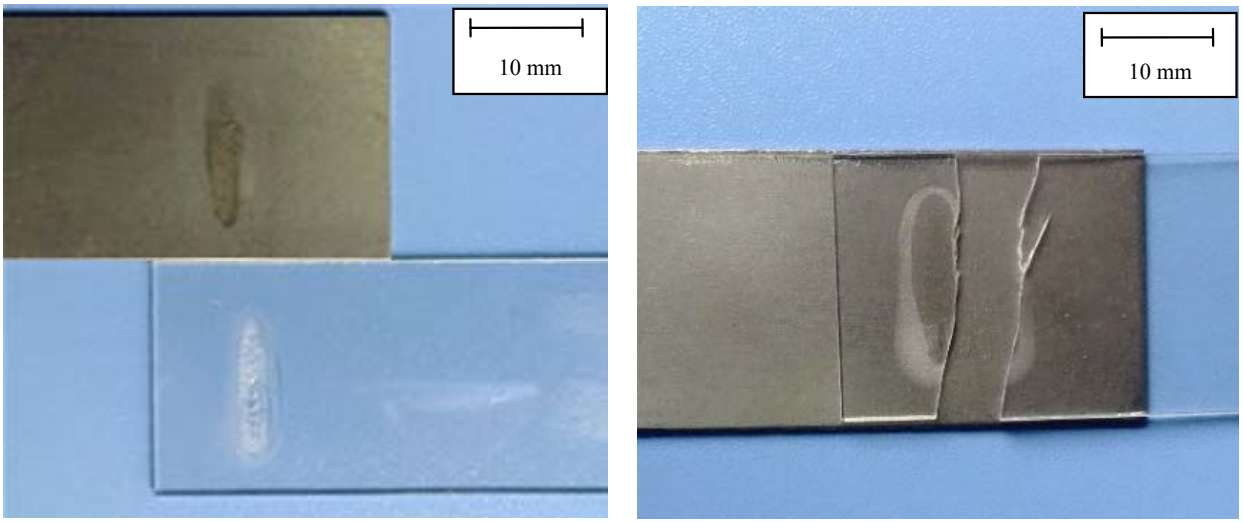

(a) (b)

Fig. 8.24 Failure appearance of (a) a LAMP specimen (55 W), (b) a U-LAMP specimen (55 W).

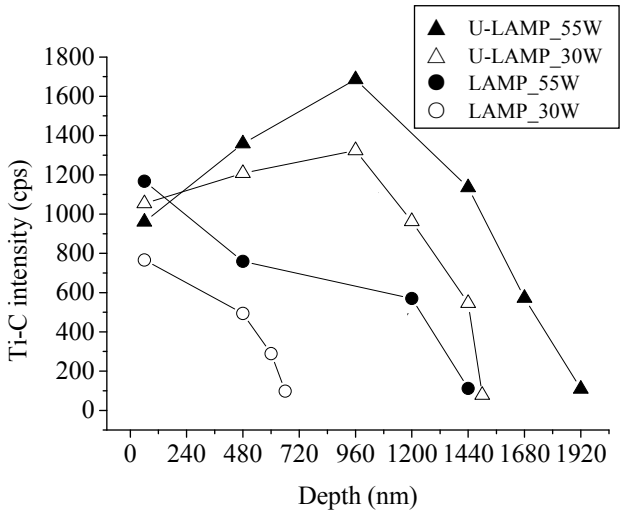

Fig. 8.25 Ti-C intensity measured at different sputtering depths for some LAMP and U-LAMP specimens.

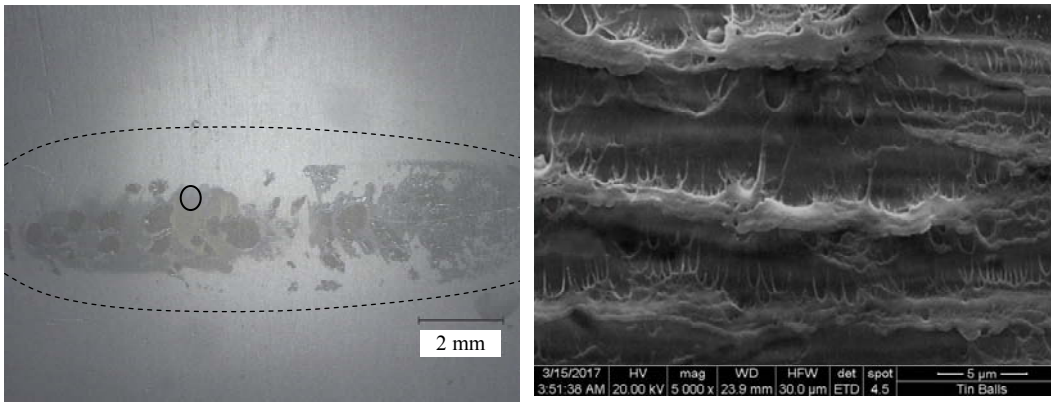

(a) (b)

Fig. 8.26 Fracture surface of LAMP_55W, photos taken from the Ti side (a) optical micrograph (the dotted line indicates the originally bonded boundary), (b) SEM micrograph of point A.

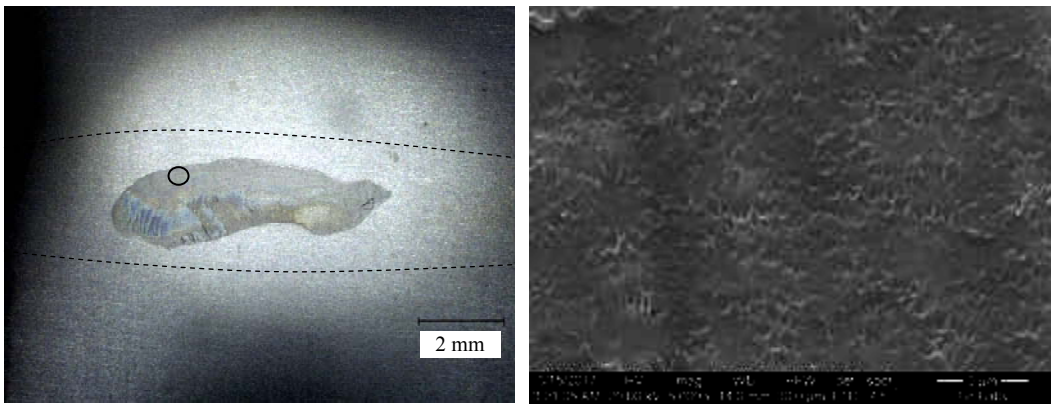

(a) (b)

Fig. 8.27 Fracture surface of LAMP_30W, photos taken from the Ti side (a) optical micrograph (the dotted line indicates the originally bonded boundary), (b) SEM micrograph of point A.

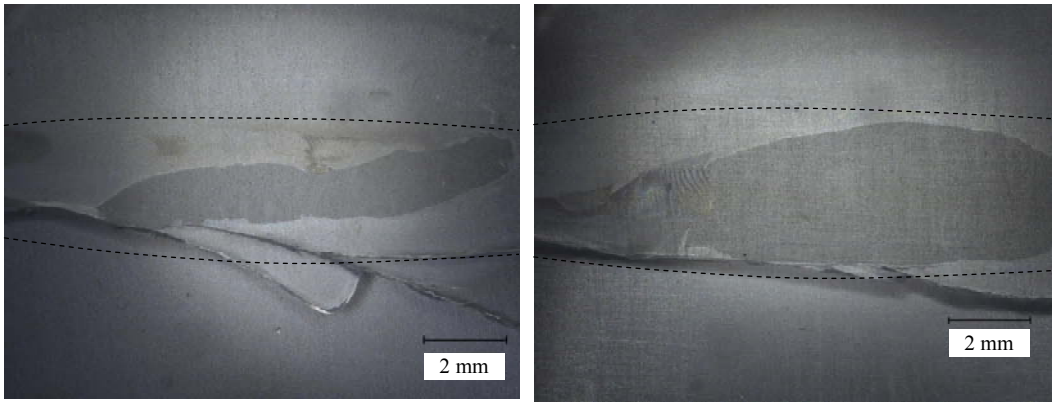

(a) (b)

Fig. 8.28 Fracture occurred in the parent plastic material (a) U-LAMP_30W, (b) U-LAMP_55W specimens; (the dotted line indicates the originally bonded boundary).

The effects of laser travel speed and frequency on failure load are similar, i.e. an increase followed by a decrease after reaching a maximum (Figs. 8.29, 8.30). This is somewhat expected because travel speed and frequency in essence control the total amount of energy input into the joint. It is considered that too high a travel speed or too low a pulse frequency results in low laser energy input and this weakens the chemical bonding activity between the metal and plastic parts. On the other hand, too low a travel speed or too high a pulse frequency results in high laser energy input and may cause degradation of the polymer, thus resulting in a drop in joint strength.

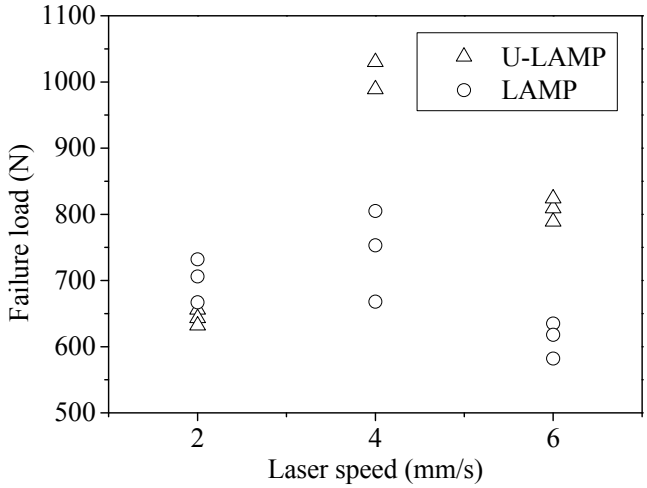

Fig. 8.29 The effects of laser travel speed on tensile shear load and fracture mode (laser pulse frequency 20 Hz, power 55 W).

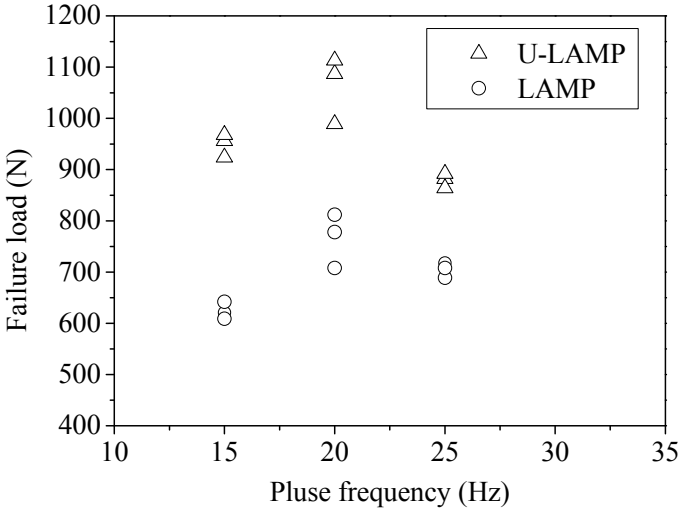

Fig. 8.30 The effects of laser pulse frequency on tensile shear load and fracture mode (laser power 55 W, travel speed 4 mm/s).

8.6 Chapter summary

An open channel transducer tool was designed for the U-LAMP joining process with the aim of driving the laser-induced bubbles out of the joined zone. In addition, the effects of ultrasonic vibration on joint appearance, chemical bonds across the joint interface and the failure load of the joint were also

studied. The removal mechanism of bubbles from the molten plastic zone was analysed based on the pressure and temperature profiles present in U-LAMP, using the finite element method. The major findings are summarised as follows.

(i) For the conventional LAMP joining process, the formation of bubbles in the joint zone is inevitable. On the other hand, with the new U-LAMP process and using the offset technique, the amount of bubbles was significantly reduced and in most cases no sizable bubbles could be observed under an optical microscope.

(ii) The combined effect of the pressure and thermal fields in the joint has an important impact on the trajectory of the bubbles, and can drive bubbles out of the joint zone. The experimental results of U-LAMP were supported by the theoretical predictions and the high speed camera images.

(iii) Ultrasonic vibration causes a more intimate contact between molten PET and the Ti metal which promotes chemical reactions between them.

(iv) Comparing the fracture load of the LAMP and U-LAMP specimens, the failure load of the latter was significantly higher than that of the LAMP specimen. With regard to the failure mode, the LAMP specimens mainly fractured at the metal-plastic interface, while for the U-LAMP specimens, the fractures generally occurred in the plastic part.

Chapter 9

Fatigue Properties

9.1 Introduction

The objective of the study is to characterise and to compare the fatigue performance, in terms of S-N curves, of the lap joined specimens produced by LAMP and U-LAMP. Fatigue tests were conducted on both the LAMP and U-LAMP specimens joined by using laser powers of 30 W and 55 W. The condition of 55 W was chosen because this condition yielded the maximum shear failure load, while for the case of 30 W, the LAMP and U-LAMP specimens are largely free from porosity. Figs. 5.1 and 8.5 show the joints of these four types of specimens for ease of reference. Fatigue test was conducted at a constant mean load of 200 N. The S-N results obtained were correlated with observations derived from light and scanning electron microscopy (SEM) studies of the joints after fatigue testing.

9.2 Comparison of fatigue endurance

The fatigue endurance of the specimens (LAMP_30W, LAMP_55W，U-LAMP_30W, U-LAMP_55W) are summarised in Table 9.1. The data are presented in the form of S-N curves in Fig. 9.1. The results show that the fatigue resistance of the specimens follows the sequence of U-LAMP_55W > U-LAMP_30W > LAMP_55W > LAMP_30W. In the absence of porosity in the U-LAMP joints, increasing the laser power from 30 W to 55 W results in a

longer fatigue life. For the LAMP specimens, although LAMP_55W contains porosity, its fatigue resistance is still better than that of LAMP_30W which is largely free from porosity. This indicates that a stronger interface, in terms of chemical bonds intensities, will give rise to a longer fatigue life. Comparing the lives of U-LAMP_30W and LAMP_30W (both are virtually porosity free) also shows that the former, which has higher chemical bond intensity at the PET/Ti interface than the latter, exhibits superior resistance to fatigue. An improvement in fatigue life of two orders of magnitude was obtained. Comparing the results of U-LAMP_55W and LAMP_55W shows that with a similar chemical bonding condition, an improvement of fatigue life of one order of magnitude was obtained if most of the porosity is eliminated. The following section presents some observations of the study of the LAMP and U-LAMP joints after fatigue testing, explaining the differences in fatigue life between them.

Table 9.1 Fatigue endurance of the LAMP and U-LAMP specimens

Samples	Specimen designation	Test_1 (cycles)	Test_2 (cycles)	Test_3 (cycles)	Test_4 (cycles)	Test_5 (cycles)
LAMP_30W	Specimen A	3078	2856	2538	2246	1982
LAMP_55W	Specimen B	186542	154896	102886	98652	46326
U-LAMP_30W	Specimen C	>600000	567894	511836	386604	268956
U-LAMP_55W	Specimen D	2177962	>600000	>600000	586184	548764

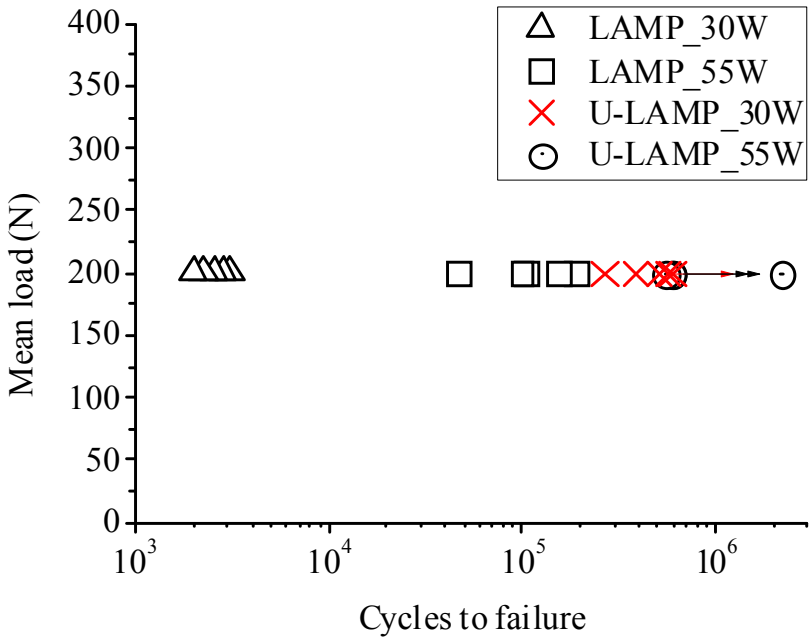

Fig. 9.1 S–N curves of the LAMP and U-LAMP specimens.

9.3 Fatigue behaviour

For both the LAMP and U-LAMP specimens, fatigue cracks were initiated at the outside periphery and propagated towards the centre of the bonded zone. A typical example showing this behaviour is given in Fig. 9.2. The crack started at the periphery due to the stress concentration along the bonding boundary, and the chemical bond there is relatively weak. It is worth remembering that the intensity of the chemical bonds decreases from a maximum at the centre of the weld line to a minimum at the periphery because of the Gaussian distribution of laser energy, where the centre receives the highest laser power.

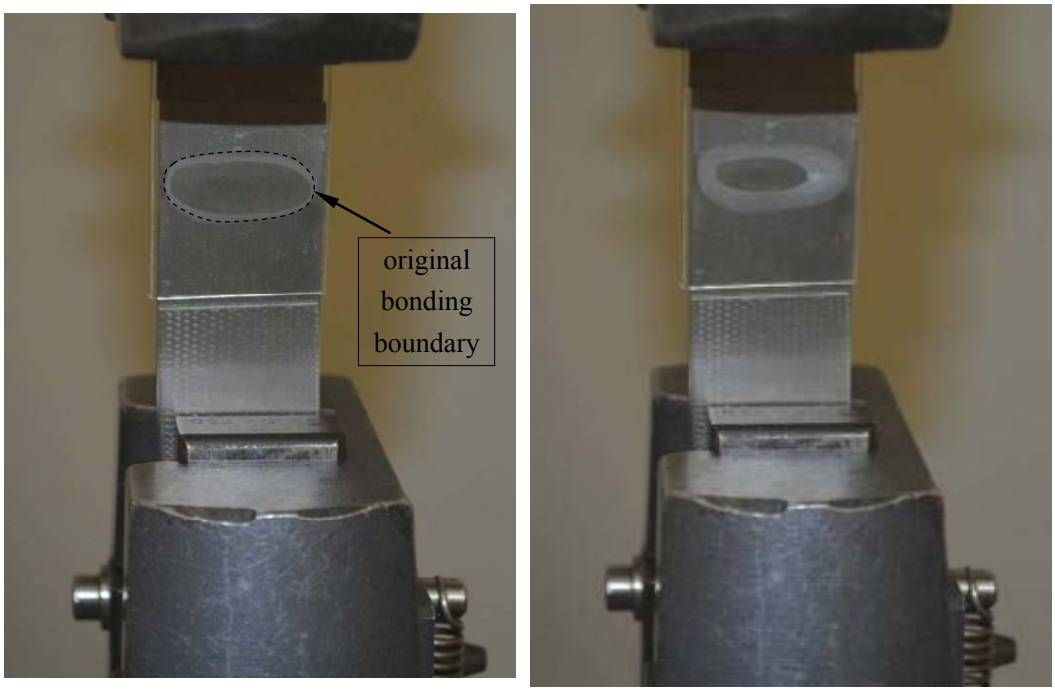

(a) (b)

Fig. 9.2 The joined zone of a U-LAMP specimen (Specimen D) after testing for (a) 1000 cycles, and (b) 6 x 10^5 cycles. (the dotted line outlines the original bonding boundary).

For both the LAMP and U-LAMP specimens, although fatigue cracks all started at the periphery of the bonded zone, a close examination of their fracture surfaces (the Ti part) shows that their crack propagation behaviours are different. Fig. 9.3(b) shows the fracture surface of a LAMP_55 W specimen; the dotted line outlines the original periphery of the bonded area. The joint appearance before testing is shown in Fig. 9.3(a). A fairly shiny surface (marked A in Fig. 9.3b) can be observed in regions relatively far away from the centreline region. In locations where there are bubbles (such as that marked B in Fig. 9.3b), a tinted surface can be observed.

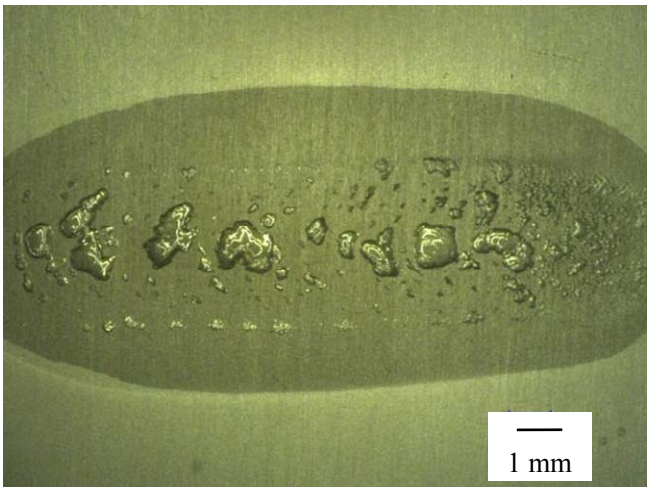

(a)

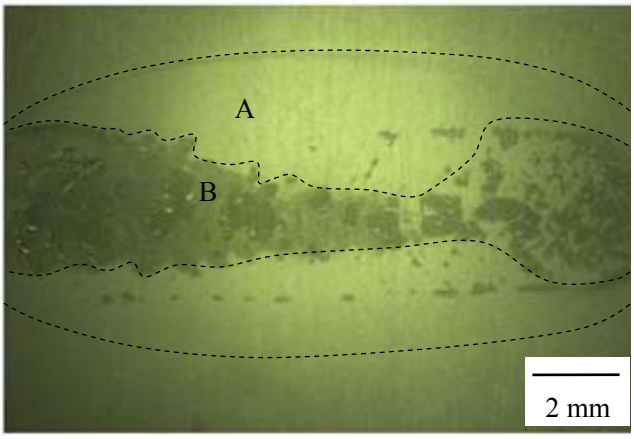

(b)

Fig. 9.3 (a) joint appearance of Specimen B before fatigue testing, (b) fracture surface of the Ti side.

The SEM examination of this fracture surface confirms that Zone A is basically the bare surface of the Ti sheet with mechanical grinding marks clearly seen on the surface, also only a small amount of PET adheres to the surface (Fig. 9.4a). The lack of strong chemical bonding between PET and Ti is evidenced from the XPS results of Zone A. Figs. 9.5 and 9.6 show the high resolution C1s and Ti2ps XPS spectra obtained for this region, respectively. The results reveal that the chemical composition and the chemical state of this region are similar to those of the original Ti sheet, i.e. only TiO_2 covered the surface. This means that

for a Zone A type of area, the bonding is very weak in that the fatigue crack actually debonded the Ti/PET interface. It is considered that the fatigue crack advances at a fast pace in this region. This type of crack propagation mode was also found to be dominant in Specimen A (LAMP_30W) (Fig. 9.7), and this explains why Specimen A has a low fatigue life.

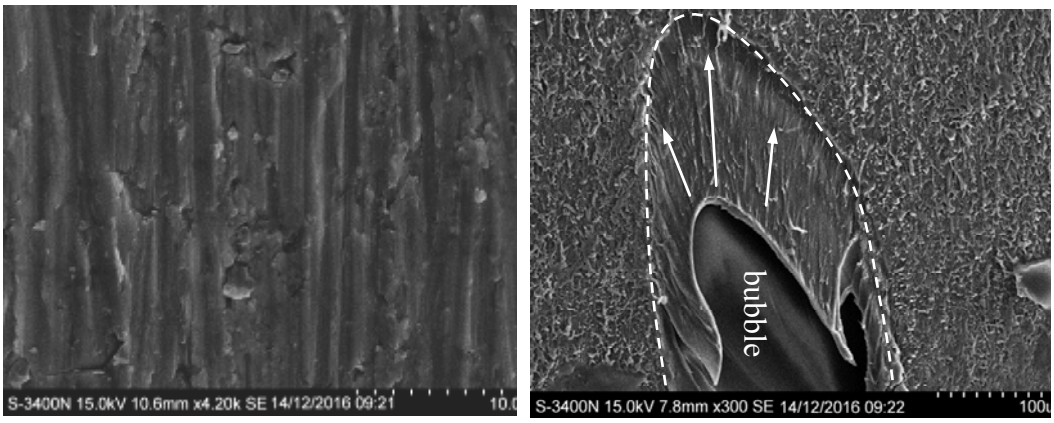

(a) (b)

Fig. 9.4 SEM micrographs of the fracture surface of Specimen B: (a) Zone A, and (b) Zone B (arrows pointing to possible fatigue crack growth directions) of Fig. 9.3(b).

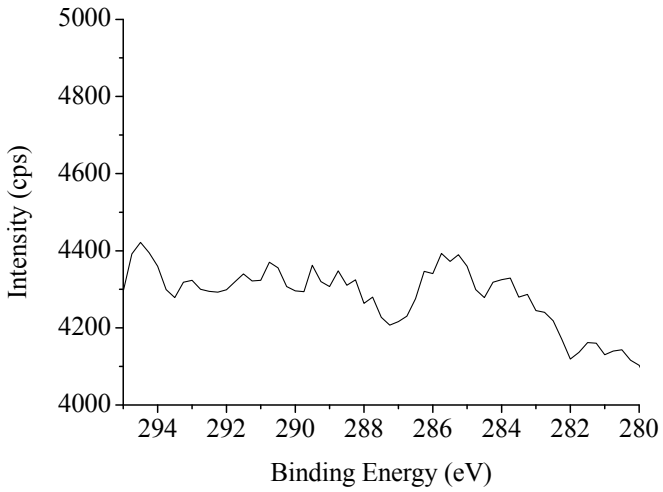

Fig. 9.5 High resolution C1s XPS spectrum taken from Zone A of Fig. 9.3(a).

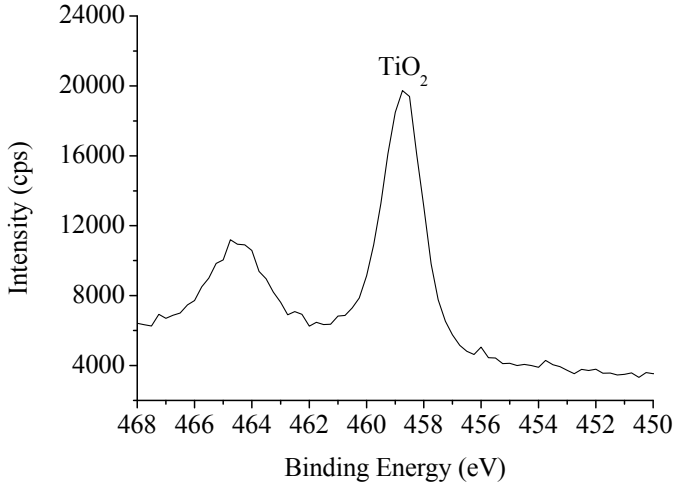

Fig. 9.6 High resolution Ti2ps XPS spectrum taken from Zone A in Fig. 9.3(b).

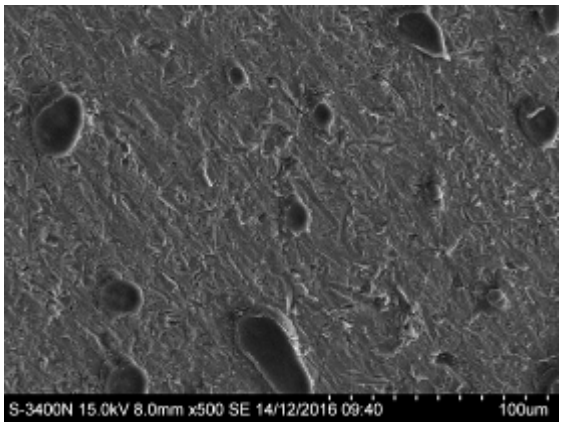

Fig. 9.7 Fracture surface of Specimen A, most areas resemble that of Zone A of Specimen B, and are bare metal surfaces.

In areas where there are bubbles, polymer residuals were found on the surface with signs of fibrillar deformation of the plastic material (Fig. 9.4b). Fig. 9.8 shows the high resolution C1s XPS spectra taken from Zone B without ion-milling and after ion-milling to a depth of 480 nm. The presence of a C-C bond before ion-milling supports the idea of PET adhering to the Ti surface, and

the Ti-C bond found at the depth of 480 nm reveals that the PET/Ti interface was bonded chemically. Fig. 9.4(b) also shows that at the edge of the bubble, the crack propagated in a relatively brittle manner. This suggests that, due to the stress concentration effect, a relatively fast propagating pace of the crack occurred at bubbles locations, shortening the fatigue life of the joint. Although bubbles in the joint can act as crack deflectors and could possibly reduce the effective stress intensity at the crack fronts, such an effect is considered to be small in this case because the bubbles are lying more or less in the same horizontal plane and large crack deviation is not expected. It is likely that the fatigue crack propagated in a fast manner by going through the bubbles. The fatigue crack propagation path in Specimen B is proposed and illustrated in Fig. 9.9.

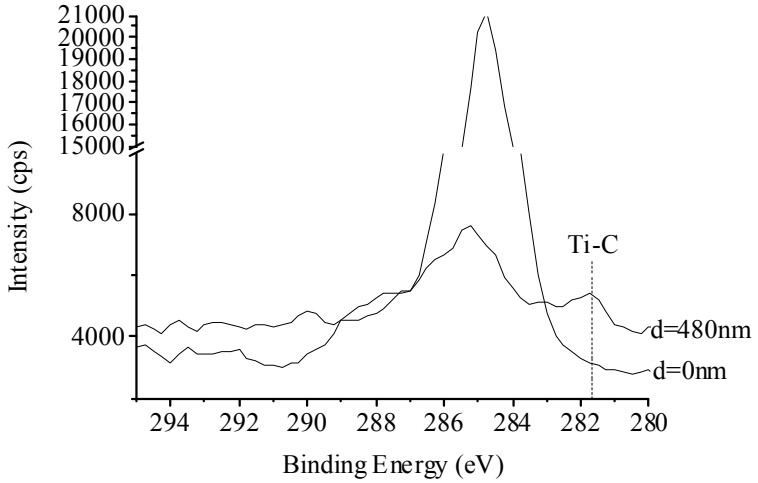

Fig. 9.8 High resolution C1s XPS spectra taken from Zone B, without ion-milling (d=0 nm) and after ion-milling to a depth of 480 nm.

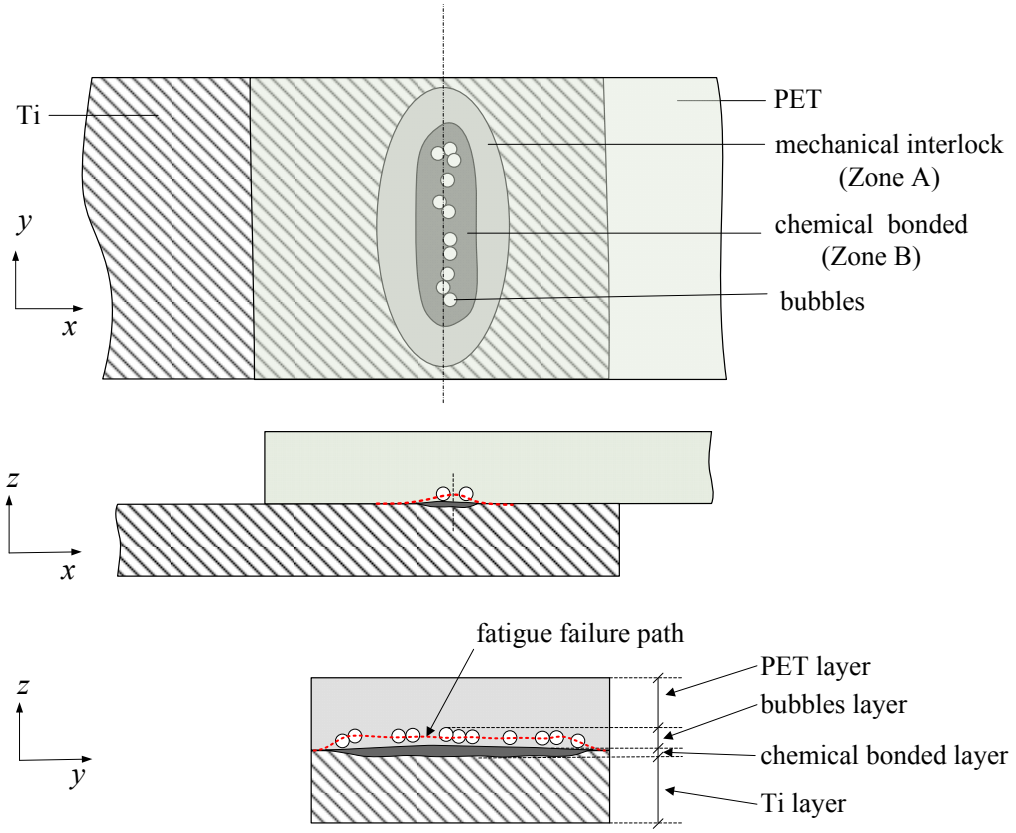

Fig. 9.9 Proposed fatigue crack propagation path in regions where there are bubbles (Specimen B) (not to scale).

For the U-LAMP_55W specimen, which is free from observable bubbles (Fig. 9.10a), fatigue cracks also started at the periphery of the bonded area. The fracture surface can be broadly divided into two regions (Fig. 9.10b), Zone A and Zone B. Zone A is a relatively flat region with some residuals of PET adhering to the Ti surface (Fig. 9.11a). It is considered that the PET/Ti interface at some spots in this region is chemically bonded. This is supported by the high resolution C1s and Ti2ps XPS spectra taken from Zone A where chemical bonds of Ti-C, Ti-O and Ti_2O_3 were detected (Figs. 9.12 and 9.13). Compared to the situation of Zone A of the LAMP_55W specimen, the stronger interface of the U-LAMP_55W specimen should increase the fatigue resistance

of the joint. When the crack advances to Zone B, it appears that the fatigue growth mechanism changes, the cracks propagate in the plastic material and "beachmarks" are observed on the fracture surface (Fig. 9.10b). In between the beachmarks, discontinuous growth bands are found (Fig. 9.11b). These bands resemble those of the striations observed in metal fatigue, but given the relatively large spacing between two adjacent bands, it is unlikely that the spacing represents the local fatigue crack growth (i.e. crack extension per cycle). Some areas in Zone B also exhibit a kind of ductile fatigue crack growth (Fig. 9.11c), and the crack growth rate in these regions should be low. It is considered that without the weakening effect of bubbles, fatigue crack growth mainly follows a path in the plastic material (Fig. 9.14), and this is a relatively slow process compared to that of the propagation mechanism of Specimen B (Fig. 9.9). The fatigue crack growth mechanism of Specimen C (U-LAMP_30W) (Fig. 9.15) is found to be similar to that of Specimen D (U-LAMP_55W) (Fig. 9.11b), i.e. a mixed brittle and ductile growth mechanism. The slightly better fatigue performance of the latter is considered to be due to a stronger bonded interface.

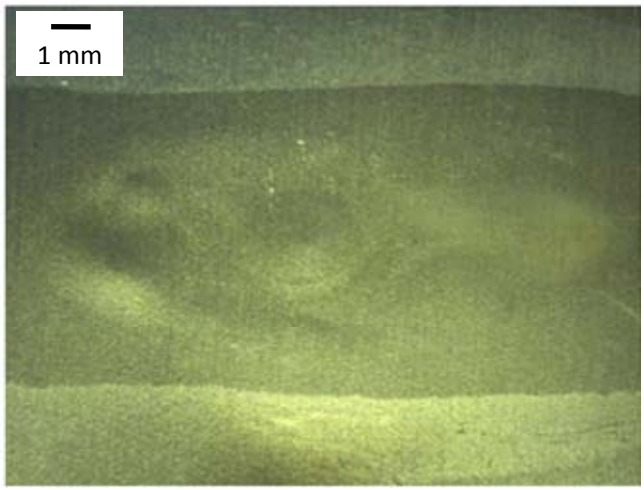

(a)

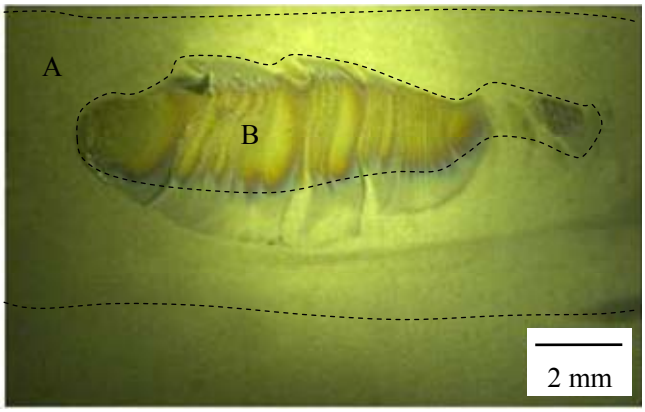

(b)

Fig. 9.10 (a) Joint appearance of specimen D; (b) optical micrograph of the fracture surface taken from the Ti side.

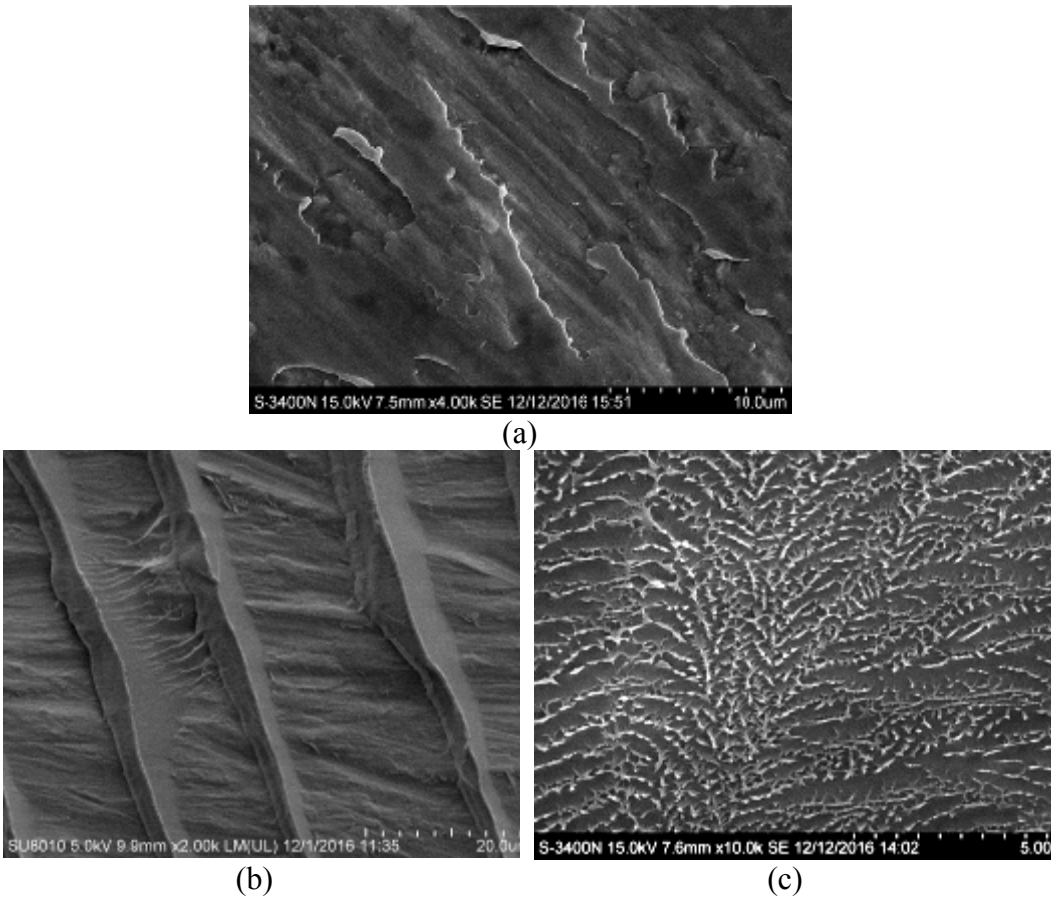

Fig. 9.11 SEM fractographs of Specimen D: (a) Zone A with some residuals of PET; (b) Zone B showing brittle type of "striations", (c) Zone B showing ductile fracture.

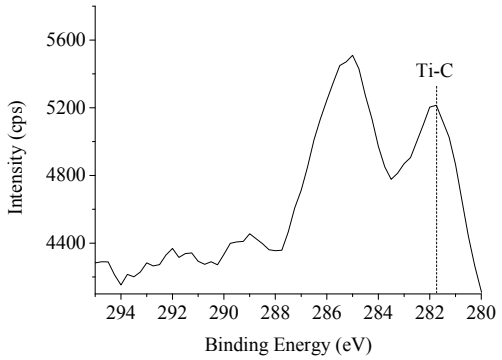

Fig. 9.12 High resolution C1s XPS spectra taken from Zone A of Fig. 9.10(b).

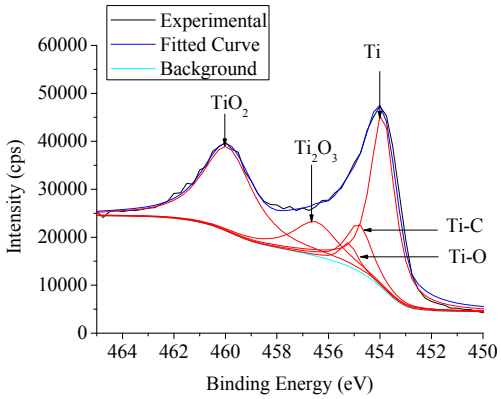

Fig. 9.13 High resolution Ti2ps XPS spectra taken from Zone A of Fig. 9.10(b).

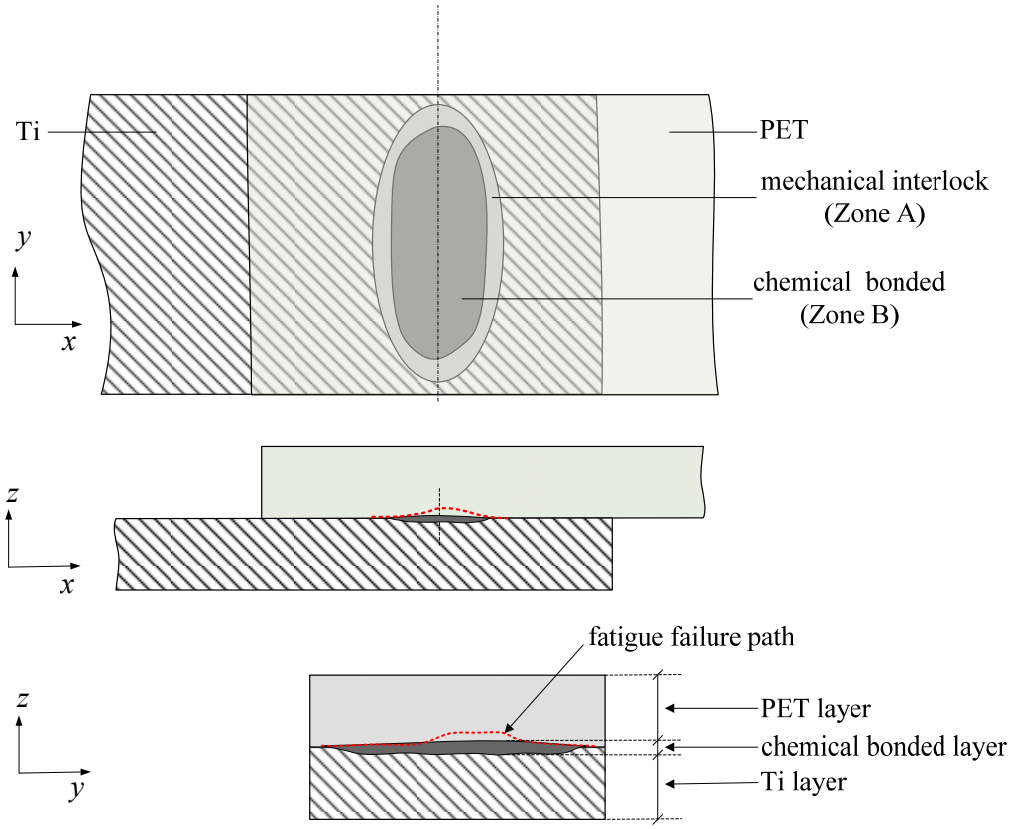

Fig. 9.14 Proposed fatigue crack path in Specimen D (not to scale).

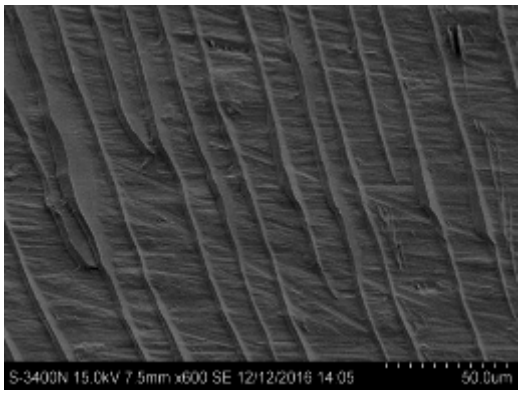

(a)

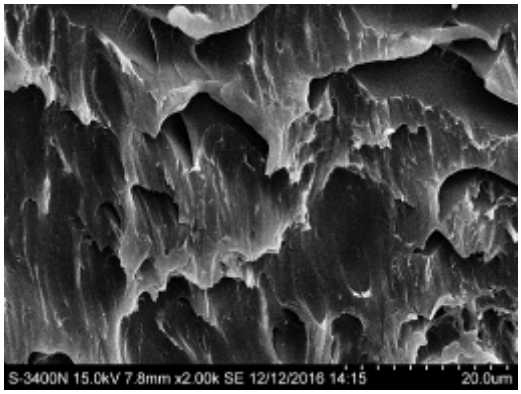

(b)

Fig. 9.15 Fracture features of Specimen C are similar to those of Specimen D: (a) brittle type of "striations", (b) ductile fracture.

9.4 Chapter summary

The fatigue behaviour of the LAMP and U-LAMP joined specimens have been studied. The major observations are summarised follows:

(i) The fatigue performance, in terms of fatigue life, of the U-LAMP specimens was always better than that of the LAMP specimens.

(ii) For all the U-LAMP and LAMP specimens, the fatigue crack started from

the outside boundary of the bonded zone and advanced towards the central area of the joint.

(iii) For the LAMP specimens, a relatively large portion of the fracture surface exhibited a flat region due to weak interfacial bonding. This led to fast fatigue crack growth.

(iv) The bubbles present in the LAMP specimens act as stress raisers and reduce the fatigue life of the joint.

(v) For the U-LAMP specimens, a large proportion of the crack propagation life takes place in the plastic material and this gives rise to a high fatigue crack growth resistance.

Chapter 10

Conclusions

A new laser joining technology, namely ultrasound-aided laser joining (U-LAMP), has been developed to bond plastics to metals. The four objectives set out for this research study have been accomplished. They are:

(i) to design an ultrasonic system for the U-LAMP process that can resolve the bubble problem which is inherent in the conventional LAMP process;

(ii) to analyse and model the acoustic field in relation to the dynamic movement of bubbles in the joint;

(iii) to understand the joining mechanisms of metals to plastics under the combined actions of a laser and ultrasound;

(iv) to improve the mechanical properties of laser fabricated metal-plastic joints with ultrasound aid.

The major findings of this research study are summarised as follows:

A. Conventional laser joining metal-to-plastic (LAMP)

(i) Laser energy has a significant effect on the amount and distribution of bubbles. A somewhat discrete distribution of bubbles was obtained when a relatively low laser energy was used, which in this study was 45 W. When the energy was raised to 60 W, large connected bubbles were formed along the centreline of the joint. Further increase of the energy to 80 W, produced more bubbles, however they become more dispersed and

occupied a larger area of the joint.

(ii) The results of the XPS analysis revealed that the Ti/PET interface contained new Ti–C, Ti–O and Ti_2O_3 bonds after laser irradiation, and the thickness of the interface, in general, increased with increasing laser energy input. Increasing the laser input energy also increased the intensity count of the chemical bonds.

(iii) The chemical bond intensities of the Ti–C and Ti–O species have pronounced effects on the tensile failure load of the joints. When the amount of bubbles is high, the weakening effect of the bubbles outweighs the strengthening effect of the high chemical bonding intensity.

B. Ultrasound-aid laser joining metal-to-plastic (U-LAMP)

(a) Low laser energy input

(i) For both the joints formed with and without ultrasonic vibration, no bubbles were observed when the laser power used was below 30 W. A higher laser power, such as 45 W, produced large quantities of bubbles in the joint.

(ii) For specimens joined at 30 W, the strength of the joint produced using ultrasonic aid, in terms of tensile failure load, was always higher than that of the joint formed without ultrasonic aid. This improvement can be as high as three times. When compared to the joint produced using a higher laser power (45 W) and without ultrasonic aid, and where bubbles had formed, the joint strength of the ultrasonic-aid specimen (laser power 30 W) was nearly double the former.

(iii) Ultrasonic vibration promotes chemical reactions between molten PET and Ti metal. The XPS results showed that the U-LAMP specimens have higher bond intensities of Ti-C, at the joint interface, than the LAMP specimens.

(b) High laser energy input

(i) In order to take advantage of using ultrasonic vibration in the laser joining of plastics to metals to drive laser-induced bubbles out of the molten plastic zone, a transducer tool with a surface cavity is needed to create a low pressure region in the molten plastic.

(ii) For the conventional LAMP joining process, the formation of bubbles in the joint zone is inevitable and the amount increases when the laser power is increased. On the other hand, with the new U-LAMP process and using an offset technique, the amount of bubbles was significantly reduced, and in most cases no sizable bubbles could be observed by optical microscopy. It is believed that U-LAMP can be potentially applied to other metal-plastic pairs to achieve similar outcomes.

(iii) The theoretical basis on the combined effect of pressure and temperature fields on the track movement of bubbles was studied, and the predicated results were in good agreement with the experimental results together with supporting evidence from high speed camera images.

(iv) Comparing the fracture load of the LAMP and U-LAMP specimens, the failure load of the latter was significantly higher than that of the LAMP specimen. With regard to the failure mode, the LAMP specimens mainly fractured at the metal-plastic interface, while for the U-LAMP specimens,

the fractures generally occurred in the plastic part.

(v) The improvement obtained for the joints formed with the aid of ultrasonic vibration is believed to be due to the absence of bubbles in the joint and a strong chemically bonded interface is formed.

(vi) The fatigue resistance of U-LAMP specimens is superior to that of LAMP specimens.

Chapter 11

Suggestions for Future Work

The new laser joining technology developed in this research study, namely ultrasound-aided laser joining (U-LAMP), has been successfully applied to bond plastics to metal, and the mechanical properties of the joints were superior to those of the conventional laser joining metal-to-plastic (LAMP) process. However, there are still some interesting subjects worthy of further investigation; they are:

(i) This study used a longitudinal mode of vibration, and it is worth to investigate another mode of vibration on bubble movement, i.e. the flexural mode.

(ii) Having confirmed the superiority of the U-LAMP process in joining simple rectangular coupons, larger joint surfaces and different shapes of joints should be explored.

(iii) Transducer tools with different surface profiles to suit different joint profiles need to be realised.

(iv) It is believed that U-LAMP should also be successfully applied to other metal-plastic pairs with similar outcomes. To confirm this, more experiments are needed.

(v) In modelling bubble movements, many assumptions were made. The influence of ultrasound on the viscosity of the molten PET and the variation of density of molten polymer as a function of temperature were

not taken into account. Therefore, the mathematical model of bubble movement needs to be refined.

(vi) The fatigue test was only conducted at one load level, more tests are required at different load levels in order to fully understand the fatigue crack initiation and propagation behaviour.

Appendix A

XPS Spectra for LAMP Samples

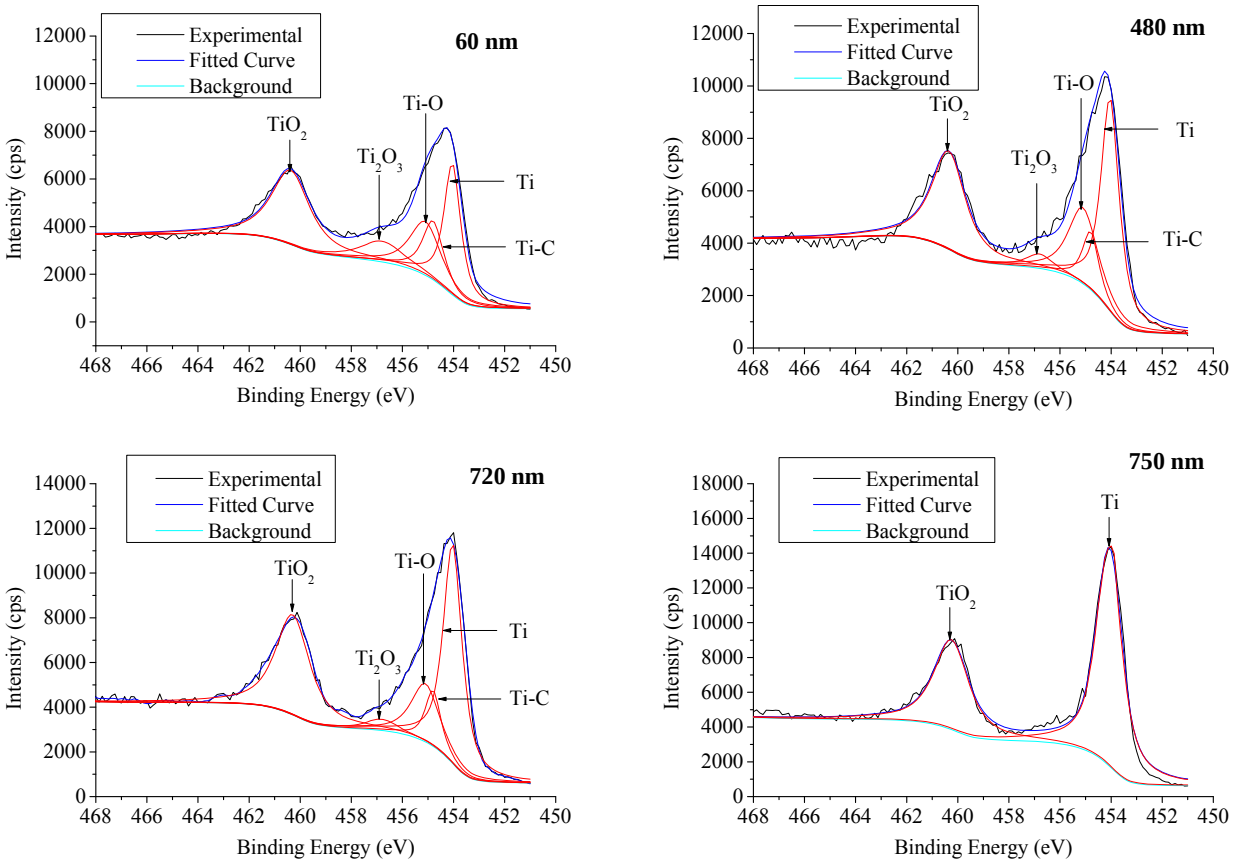

Curve fitting conducted for Ti2p high resolution XPS spectra obtained from the Ti side of the joined samples after ion-milling to various depths for Sample 1 in Chapter 4 (laser power 35 W, laser speed 4 mm/s, laser frequency 20 Hz).

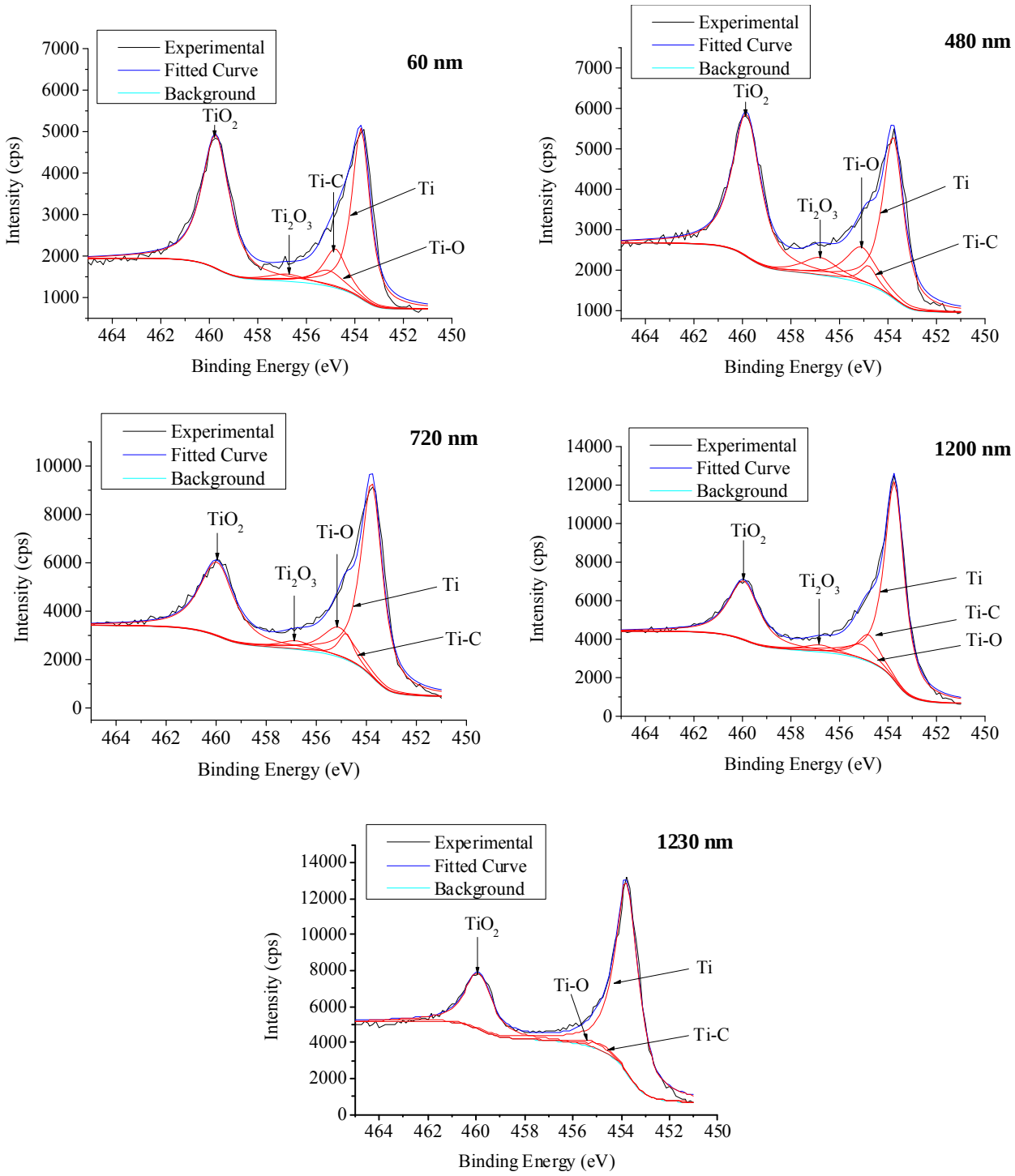

Curve fitting conducted for Ti2p high resolution XPS spectra obtained from the Ti side of the joined samples after ion-milling to various depths for Sample 2 in Chapter 4 (laser power 45 W, laser speed 4 mm/s, laser frequency 20 Hz).

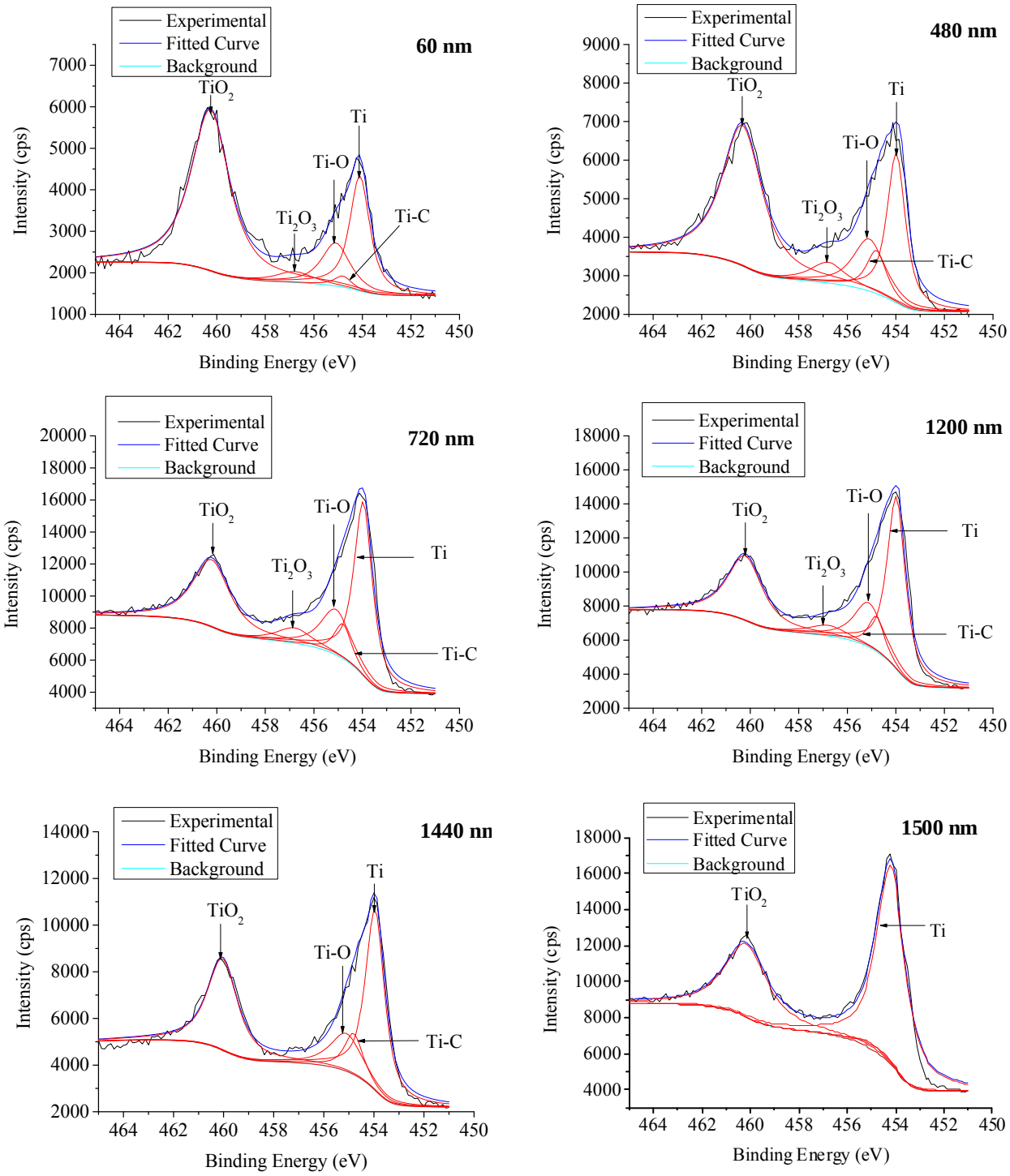

Curve fitting conducted for Ti2p high resolution XPS spectra obtained from the Ti side of the joined samples after ion-milling to various depths for Sample 3 in Chapter 4 (laser power 60 W, laser speed 4 mm/s, laser frequency 20 Hz).

.

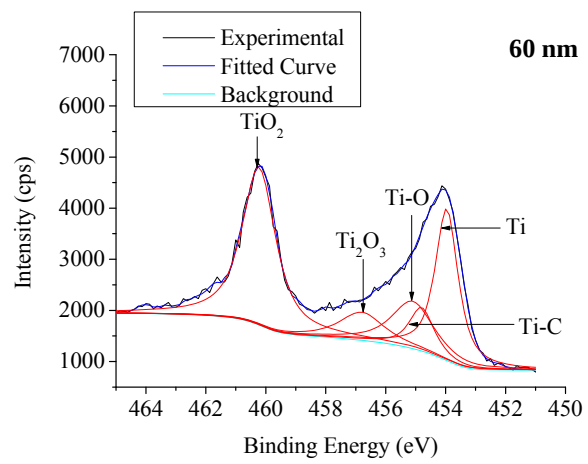
Experimental
Fitted Curve
Background
60 nm
TiO2
Ti-O
Ti2O3
Ti
Ti-C
Intensity (cps)
Binding Energy (eV)

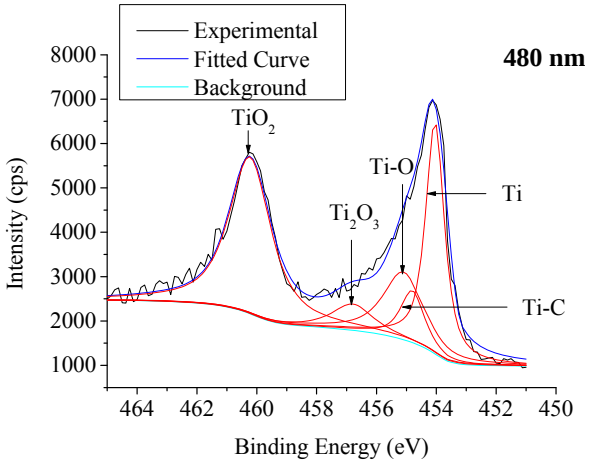
Experimental
Fitted Curve
Background
480 nm
TiO2
Ti-O
Ti2O3
Ti
Ti-C
Intensity (cps)
Binding Energy (eV)

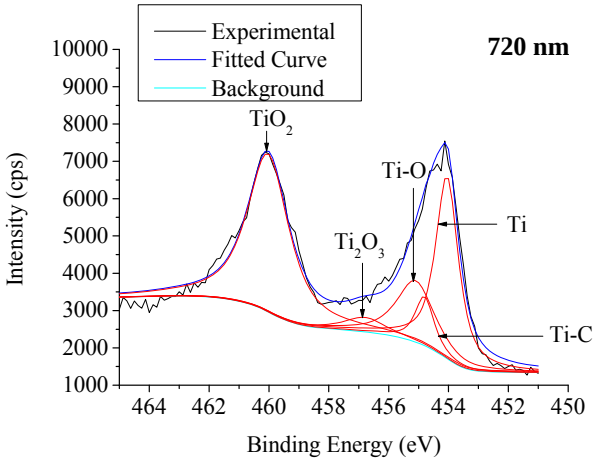
Experimental
Fitted Curve
Background
720 nm
TiO2
Ti-O
Ti2O3
Ti
Ti-C
Intensity (cps)
Binding Energy (eV)

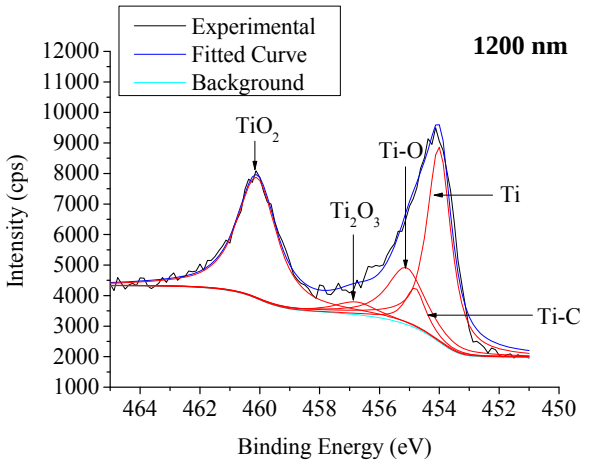
Experimental
Fitted Curve
Background
1200 nm
TiO2
Ti-O
Ti2O3
Ti
Ti-C
Intensity (cps)
Binding Energy (eV)

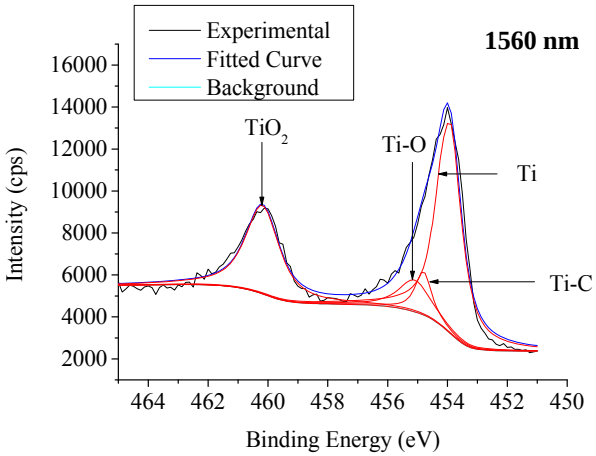
Experimental
Fitted Curve
Background
1560 nm
TiO2
Ti-O
Ti
Ti-C
Intensity (cps)
Binding Energy (eV)

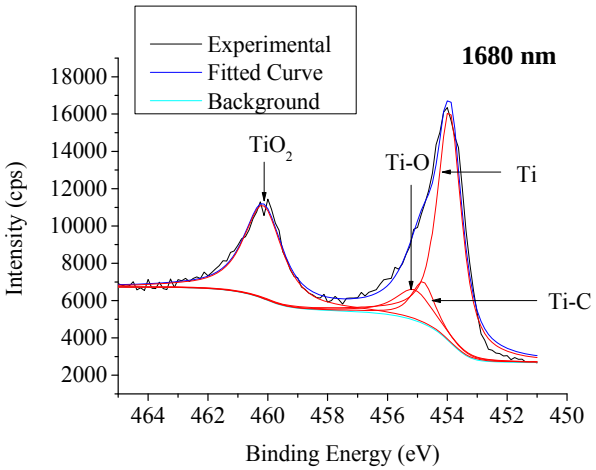
Experimental
Fitted Curve
Background
1680 nm
TiO2
Ti-O
Ti
Ti-C
Intensity (cps)
Binding Energy (eV)

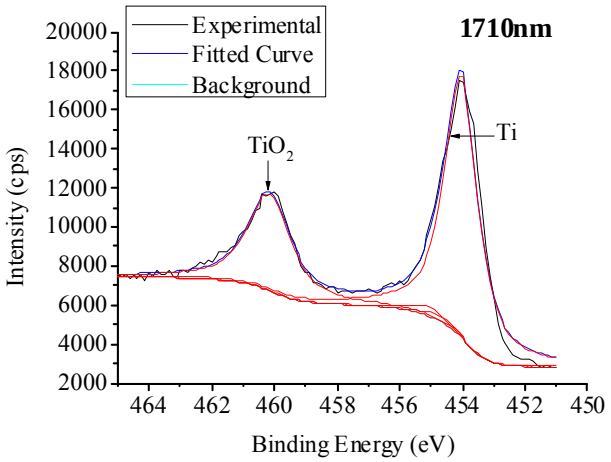

Curve fitting conducted for Ti2p high resolution XPS spectra obtained from the Ti side of the joined samples after ion-milling to various depths for Sample 4 in Chapter 4 (laser power 80 W, laser speed 4 mm/s, laser frequency 20 Hz).

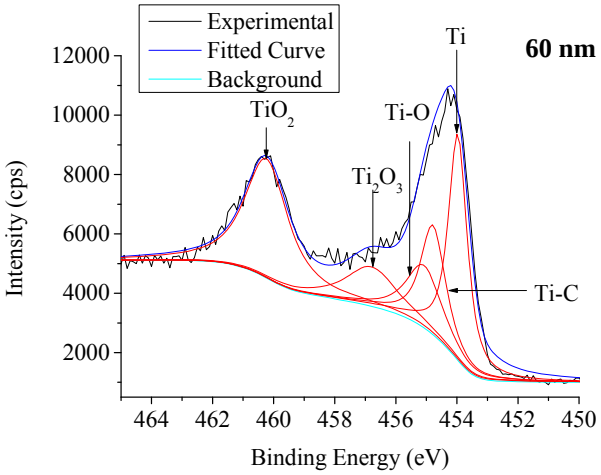

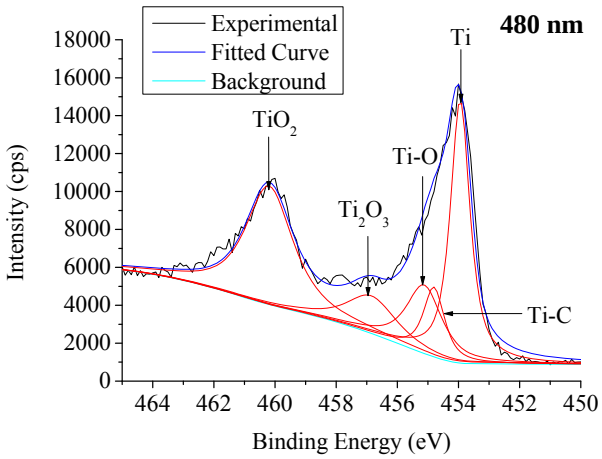

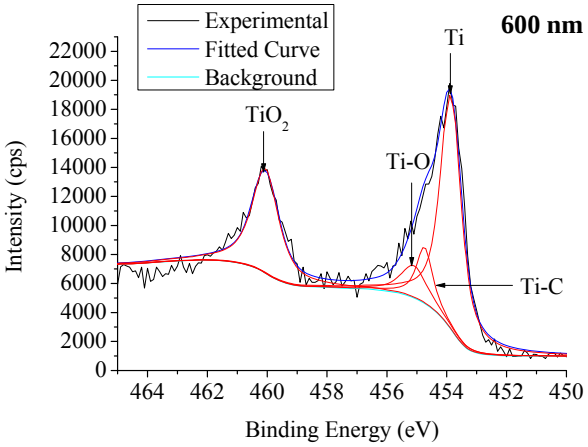

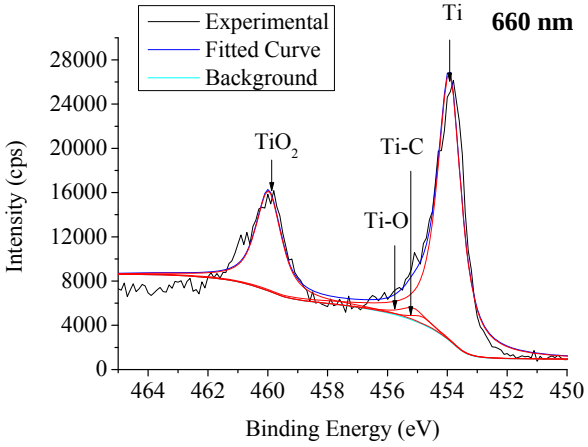

Curve fitting of Ti2p high resolution XPS spectra obtained from the Ti side of the joined samples after ion-milling to various depths of the LAMP specimen (laser power 30 W, laser speed 4 mm/s, laser frequency 20 Hz).

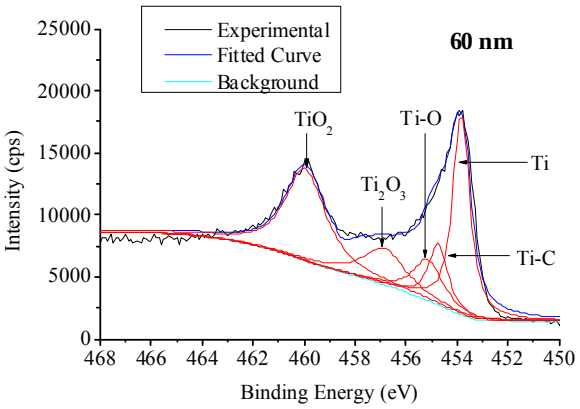

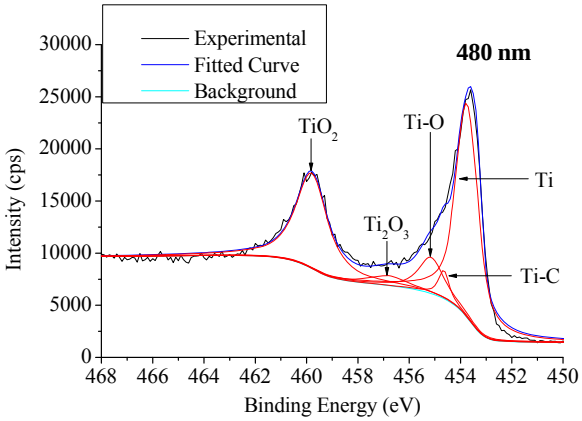

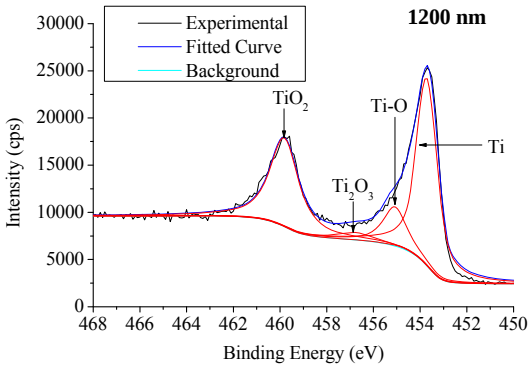

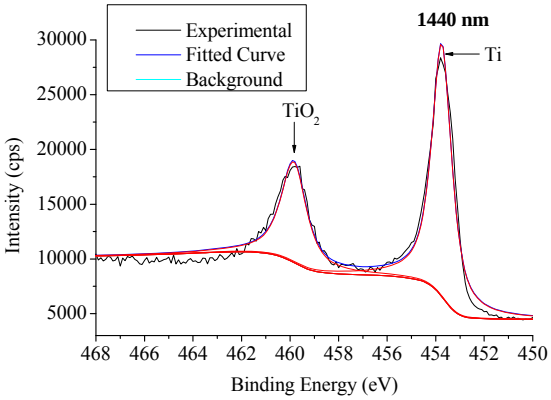

Curve fitting conducted for Ti2p high resolution XPS spectra taken from the Ti side of LAMP sample for various depths (laser power 55 W, welding speed 4 mm/s, laser frequency 20 Hz) .

Appendix B

XPS Spectra for U-LAMP Samples

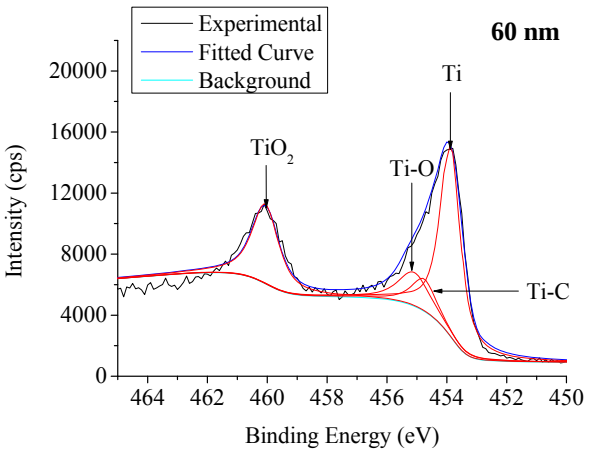

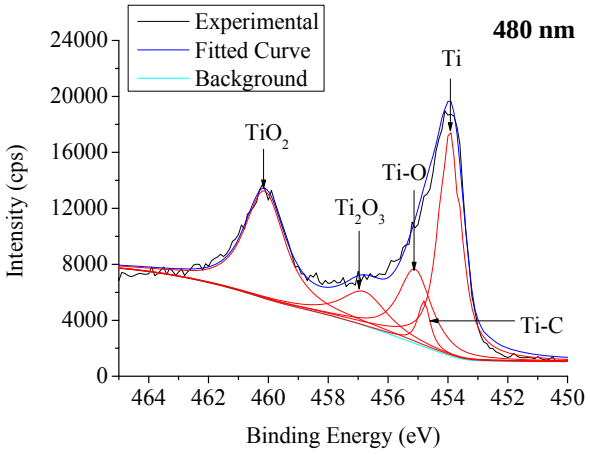

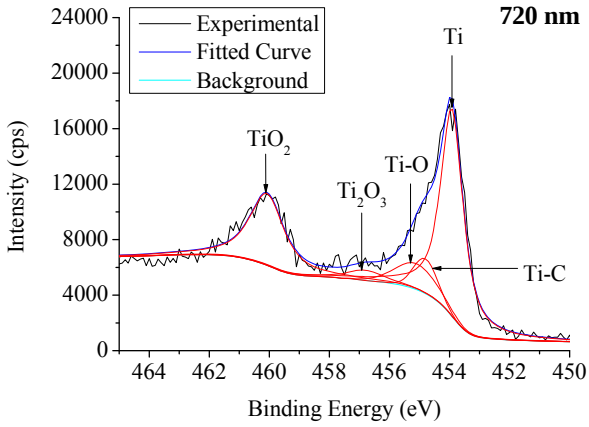

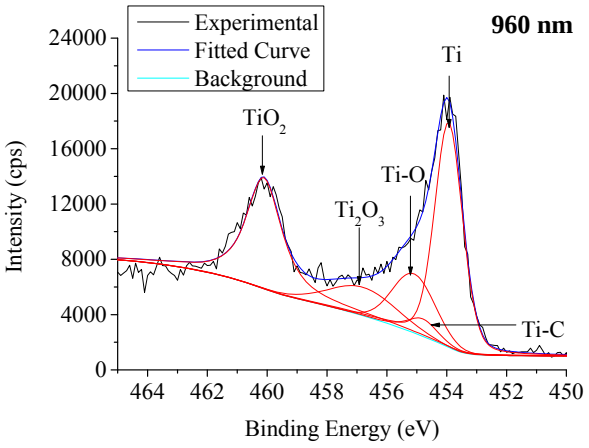

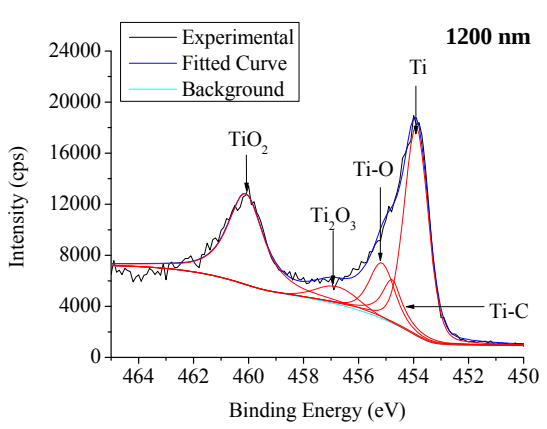

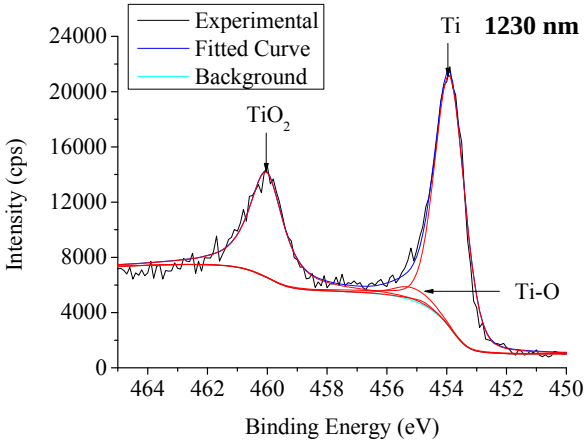

Curve fitting of Ti2p high resolution XPS spectra obtained from the Ti side of the U-LAMP samples (laser power 30 W, laser speed 4 mm/s, laser frequency 20 Hz, with vibration amplitude = 2 μm) after ion-milling to various depths.

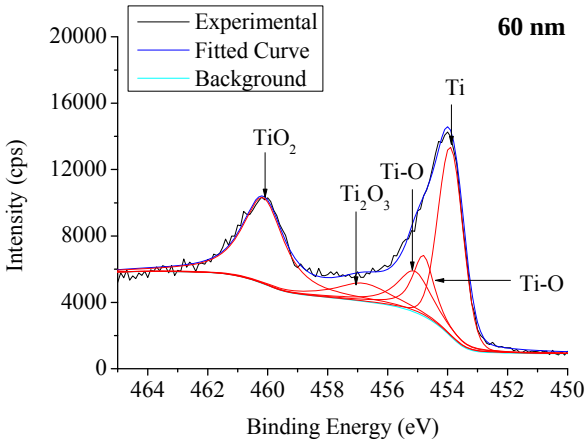

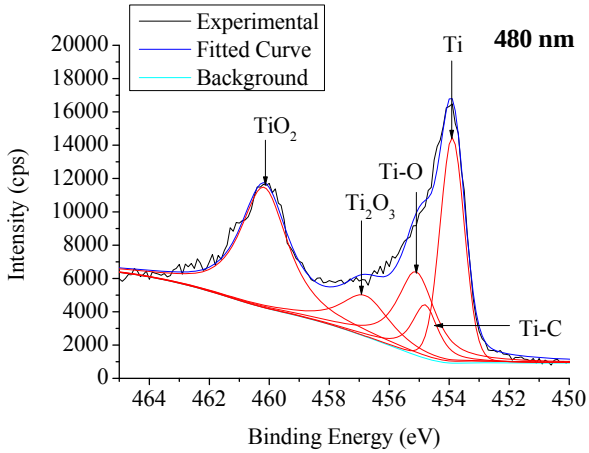

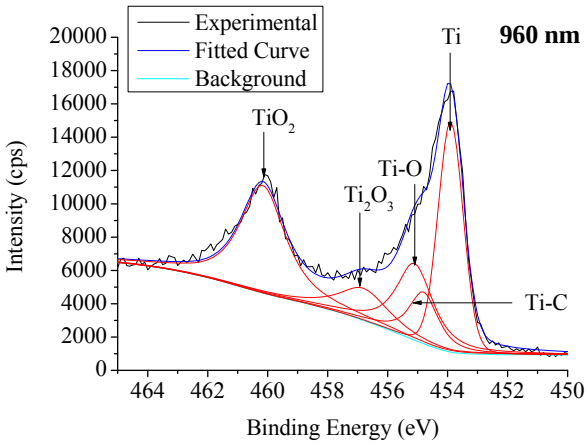

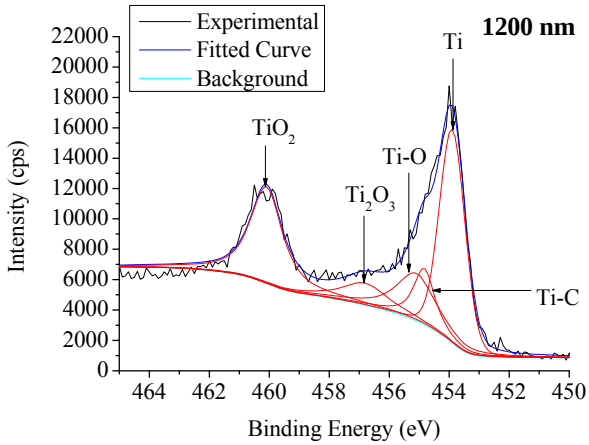

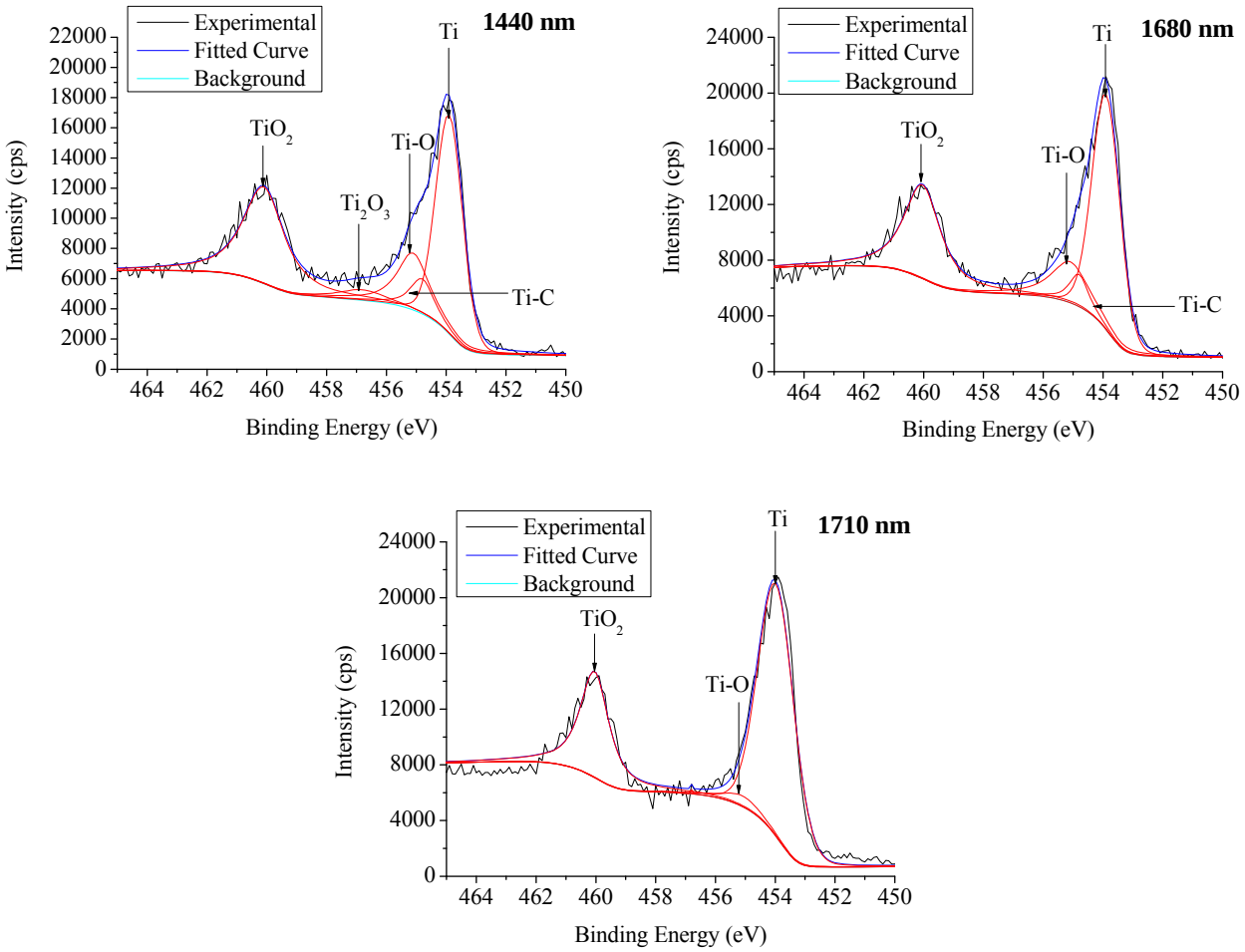

Curve fitting of Ti2p high resolution XPS spectra obtained from the Ti side of the U-LAMP samples (laser power 30 W, laser speed 4 mm/s, laser frequency 20 Hz, with vibration amplitude = 4 μm) after ion-milling to various depths.

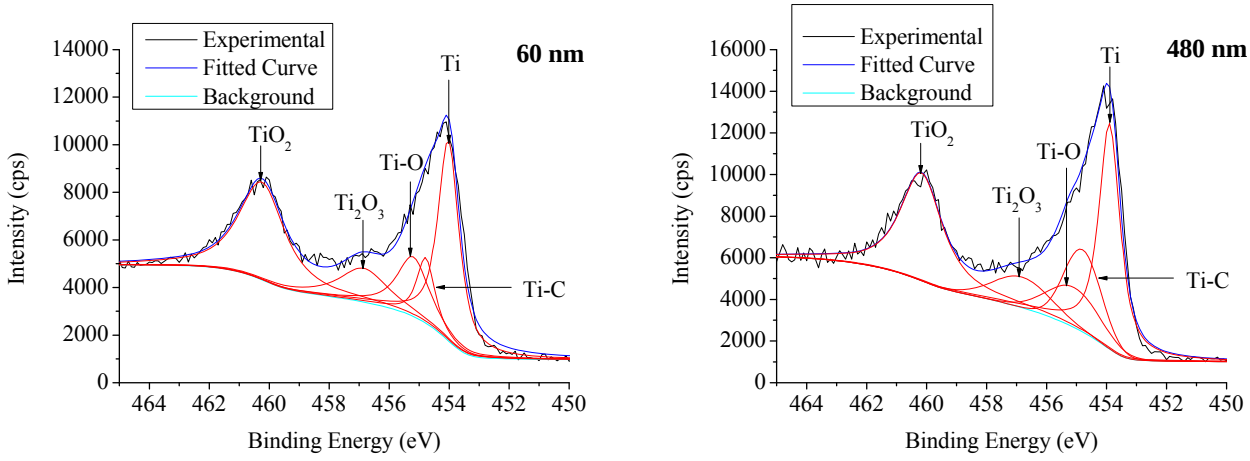

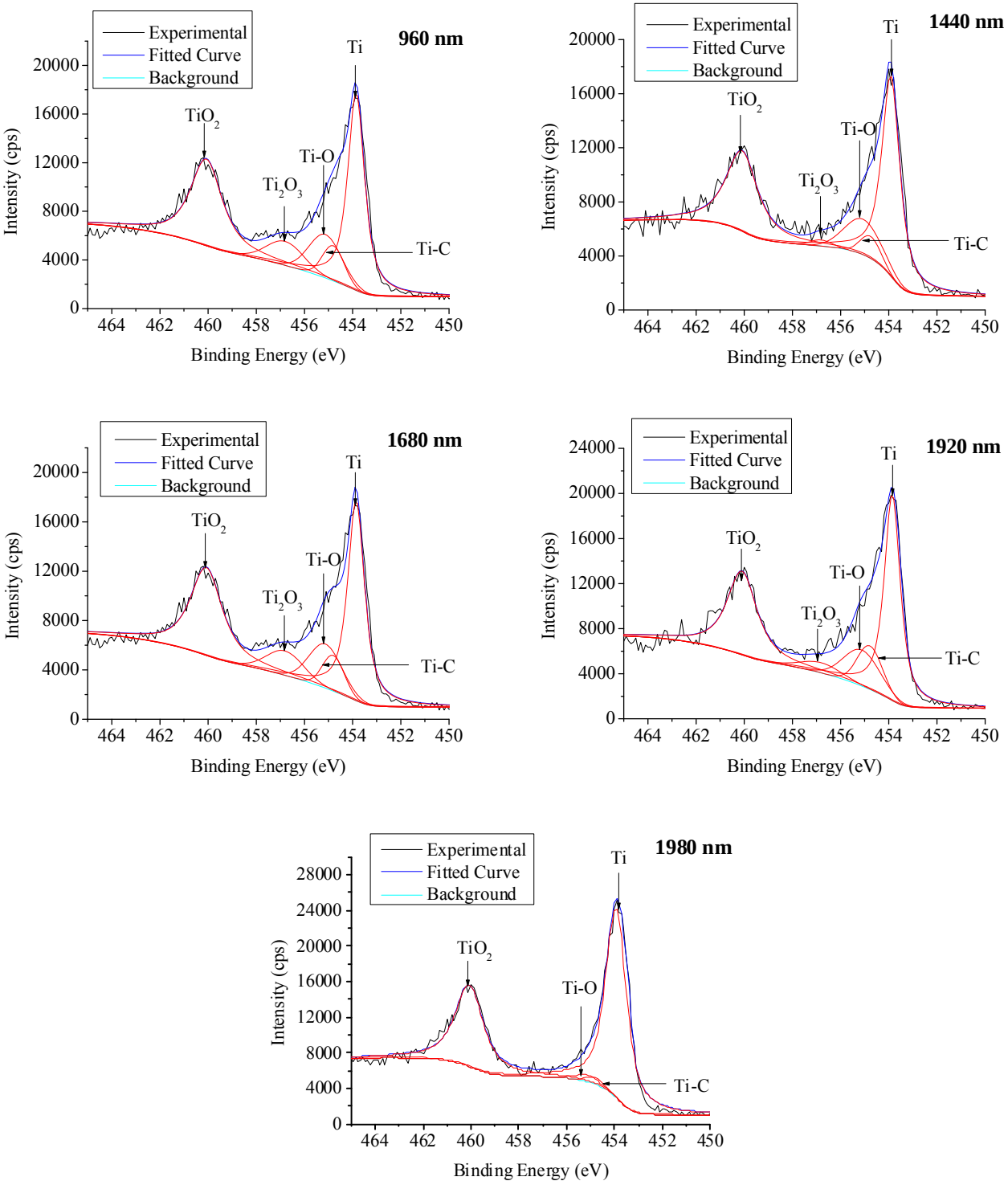

Curve fitting of Ti2p high resolution XPS spectra obtained from the Ti side of the U-LAMP samples (laser power 30 W, laser speed 4 mm/s, laser frequency 20 Hz, with vibration amplitude = 6 μm) after ion-milling to various depths.

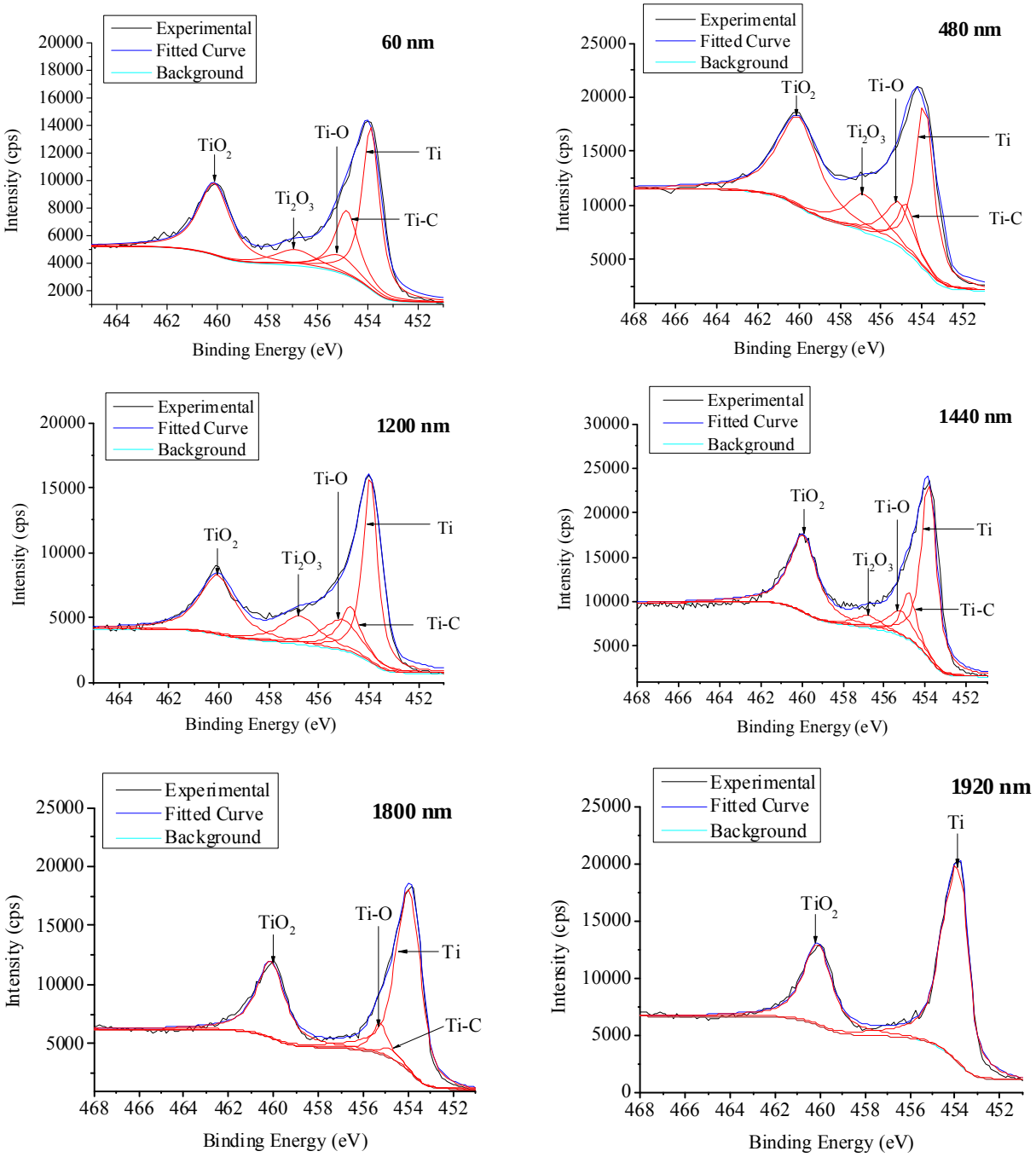

Curve fitting conducted for Ti2p high resolution XPS spectra taken from the Ti side of the U-LAMP sample with the ultrasonic duty cycle of 20% for various depth (laser power 55 W, welding speed 4 mm/s, pulsed frequency 20 Hz, with vibration amplitude = 4 μm)

References

[1] H.L. Gower, R.R.G.M. Pieters, I.M. Richardson. Pulsed laser welding of metal-polymer sandwich materials using pulse shaping. Laser Applications, 2006, 18, 35–41

[2] X. Wang, P. Li, Z.K. Xu. Laser transmission joint between PET and titanium for biomedical application. Materials Processing Technology, 2010, 210, 1767–1771

[3] F. Haddadi. Rapid intermetallic growth under high strain rate deformation during high power ultrasonic spot welding of aluminium to steel. Materials & Design, 2015, 66, 459–472

[4] Y.C. Lim, L. Squires, T.Y. Pan. Study of mechanical joint strength of aluminum alloy 7075-T6 and dual phase steel 980 welded by friction bit joining and weld-bonding under corrosion medium. Materials &Design, 2015, 69, 37–43

[5] I. Bauer, U.A. Russek, H.J. Herfurth. Laser micro-joining of dissimilar and biocompatible materials. Conference on Photon Processing in Microelectronics and Photonics III, 2004, 5339, 454–464

[6] H. Nakamura, T. Masaki. Plastic welding with diode lasers. Japanese Weld Socity, 2003, 72, 125–136

[7] S.T. Amancio-Filho, J.F. dos Santos. Joining of polymers and polymers–metal hybrid structures: Recent developments and trends. Polymer Engineering and Science,2009, 49, 1461–1476

[8] D. Elena, A. Lazar. Adhesive bonding between Aluminium and

polytetra - fluoroethylene. Material Processing Technology, 2003,143-144，191–194

[9] S. Katayama, Y. Kawahito. Laser direct joining of metal and plastic. Scripta Materialia, 2008, 59, 1247–1250

[10] Y. Kawahito, Y. Niwa, T. Terajima. Laser direct joining of glassy metal Zr55Al10Ni5Cu30 to engineering plastic polyethylene terephthalate. Materials Transactions, 2010, 51, 1433-1436

[11] Y. Kawahito, S. Katayama, K. Nishimoto. Laser direct joining between stainless steel and amorphous polyamide plastic. 8th ASME/JSME Thermal Engineering Joint Conference, 2011, 1119-1123

[12] Y. Kawahito, S. Katayama. Characteristics of LAMP joining structures for several materials. Conference on Processing of ICALEO, 2010, 1469–1473

[13] F. Lambiase, S. Genna. Laser-assisted direct joining of AISI304 stainless steel with polycarbonate sheets: Thermal analysis, mechanical characterization, and bonds morphology. Optics and laser technology, 2017, 88, 205–214

[14] A. Fortunato, G. Cuccolini, A. Ascari, L. Orazi, G. Campana, G. Tani. Hybrid metal-plastic joining by means of laser. International Journal of Material Forming, 2010, 3, 1131–1134

[15] H. Edmund, H. Wolf-Martin, P. Reinhart. Laser transmission micro-welding. Micro-system Technology, 2006, 12, 632–639

[16] M. Wahba, Y. Kawahito, S. Katayama. Laser direct joining of AZ91D thixomolded Mg alloy and amorphous polyethylene terephthalate. Journal of Materials Processing Technology, 2011, 211, 1166–1174

[17] G. Meucci, S. Esente, I. Esente. Anterior capsule cleaning with an ultrasound irrigating scratcher. Journal of cataract and refractive surgery, 1991, 17, 75-79

[18] Y. Tanimura, K. Yoshida, Y. Watanabe. A study on cleaning ability of oscillating bubbles driven by low-frequency ultrasound. 30th symposium on ultrasonic electronics, 2009, 49(7)

[19] L.M. Jiang, B. Verhaagen, M. Versluis. An evaluation of the effect of pulsed ultrasound on the cleaning efficacy of passive ultrasonic irrigation. Journal of endodontics, 2010, 36, 1887-1891

[20] R.K. Ing, J.P. Monchalin. Broad-band optical-detection of ultrasound by 2-wave mixing in photorefractive crystal. Applied physics letters, 1991, 59, 3233-3235

[21] J.J. Hawkes, R.W. Barber, D.R. Emerson. Continuous cell washing and mixing driven by an ultrasound standing wave within a microfluidic channel.Lab on a chip, 2004, 4, 446-452

[22] T.W. Chan, T.M. Yue, H.C. Man. Ultrasonically aided laser drilling of particle reinforced aluminium based composites. Material science and technology, 1998, 14, 1039-1044

[23] K. Egashira, R. Kumaga, R. Okina. Drilling of microholes down to 10 mu m in diameter using ultrasonic grinding. Precision engineering,

2014, 38, 605-610

[24] S. Takahasi, P. Korondi, B. Resko, Y. Kunii. The development of ultrasonic drilling device. 2008 6th International Symposium on Applied Machine Intelligence and Informatics, 2008, 105-109

[25] A. Shoh. Welding of thermoplastics by ultrasound. Ultrasonics, 1976, 14, 209-217

[26] G. Amza, A. Hadar, Z. Apostolescu, G. Girleanu, L. Anton. Experimental and theoretical research regarding the acoustical parameters influence on the ultrasound welding of inteligent composite. Material plastice, 2007, 44, 60-65

[27] G. Amza, D. Dobrota. Ultrasound effect on the mechanical properties of parts loaded by welding. Metalurgija, 2013, 52, 83-86

[28] J.B. Li, K.K. Xu, X.B. Lin, X.Y. Wu, G.L. Gao. Research on the flow characteristics of polymer injection molding under ultrasonic vibration and plastics' mechanical strength. International Conference on Engineering Design and Optimization, 2011, 37-38, 1092-1100

[29] J.Y. Chen, Y.Z. Chen, H.L. Li, S.Y. Lai, J. Jow. Physical and chemical effects of ultrasound vibration on polymer melt in extrusion. Ultrasonic sonochemistry, 2010, 17, 66-71

[30] Y.Z. Chen, H.L. Li. Mechanism for effect of ultrasound on polymer melt in extrusion. Journal of polymer science part B-polymer physics, 2007, 45, 1226-1233

[31] A.A. Panov, T.A. Anasova, G.E. Zaikov, A.K. Panov. Influence of

ultrasound on the basic parameters of the extrusion of polymer melts. Theoretical foundations of chemical engineering, 2011, 45, 436-442

[32] O. Louisnard. A simple model of ultrasound propagation in a cavitating liquid.Part II: Primary Bjerknes force and bubble structures. Ultrasonics sonochemistry, 2012, 19, 66-76

[33] O. Louisnard. Analytical expressions for primary Bjerknes force on inertial cavitation bubbles. Physical review E, 2008, 78, 036322

[34] R. Mettin, I. Akhatov, U. Parlitz, C.D. Ohl, W. Lauterborn. Bjerknes forces between small cavitation bubbles in a strong acoustic field. Physical review E, 1997, 56, 2924-2931

[35] J.J. Jiao, Y. He, T. Leong, S.E. Kentish, M. Ashokkumar, R. Manasseh, J. Lee. Experimental and theoretical studies on the movements of two bubbles in an acoustic standing wave field. Journal of physical chemistry B, 2013, 117, 12549−12555

[36] C.H. Wang, J.C. Cheng. Interaction of a bubble and a bubble cluster in an ultrasonic field. Chinese physics B, 2013, 22, 014304

[37] J.D. Majumdar, I. Manana. Laser-assisted frabrication of materials. Springer Series in Materials Science, Berlin, New York: Springer, 2013, 161, 28pp, ISBN 978-3-642-28359-8 (eBook)

[38] W.M. Steen, J. Mazumder. Laser material processing(fourth edition).Springer-Verlag London Limited, London: Springer, 2010, 199pp, e-ISBN 978-1-84996-062-5 (eBook)

[39] P. Schaaf. Laser processing of materials. Springer Series in Materials

Science, Heidelberg, New York: Springer-Verlag, 2010, 139, 21pp, e-ISBN 978-3-642-13281-0

[40] M.K. Chun, K. Rose. Interaction of high-intensity laser beams with metals. Journal of Applied Physics, 1970, 41, 614-620

[41] J. Ihlemann. Excimer laser ablation of fused-silica. Applied surface science, 1992, 54, 193-200

[42] M. Bolle, K. Luther, J. Troe, J. Ihlemann, H. Gerhardt. Photochemically assisted laser ablation of doped polymethyl-methacrylate. Applied surface science, 1990, 46, 279-283

[43] S. Katayama. Laser joining of metal and plastic. Industrial Laser Solutions, 2010, 25(6)

[44] F. Yusof, M. Yukio, M. Yoshiharu, M.H.A. Shukor. Effect of anodizing on pulsed Nd:YAG laser joining of polyethylene terephthalate (PET) and aluminium alloy (A5052). Materials & Design, 2012, 37, 410–415

[45] X.H. Tan, J. Zhang, J.G. Shan, S.L. Yang, J.L. Ren. Characteristics and formation mechanism of porosities in CFRP during laser joining of CFRP and steel. Composites Part B-Engineering, 2015, 70, 35-43

[46] W. Tillmann, A. Elrefaey, L. Toward. Toward process optimization in laser welding of metal to polymer. Marerialwissenschaft und werkstofftechnik, 2010, 41, 879-883

[47] J. Cheon, S.J. Na. Relation of joint strength and polymer molecular structure in laser assisted metal and polymer joining. Science and

Technology of Welding and Joining, 2014, 19(8), 631–637

[48] Y. Farazila, Y. Miyashita, H. Wang, Y. Mutoh, Y. Otsuka. YAG laser spot welding of PET and metallic materials. Journal of laser micro nanoengineering, 2011, 6, 69-74

[49] Y. Miyashita, M. Takahashi, M. Takemi. Dissimilar materials micro welding between stainless steel and plastics by using pulsed YAG laser. Journal of solid mechanics and materials engineering, 2009, 3, 409-415

[50] A. Roesner, S. Scheik, A. Olowinsky, A. Gillner, U. Reisgen, M. Schleser. Laser assisted joining of plastic metal hybrids. Physics Procedia, 2011, 12, 370–377

[51] D.G. Georgiev, T. Sultana, A. Mian, G. Auner, H. Herfurth, R. Witte, G. Newaz. Laser fabrication and characterization of sub-millimeter joints between polyimide and Ti-coated borosilicate glass. Journal of Materials Science, 2005, 40, 5641–5647

[52] G. Newaz, A. Mian, T. Sultana, T. Mahmood, D.G. Georgiev, G. Auner, R. Witte, H. Herfurth. A comparison between glass/polyimide and titanium/polyimide microjoint performances in cerebrospinal fluid. Journal of Biomedical Materials Research Part A, 2006, 79A, 159–165

[53] A. Mian, T. Sultana, G. Auner, G. Newaz. Bonding mechanisms of laser-fabricated titanium/polyimide and titanium coated glass/polyimide microjoints. Surface and Interface Analysis, 2007, 39, 506–511

[54] A. Mian, G. Newaz, L. Vendra, N. Rahman, D.G. Georgiev, G. Auner,

R. Witte, H. Herfurth. Laser bonded microjoints between titanium and polyimide for applications in medical implants. Journal of Materials Science-Materials in Medicine, 2005, 16, 229–237

[55] L.K. Massey. Permeability Properties of Plastics and Elastomers: A Guide to Packaging and Barrier Materials, 2nd edition. William Andrew Publishing: New York, 2003, 206pp

[56] G.L. Georgiev, R.J. Baird, E.F. McCullen, G. Newaz, G. Auner, R. Patwa, H. Herfurth. Chemical bond formation during laser bonding of Teflon (R) FEP and titanium. Applied Surface Science, 2009, 255, 7078–7083

[57] G.L. Georgiev, T. Sultana, R.J. Baird, G. Auner, G. Newaz, R. Patwa, H. Herfurth. Laser bonding and characterization of Kapton FN/Ti and Teflon FEP/Ti systems. Journal of Materials Science, 2009, 44, 882–888

[58] E. Rodriguez-Vidal, C. Sanz, C. Soriano, J. Leunda, G. Verhaeghe. Effect of metal micro-structuring on the mechanical behavior of polymer–metal laser T-joints. Journal of Materials Processing Technology, 2016, 229, 668-677

[59] D.J. Jung, J. Cheon, S.J. Na. Effect of surface pre-oxidation on laser assisted joining of acrylonitrile butadiene styrene (ABS) and zinc-coated steel, 2016, 99, 1-9

[60] C.W. Chan, G.C. Smith. Fibre laser joining of highly dissimilar materials: Commercially pure Ti and PET hybrid joint for medical

device applications. Materials & Design, 2016, 103, 278-292

[61] Y. Farazila, Y. Mutoh, Y. Miyashita. Effect of pre-oxidized CuO layer in joining between polyethylene terephalate (PET) and copper (Cu) by using pulsed Nd:YAG laser. Advanced Materials Research, 2010, 129-131, 714-718

[62] W. Robert, Jr. Messler. Joining composite materials and structures: some thought-provoking possibilities. Journal of thermoplastic composite materials, 2004, 17, 51-75

[63] F.C. Liu, J. Liao, K. Nakata. Joining of metal to plastic using friction lap welding. Materials and Design, 2014, 54, 236-244

[64] F. Yusof, Y. Miyashita, N. Seo, Y. Mutoh, R. Moshwan. Utilising friction spot joining for dissimilar joint between aluminium alloy (A5052) and polyethylene terephthalate. Science and Technology of Welding and Joining, 2012, 17, 544-548

[65] S.T. Amancio-Filhoa, C. Buenoa, J.F. Dossantosa, N. Huber, E. Hage. On the feasibility of friction spot joining in magnesium/fiber-reinforced polymer composite hybrid structures. Materials science and engineering A, 2011, 528, 3841-3848

[66] F.C. Liu, J. Liao, Y. Gao, K. Nakata. Effect of plasma electrolytic oxidation coating on joining metal to plastic. Science and Technology of Welding and Joining, 2015, 20, 291-296

[67] K.Nagatsuka, S.Yoshida, A.Tsuchiya, K.Nakata. Direct joining of carbon-fiber–reinforced plastic to an aluminum alloy using friction lap

joining. Composites Part B-Engineering, 2015, 73, 82-88

[68] F.Balle, G.Wagner, D.Eifler. Ultrasonic metal welding of aluminium sheets to carbon fibre reinforced thermoplastic composites. Advanced engineering materials, 2009, 11, 35-39

[69] G.Wagner, F.Balle, D.Eifler. Ultrasonic welding of aluminum alloys to fiber reinforced polymers. Advanced engineering materials, 2013, 15, 792-803

[70] R.Y. Yeh, R.Q. Hsu. Development of ultrasonic direct joining of thermoplastic to laser structured metal. International Journal of Adhesion & Adhesives, 2016, 65, 28-32

[71] E.C.Bernhardt. Effect of ultrasound on thermolplastic melts. Journal of industrial and engineering chemistry, 1954, 46,742-746

[72] A.O.Carlos, E.G.Carlos, M.C.Guillermo, B.B.Dario, M.Alfonso, L.Francesca. An overview of progress and current challenges in ultrasonic treatment of polymer melts. Advances in polymer technology, 2013, 32, 582-602

[73] S.L.Peshkovskii, M.L.Friedman, A.I.Tukachinshii, G.V.Vinogradov, N.S.Enikolopian. Acoustic cavitation and its effect on flow in polymers and filled systems. Polymer composites, 1983, 4, 126-134

[74] V.V.Yashinl, A.I.Isayev. A model for rubber degradation under ultrasonic treatment: part I. acoustic cavitation in viscoelastic solid. Rubber chemistry and technology, 1999, 72, 741-757

[75] R. Kumar, A.I. Isayev. Thermotropic LCP/CNF nanocomposites

prepared with aid of ultrasonic waves. Polymer, 2010, 51, 3503-3511

[76] A.Z. Zsayev, C.M. Wong, X. Zeng. Effect of oscillations during extrusion on rheology and mechanical properties of polymers. Advances in polymer technology, 2003, 10, 31-45

[77] L.H. Thompson, L.K. Doraiswamy. Sonochemistry: Science and Engineering. Industrial & engineering chemistry research, 1999, 38, 1215-1249

[78] D.E. Hughes, W.L. Nyborg. Cell disruption by ultrasound: streaming and other activity around sonically induced bubbles is a cause of damage to living cells. Science, 1962, 138, 108-114

[79] F. Hao, V. Gustavo, C. Barbosa. Ultrasound technology for food and bioprocessing. Springer Science+Business Media, LLC: New York, 2011, 1-12pp.

[80] J.W. Hoyt. Effect of polymer additives on jet cavitation. Journal of fluids engineering, 1976, 98, 106-111

[81] J.W. Hoyt, J.J. Taylor. A photographic study of cavitation in jet flow. Journal of fluids engineering, 1981, 103, 14-18

[82] G.L. Chanhine, D.H. Fruman. Dilute polymer solution effects on bubble growth and collapse. Physics of fluids, 1979, 22, 1406-1407

[83] H.S. Fogler, J.D. Goddard. Collapse of Spherical Cavities in Viscoelastic Fluids. Physics of fluids, 1970, 13, 1135-1141

[84] E.A. Brujan, C.D. Ohl, W. Lauterborn, A. Philipp. Dynamics of laser-induced cavitation bubbles in polymer solutions. Acustica, 1996,

82, 423-430

[85] E.A. Brujan, T. Ikeda, Y. Matsumoto. Dynamics of ultrasound-induced cavitation bubbles in non-Newtonian liquids and near a rigid boundary. Physics of fluids, 2004, 16, 2402-2410

[86] X.Y. Xi, F. Yang, D. Chen, Y. Luo, D. Zhang, N. Gu, J.R. Wu. A targeting drug-delivery model via interactions among cells and liposomes under ultrasonic excitation. Physics in medicine and biology, 2008, 53, 3251-3265

[87] Y.Z. Chen, H.L. Li. Mechanism for effect of ultrasound on polymer melt in extrusion. Journal of polymer science part B-Polymer physics, 2007, 45, 1226-1233

[88] H. Kim, J.W. Lee. Effect of ultrasonic wave on the degradation of polypropylene melt and morphology of its blend with polystyrene. Polymer, 2002, 43, 2585-2589

[89] H. Wu, W.T. Bao, S.Y. Guo. Enhanced flow behaviors of metallocene-catalyzed linear low-density polyethylene during ultrasound-assisted extrusion. Polymer engineering and science, 2010, 50, 2229-2235

[90] Campbell. Effects of vibration during solidification. International metals reviews, 1981, 2, 71-108

[91] M.J. Shortencarier, P.A. Dayton, S.H. Bloch, P.A. Schumann, T.O. Matsunaga, K.W. Ferrara. A method for radiation-force localized drug delivery using gas-filled lipospheres. IEE Transactions on ultrasonics

ferroelectrics and frequency control, 2004, 51, 822-831

[92] J.J. Rychak, A.L. Klibanov, J.A. Hossack. Acoustic radiation force enhances targeted delivery of ultrasound contrast microbubbles: In vitro verification. IEEE Transactions on Ultrasonics Ferroelectrics and Frequency Control

[93] V.F.K. Bjerknes. Fields of Force. Columbia University Press, New York, 1906

[94] A. Eller. Force on a bubble in a standing acoustic wave. Journal of the acoustical society of America, 1968, 43, 170-171

[95] M. Kornfeld, L. Suvorov. On the destructive action of cavitation. Journal of Applied Physics, 1994, 15, 495–506

[96] F.G. Blake. Bjerknes forces in stationary sound fields. Journal of the acoustical society of America, 1949, 21, 551

[97] A.A. Doinikov. Viscous effects on the interaction force between two small gas bubbles in a weak acoustic field. Journal of the acoustical society of America, 2002, 111, 1602-1609

[98] A. Harkin, T.J. Kaper, A.Nadim. Coupled pulsation and translation of two gas bubbles in a liquid. Journal of fluid mechanics, 2001, 445, 377-411

[99] R. Mettin, I. Akhatow, U. Parlitz, C.D. Ohl, W. Lauterborn. Bjerknes forces between small cavitation bubbles in a strong acoustic held. Physical review E, 1997, 56, 2924-2931

[100] E.A. Zabolotskaya. Interaction of gas-bubbles in a sound field. Soviet

physics acoustics-ussr, 1984, 30, 365-368

[101] M. Ida. Alternative interpretation of the sign reversal of secondary Bjerknes force acting between two pulsating gas bubbles. Physical review E, 2003, 67, 056617

[102] L.A. Crum. Bjerknes forces on bubbles in a stationary sound field. Journal of the acoustical society of America, 1975, 57, 1363-1370

[103] A.A. Doinikov. Bjerknes forces between two bubbles in a viscous fluid. Journal of the acoustical society of America, 1999, 106, 3305-3312

[104] U. Parlitz, R. Mettin, S. Luther, I. Akhatov, M. Voss, M. Lauterborn. Spatio-temporal dynamics of acoustic cavitation bubble clouds. Philosophical transactions of the royal society a-mathematical physical and engineering sciences, 1999, 357, 313-334.

[105] M. Ida. Phase properties and interaction force of acoustically interacting bubbles: A complementary study of the transition frequency. Physics of fluids, 2005, 17, 097107

[106] A.A. Doinikov, S.T. Zavtrak. Radiation forces between two bubbles in a compressible liquid. Journal of the Acoustical Society of America, 1997, 103, 1424-1431

[107] A.A. Doinikov. Translational Motion of a Spherical Bubble in an Acoustic Standing Wave of High Intensity. Physical Fluids A, 2002, 14, 1420−1425

[108] X.Y. Xi, F.B. Cegal, M. Lowe, A. Thiemann, T. Nowak, R. Mettin, F. Holsteyns, A. Lippert. Study on the bubble transport mechanism in an

acoustic standing wave field. Ultrasonics, 2011, 51, 1014-1025

[109] J.J. Jiao, Y. He, T. Leong, S.E. Kentish, M. Ashokkumar, R. Manasseh, J. Lee. Experimental and theoretical studies on the movements of two bubbles in an acoustic standing wave field. Physical chemistry B, 2013, 117, 12549-12555

[110] J. Kumar. Ultrasonic machining- A comprehensive review. Machining science and technology, 2013, 17, 325-379

[111] L. Balamuth. Ultrasonic vibrations assisted cutting tools. Metalworking Production, 1964, 108, 75–77

[112] D. Kremer. The state of the art of ultrasonic machining. CIRP Annals - manufacturing technology, 1981, 30, 107–115

[113] V.F. Kazantsev. Improving the output and accuracy of ultrasonic machining. Machines and Tooling, 1966, 37, 33-39

[114] W.L. Xu, L. Han. Piezoelectric actuator based active error compensation of precision machining. Measurement Science and Technology, 1999, 10, 106-111

[115] T.W. Chan. Ultrasound-aided laser machining. Ph.D thesis of the Hong Kong Polytechnic University, 1998

[116] D. Ensminger, F.B. Stulen. Ultrasonics: Data, Equations, and Their practical uses. U.S.: Taylor & Francis Group, 2009

[117] S.B. Amor, M. Jacquet, P. Fioux, M. Nardin. XPS characterisation of plasma treated and zinc oxide coated PET. Applied Surface Science, 2009, 255, 2009, 5052–5061

[118] D. Gonbeau, C. Guimon, G.P. Guillouzo, A. Levasseur, G. Meunier, R. Dormoy. XPS study of thin films of titanium oxysulfides. Surface Science, 1991, 254, 81–89

[119] K.F. Tamrin, Y. Nukman, S.S. Zakariyah. Laser Lap Joining of Dissimilar Materials: A Review of Factors Affecting Joint Strength. Materials and Manufacturing Processes, 2013, 28, 857-871

[120] Z.K. Xu, H.X. Liu, P. Li, X.H. Song, K. Wang, X. Wang. Numerical simulation of thermal/mechanical coupling in laser transmission microjoining of PET and titanium. Interational conference on materials science and engine, 2011, 160-162, 1118-1125

[121] M.Y. Hu, J.W. Shi. Effect of aluminum alloy surface absorptivity on weld shape. Hot working technology, 2009, 38, 150—151

[122] C.S. Wu. Welding thermal process and molten pool form. Beijing: China machine press, 2007

[123] Y.B. Chen. Modern laser welding technology. Beijing: China Science and Technology press, 2005, 35-39

[124] N. Fedelich et.al.. Thermal analysis of Polymers. METTLER TOLEDO (www.mt.com/ta-usercoms).

[125] M. A. White. Properties of materials. New York : Oxford University press, 1999.

[126] C.J. Nonhof, G.A. Luiten. Estimates for process conditions during the ultrasonic welding of thermoplastics. Polymer Engineering Science, 1996, 36, 1177–1183

[127] T.M. Nolunay, P.R. Dawson, K.K. Wang. Heating and bonding mechanisms in ultrasonic welding of thermoplastics. Polymer Engineering Science, 1983, 23, 726–733

[128] K.S. Suresh, M.R. Rani, K. Prakasan, R. Rudramoorthy. Modeling of temperature distribution in ultrasonic welding of thermoplastics for various joint designs. Journal of Materials Processing Technology, 2007, 186, 138–146

[129] J.F. Mano, J.C. Viana. Stress–strain experiments as a mechanical spectroscopic technique to characterise the glass transition dynamics in poly(ethylene terephthalate). Polymer Testing, 2006, 25, 953–960

[130] Z. Zhang, X. Wang, Y. Luo, Z. Zhang, L. Wang. Study on heating process of ultrasonic welding for thermoplastics. Journal of Thermoplastic Composite Materials, 2010, 23, 647–664

[131] A. Siddiq, E. Ghassemieh. Thermomechanical analyses of ultrasonic welding process using thermal and acoustic softening effects. Mechanics of Materials. 2008, 40, 982–1000

[132] A. Benatar, T.G. Gutowski. Ultrasonic welding of peek graphite apc-2 composites. Polymer Engineering Science, 1989, 29, 1705–1721

[133] A. Levy, S.L. Corre, I.F. Villegas. Modelling of the heating phenomena in ultrasonic welding of thermoplastic composites with flat energy directors. Journal of Materials Processing Technology, 2014, 214, 1361-1371

[134] B.Y. Jiang, H.J. Peng, W.Q. Wu, Y.L. Jia, Y.P. Zhang. Numerical

Simulation and Experimental Investigation of the Viscoelastic Heating Mechanism in Ultrasonic Plasticizing of Amorphous Polymers for Micro Injection Molding. Polymers, 2016, 8, 199-210

[135] J.L. Rose. Ultrasonic Waves in Solid Media. Cambridge University Press, 1999.

[136] H. Lu, J. Leng, S. Du. A phenomenological approach for the chemo-responsive shape memory effect in amorphous polymers. Soft Matter, 2013, 9, 3851–3858

[137] J.H. Ham, B. Platzer. Semi-empirical equations for the residence time distributions in disperse systems—Part 1: Continuous phase. Chemical Engineering & Technology, 2004, 27(11), 1172–1178

[138] F.J. Wortmann, K.V. Schulz. Stress relaxation and time/temperature superposition of polypropylene fibres. Polymer, 1995, 36, 315–321

[139] R.A. Schapery. Application of thermodynamics to thermomechanical, fracture, and birefringent phenomena in viscoelastic media. Journal of Applied Physics, 1964, 35, 1451–1465

[140] D.J. Plazek. The temperature dependence of the viscoelastic behavior of poly(vinyl acetate). Polymer Journal, 1980, 12, 43–53

[141] D. Ensminger, L.J. Bond. Ultrasonics fundamentals, technologies, and applications (2nd ed.). Taylor & Francis Group, United State of America, 2012 (Chapter 7)

[142] M. Ashokkumar, R. Hall, P. Mulyaney, F. Grieser. Sonoluminescence from aqueous alcohol and surfactant solutions. Journal of physical

chemistry B, 1997, 101, 10845-10850

[143] S. Hatanaka, K. Yasui, T. Tuziut, T. Kozuka, H. Mitome. Quenching mechanism of multibubble sonoluminescence at excessive sound pressure. Japanese journal of Applied Physics part 1-regular papers short notes & review papers, 2001, 40, 3856-3860

[144] P.A. Raghupathi, S.G. Kandlikar. Bubble growth and departure trajectory under asymmetric temperature conditions. International Journal of Heat and Mass Transfer, 2016, 95, 824-832

[145] S.G. Kandlikar. Controlling bubble motion over heated surface through evaporation momentum force to enhance pool boiling heat transfer. Applied Physics Letters, 2013, 102 (5), 051611

[146] S.G. Kandlikar. A theoretical model to predict pool boiling CHF incorporating effects of contact angle and orientation, Journal of Heat Transfer-Transactions of the ASME, 2001, 123 (6), 1071– 1079

[147] B.B. Mikic, W.M. Rohsenow, P. Griffith. On bubble growth rates. International Journal of Heat and Mass Transfer, 1970, 3 (4), 657–666

[148] V.S. Nikolayev, D. Chatain, Y. Garrabos, D. Beysens. Experimental evidence of the vapour recoil mechanism in the boiling crisis. Physics Review Letter, 2006, 97 (18), 184503

[149] I. Tudela, V. Sáez, M.D. Esclapez, M.I. Díez-García, P. Bonete, J. González-García. Simulation of the spatial distribution of the acoustic pressure in sonochemical reactors with numerical methods: a review. Ultrasonics Sonochemistry, 2014, 21, 909–919

[150] W. Zhai, H.M. Liu, Z.Y. Hong, W.J. Xie, B. Wei. A numerical simulation of acoustic field within liquids subject to three orthogonal ultrasounds. Ultrasonics Sonochemistry, 2017, 34, 130-135